

CHARACTERIZATION OF ELECTRICAL DISCHARGE MACHINING PLASMAS

THÈSE N° 3542 (2006)

PRÉSENTÉE LE 9 JUIN 2006

À LA FACULTÉ SCIENCES DE BASE

Centre de Recherche en Physique des Plasmas

SECTION DE PHYSIQUE

ÉCOLE POLYTECHNIQUE FÉDÉRALE DE LAUSANNE

POUR L'OBTENTION DU GRADE DE DOCTEUR ÈS SCIENCES

PAR

Antoine DESCOEUDRES

ingénieur physicien diplômé EPF
de nationalité suisse et originaire de La Sagne (NE)

acceptée sur proposition du jury:

Prof. R. Schaller, président du jury
Dr Ch. Hollenstein, directeur de thèse
Prof. M. Rappaz, rapporteur
Dr G. Wälder, rapporteur
Prof. J. Winter, rapporteur



ÉCOLE POLYTECHNIQUE
FÉDÉRALE DE LAUSANNE

Lausanne, EPFL

2006

“La frousse, moi ! ... J’aime autant vous dire, mille tonnerres ! que quand je le rencontrerai, votre yéti, ça va faire des étincelles !”

le capitaine Haddock

Abstract

Electrical Discharge Machining (EDM) is a well-known machining technique since more than fifty years. Its principle is to use the eroding effect on the electrodes of successive electric spark discharges created in a dielectric liquid. EDM is nowadays widely-used in a large number of industrial areas. Nevertheless, few studies have been done on the discharge itself and on the plasma created during this process. Further improvements of EDM, especially for micro-machining, require a better control and understanding of the discharge and of its interaction with the electrodes. In this work, the different phases of the EDM process and the properties of the EDM plasma have been systematically investigated with electrical measurements, with imaging and with time- and spatially-resolved optical emission spectroscopy.

The pre-breakdown phase in water is characterized by the generation of numerous small hydrogen bubbles, created by electrolysis. Since streamers propagate more easily in a gaseous medium, these bubbles can facilitate the breakdown process. In oil, no bubbles are observed. Therefore, the breakdown mechanism in oil could be rather enhanced by particles present in the electrode gap. Fast pulses of current and light are simultaneously measured during the pre-breakdown. These pulses are characteristic of the propagation of streamers in the dielectric liquid. The pre-breakdown duration is not constant for given discharge parameters, but distributed following a Weibull distribution. This shows that the breakdown is of stochastic nature.

After the breakdown, the plasma develops very rapidly (< 50 ns) and then remains stable. The plasma light is particularly intense during the first 500 ns after the breakdown and weaker during the rest of the discharge, depending on the current intensity. While the gap distance is estimated to be around $10\text{--}100\text{ }\mu\text{m}$, the discharge excites a broad volume around the electrode gap, typically $200\text{ }\mu\text{m}$ in diameter. This volume grows slightly during the discharge. Vapor bubbles are generated in water and in oil by the heat released from the plasma. At the end of the discharge, the plasma implodes and disappears quickly. Light is still emitted after the discharge by incandescent metallic particles coming from the erosion of the workpiece. Their temperature is measured around 2'200 K , demonstrating that they are still in a liquid state in the beginning of the post-discharge.

The spectroscopic analysis of the plasma light shows a strong H_α and continuum radiation, with many atomic metallic lines emitted by impurities coming from electrode and workpiece materials. The EDM plasma is thus composed of species coming from the cracking of the dielectric molecules (mainly hydrogen in the case of water and oil), with contamination from the electrodes. The contamination is slightly higher in the vicinity of each electrode, and the contamination from the workpiece increases during the

discharge probably due to vaporization. The electron temperature, measured from copper line intensities with the two-line method, is found to be low. The temperature is around 0.7 eV ($\sim 8'100$ K) in the whole plasma, slightly higher in the beginning of the discharge. The electron density has been measured from Stark broadening and shift measurements of the H_α line. The density is extremely high, especially at the beginning of the discharge ($> 2 \cdot 10^{18} \text{ cm}^{-3}$ during the first microsecond). Then it decreases with time, remaining nevertheless above 10^{16} cm^{-3} after $50 \mu\text{s}$. During the whole discharge, the density is slightly higher in the plasma center. The EDM plasma has such a high density because it is formed from a liquid, and because it is constantly submitted to the pressure imposed by the surrounding liquid. This extreme density produces spectra with strongly-broadened spectral lines, especially the H_α line, and with an important continuum. During the first microsecond when the density is at its maximum, spectral lines are so broadened that they are all merged into a continuum.

The low temperature and the high density of the EDM plasma make it weakly non-ideal. Its typical coupling parameter Γ is indeed around 0.3, reaching 0.45 during the first microsecond. In this plasma, the Coulomb interactions between the charged particles are thus of the same order as the mean thermal energy of the particles, which produces coupling phenomena. Spectroscopic results confirm the non-ideality of the EDM plasma. The strong broadening and shift of the H_α line and its asymmetric shape and complex structure, the absence of the H_β line, and the merging of spectral lines are typical of non-ideal plasmas. The EDM plasma has thus extreme physical properties, and the physics involved is astonishingly complex.

Keywords: electrical discharge machining, EDM, plasma, spark, discharge, non-ideal plasma, optical emission spectroscopy, spectroscopy, imaging, breakdown, dielectric, liquid.

Version abrégée

L'électro-érosion (ou EDM pour *Electrical Discharge Machining*) est une technique d'usinage bien connue depuis plus de cinquante ans. Son principe est d'utiliser l'effet érosif sur les électrodes d'étincelles électriques successives créées dans un liquide diélectrique. L'électro-érosion est aujourd'hui très utilisée dans un grand nombre de secteurs industriels. Néanmoins, peu d'études ont été menées sur la décharge elle-même et sur le plasma créé pendant ce processus. Les améliorations futures de l'électro-érosion, en particulier pour le micro-usinage, passent par un meilleur contrôle et une meilleure compréhension de la décharge et de ses interactions avec les électrodes. Dans ce travail, les différentes phases du processus d'électro-érosion et les propriétés du plasma ont été étudiées de manière systématique, à l'aide de mesures électriques, d'imagerie et de spectroscopie d'émission optique résolue en temps et en espace.

La phase de pré-décharge dans l'eau est caractérisée par la génération de nombreuses petites bulles d'hydrogène, créées par électrolyse. Puisque les *streamers* se propagent plus facilement dans un milieu gazeux, ces bulles peuvent faciliter le processus de claquage. Dans l'huile, aucune bulle n'est observée. Ainsi, le mécanisme de claquage dans l'huile pourrait plutôt être facilité par des particules présentes dans l'espace inter-électrodes. Des impulsions rapides de courant et de lumière sont mesurées simultanément durant la pré-décharge. Ces impulsions sont caractéristiques de la propagation de *streamers* dans le liquide diélectrique. La durée de la pré-décharge n'est pas constante pour des paramètres de décharge donnés, mais elle est distribuée selon une distribution de Weibull. Ceci montre que le claquage est de nature stochastique.

Après le claquage, le plasma se développe très rapidement (< 50 ns) et reste ensuite stable. La lumière du plasma est particulièrement intense durant les premières 500 ns suivant le claquage et plus faible pendant le reste de la décharge, et dépend de l'intensité du courant. Alors que l'espace inter-électrodes est estimé à environ $10-100\ \mu\text{m}$, la décharge excite un large volume autour des électrodes, d'un diamètre typique de $200\ \mu\text{m}$. Ce volume croît légèrement pendant la décharge. Des bulles de vapeur sont générées aussi bien dans l'eau que dans l'huile, dû à la chaleur libérée par le plasma. A la fin de la décharge, le plasma implose et disparaît rapidement. De la lumière est encore émise après la décharge par des particules métalliques incandescentes, provenant de l'érosion de la pièce. Leur température a été mesurée à environ $2'200\ \text{K}$, ce qui démontre qu'elles sont toujours à l'état liquide au début de la post-décharge.

L'analyse spectroscopique de la lumière du plasma montre une forte radiation de la ligne H_α et une forte émission continue, avec la présence de nombreuses lignes atomiques métalliques émises par des impuretés provenant des matériaux de l'électrode et de la

pièce. Ainsi, le plasma d'électro-érosion est composé d'espèces provenant de la dissociation des molécules du diélectrique (principalement de l'hydrogène dans le cas de l'eau et de l'huile), avec une contamination des électrodes. La contamination est légèrement plus forte au voisinage de chaque électrode, et la contamination venant de la pièce augmente au cours de la décharge, probablement à cause de son évaporation. La température électronique, mesurée à partir des intensités de lignes de cuivre avec la méthode dite *two-line method*, est basse. La température est autour de 0.7 eV ($\sim 8'100$ K) dans tout le plasma, légèrement plus haute au début de la décharge. La densité électronique a été mesurée à partir de l'élargissement et du déplacement par effet Stark de la ligne H_α . La densité est extrêmement élevée, particulièrement au début de la décharge ($> 2 \cdot 10^{18} \text{ cm}^{-3}$ durant la première microseconde). Elle décroît ensuite avec le temps, restant néanmoins toujours au-dessus de 10^{16} cm^{-3} après 50 μs . Pendant toute la décharge, la densité est légèrement plus élevée au centre du plasma. Le plasma d'électro-érosion a une densité si élevée car il est formé à partir d'un liquide, et parce qu'il est constamment soumis à la pression imposée par le liquide environnant. Cette densité extrême produit des spectres avec des lignes spectrales très élargies, particulièrement la ligne H_α , et avec une importante radiation continue. Pendant la première microseconde où la densité est à son maximum, les lignes spectrales sont tellement élargies qu'elles fusionnent et ne forment qu'un continu.

La basse température et la haute densité du plasma d'électro-érosion le rendent faiblement non-idéal. Son paramètre de couplage Γ typique est en effet autour de 0.3, atteignant 0.45 pendant la première microseconde. Dans ce plasma, les interactions coulombiennes entre les particules chargées sont ainsi du même ordre que l'énergie thermique moyenne des particules, ce qui produit des phénomènes de couplage. Des résultats de spectroscopie confirment la non-idéalité du plasma d'électro-érosion. Le fort élargissement et déplacement de la ligne H_α ainsi que sa forme asymétrique et sa structure complexe, l'absence de la ligne H_β , et la fusion des lignes spectrales sont en effet typiques des plasmas non-idéaux. Le plasma d'électro-érosion possède ainsi des propriétés physiques extrêmes, et la physique y relative est étonnamment complexe.

Mots-clés: électro-érosion, EDM, plasma, étincelle, décharge, plasma non-idéal, spectroscopie d'émission optique, spectroscopie, imagerie, claquage, diélectrique, liquide.

Contents

Abstract	i
Version abrégée	iii
1 Introduction	1
1.1 Electrical Discharge Machining (EDM)	1
1.1.1 Principles	2
1.1.2 History	4
1.1.3 State of the art	8
1.2 Purpose and structure of the work	8
2 EDM plasmas : Background	11
2.1 Discharges in gases	11
2.1.1 Spark, arc, glow & co.	11
2.1.2 Sparks and streamers	12
2.1.3 Electric arcs and cathode spots	14
2.2 Discharges in dielectric liquids	18
2.3 Other similar plasmas	22
3 Experimental setup and diagnostics	25
3.1 Electrical discharge machining device	25
3.2 Electrical measurements	27
3.2.1 Discharge measurements	27
3.2.2 Pre-breakdown measurements	28
3.3 Plasma light intensity measurements	29
3.4 Imaging	30
3.5 Optical emission spectroscopy	32
3.5.1 Principles	32
3.5.2 Electron temperature measurement	33
3.5.3 Electron density measurement	35
3.5.4 General experimental setup	37
3.5.5 Experimental setup for time-resolved spectroscopy	40
3.5.6 Experimental setup for spatially-resolved spectroscopy	40
3.6 Experimental difficulties	41

4	Pre-breakdown of EDM discharges	45
4.1	Bubbles	45
4.2	Pre-breakdown current	46
4.3	Pre-breakdown duration	50
5	Imaging diagnostics of EDM discharges	53
5.1	Imaging of the EDM process	53
5.1.1	Erosion	53
5.1.2	Bubbles	54
5.1.3	Short-circuit	55
5.1.4	Reproducibility	56
5.2	Plasma imaging	56
5.2.1	Evolution of the plasma light intensity	56
5.2.2	Typical plasma image	58
5.2.3	Plasma evolution	59
5.2.4	Effect of the discharge current	59
5.2.5	H $_{\alpha}$ emission	60
5.3	Beginning of the discharge : Fast imaging	61
5.4	End of the discharge and post-discharge	62
6	Optical emission spectroscopy of EDM plasmas	67
6.1	Time-integrated emission spectra	67
6.1.1	Typical spectrum	67
6.1.2	Effect of the dielectric	69
6.1.3	Effect of the electrode material	70
6.1.4	Effect of the electrode polarity	72
6.1.5	Effect of the discharge current	73
6.1.6	Effect of the discharge on-time	74
6.1.7	First estimation of electron density and temperature	75
6.2	Time-resolved emission spectra	76
6.2.1	Merging of atomic lines	76
6.2.2	Evolution of the electron temperature	76
6.2.3	Evolution of the electron density	77
6.3	Spatially-resolved emission spectra	79
6.3.1	Asymmetry of the contamination	79
6.3.2	Electron temperature profile	80
6.3.3	Electron density profile	81
6.4	Time- and spatially-resolved emission spectra	82
6.4.1	Evolution of the contamination	82
6.4.2	Evolution of the electron temperature profiles	83
6.4.3	Evolution of the electron density profiles	84

7	Non-ideality of EDM plasmas	87
7.1	Plasma coupling parameter Γ	87
7.2	Spectroscopic signs of the non-ideality	90
7.2.1	Broadening and shift of H_α	90
7.2.2	Asymmetry and structure of H_α	90
7.2.3	Absence of H_β and line merging	93
7.2.4	Inglis-Teller relation	94
7.3	Summary of the physical properties of EDM plasmas	95
8	Conclusions	101
A	Stark broadening and shift of hydrogen spectral lines	105
A.1	The Stark effect on hydrogen levels	105
A.2	Consequences of the Stark effect on H_α emission	107
	References	111
	Acknowledgments	123
	Curriculum Vitae	125

Chapter 1

Introduction

1.1 Electrical Discharge Machining (EDM)

Electrical Discharge Machining (EDM) is a well-known machining technique since more than fifty years. Nowadays it is the most widely-used non-traditional machining process, mainly to produce injection molds and dies, for mass production of very common objects. It can also produce finished parts, such as cutting tools and items with complex shapes. EDM is used in a large number of industrial areas: automotive industry, electronics, domestic appliances, machines, packaging, telecommunications, watches, aeronautic, toys, surgical instruments...

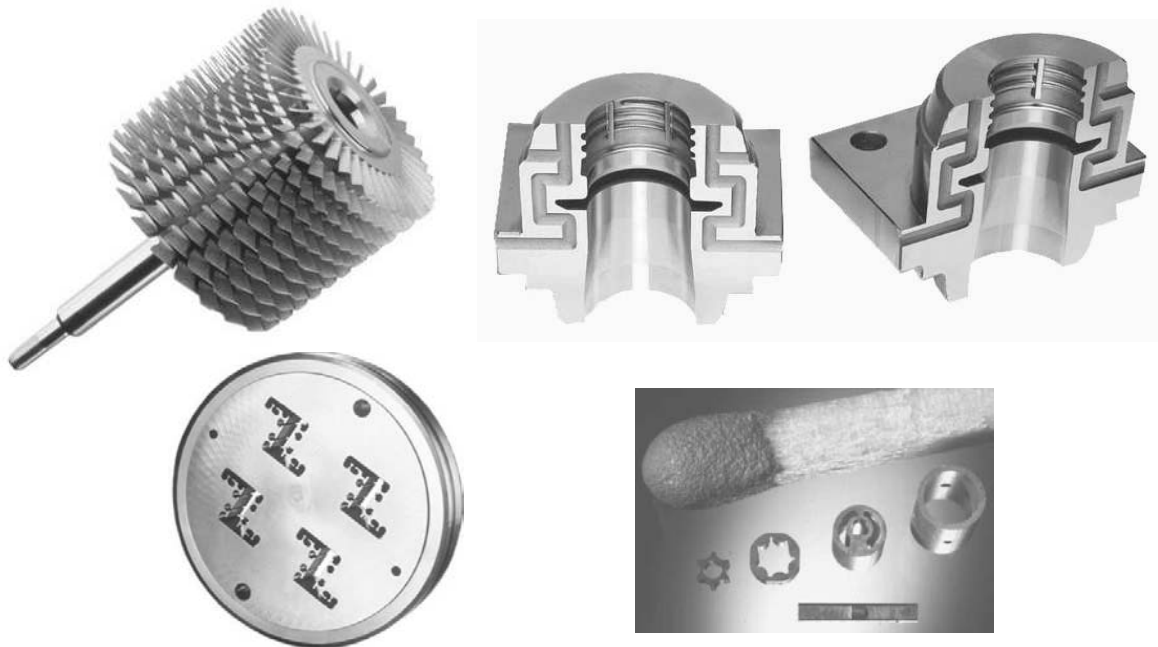


Figure 1.1: Examples of parts machined with EDM: high speed turbine and mold for the screw thread of PET bottles, produced by die-sinking; die for manufacturing plastic cladding and micro-parts, produced by wire-cutting (images © Agie-Charmilles [1,2]).

The advantages of EDM over traditional methods such as milling or grinding are multiple. Any material that conducts electricity can be machined, whatever its hardness (hardened steel, tungsten carbide, special alloys for aerospace applications, for example). Furthermore, complex cutting geometry, sharp angles and internal corners can be produced. Final surface state with low rugosity (< 100 nm) and precise machining (~ 1 μm) are other important advantages. Moreover, there is no mechanical stress on the machined piece, no rotation of workpiece or tool is necessary, and the machines have a high autonomy. On the other hand, the disadvantages are the relatively low material removal rate (order of 100 $\text{mm}^3/\text{minute}$), surface modification of the machined workpiece (“white layer” and heat affected zone, typical depth ~ 50 μm), and limited size of workpiece and tool, for example.

1.1.1 Principles

The principle of EDM is to use the eroding effect of controlled electric spark discharges on the electrodes. It is thus a thermal erosion process. The sparks are created in a dielectric liquid, generally water or oil, between the workpiece and an electrode, which can be considered as the cutting tool. There is no mechanical contact between the electrodes during the whole process. Since erosion is produced by electrical discharges, both electrode and workpiece have to be electrically conductive. Thus, the machining process consists in successively removing small volumes of workpiece material, molten or vaporized during a discharge. The volume removed by a single spark is small, in the range of $10^{-6} - 10^{-4}$ mm^3 , but this basic process is repeated typically 10'000 times per second.

Figure 1.2 gives a simple explanation of the erosion process due to a single EDM discharge. First, voltage is applied between the electrodes. This ignition voltage is typically 200 V. The breakdown of the dielectric is initiated by moving the electrode towards the workpiece. This will increase the electric field in the gap, until it reaches the necessary value for breakdown. The location of breakdown is generally between the closest points of the electrode and of the workpiece, but it will also depend on particles present in the gap [3]. When the breakdown occurs, the voltage falls and a current rises abruptly. The presence of a current is possible at this stage, because the dielectric has been ionized and a plasma channel has been created between the electrodes.

The discharge current is then maintained, assuring a continuous bombardment of ions and electrons on the electrodes. This will cause strong heating of the workpiece material (but also of the electrode material), rapidly creating a small molten metal pool at the surface. A small quantity of metal can even be directly vaporized due to the heating. During the discharge, the plasma channel expands. Therefore, the radius of the molten metal pool increases with time. The distance between the electrode and the workpiece during a discharge is an important parameter. It is estimated to be around 10 to 100 μm (increasing gap with increasing discharge current).

At the end of the discharge, current and voltage are shut down. The plasma implodes under the pressure imposed by the surrounding dielectric. Consequently, the molten metal pool is strongly sucked up into the dielectric, leaving a small crater at the workpiece surface (typically 1–500 μm in diameter, depending on the current).

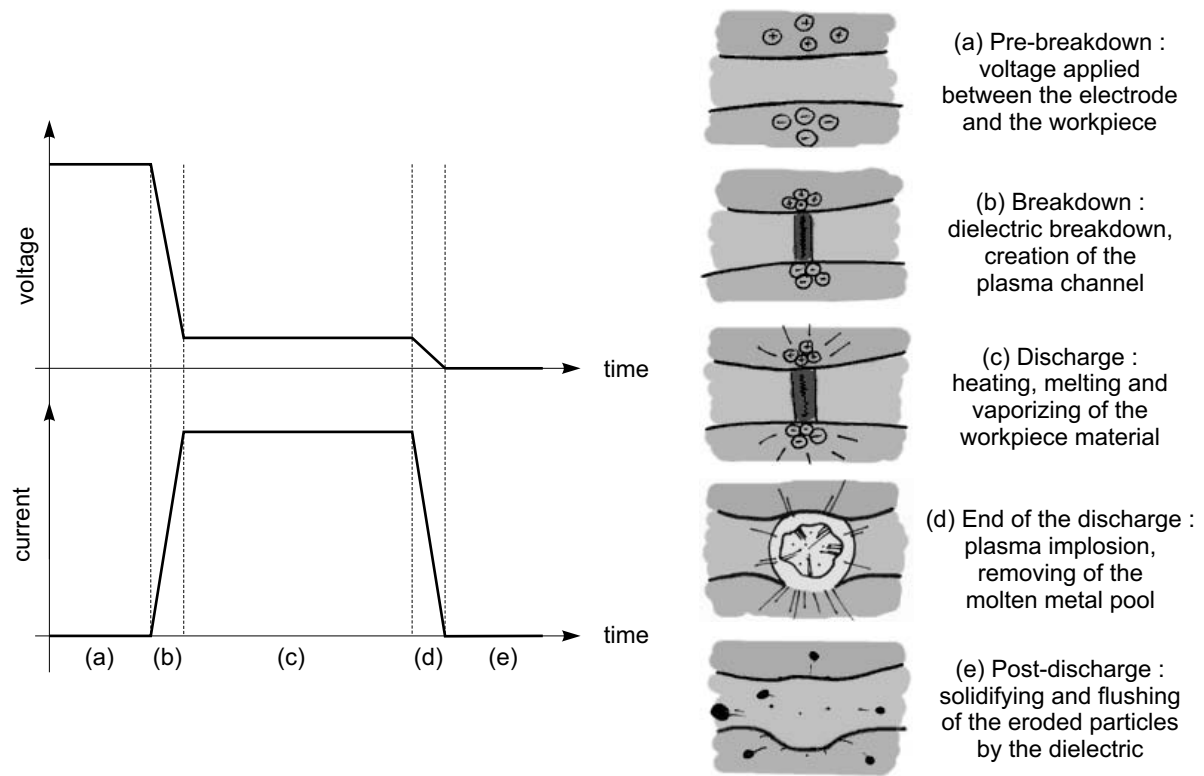


Figure 1.2: Principle of the EDM process.

The liquid dielectric plays a crucial role during the whole process: it cools down the electrodes, it guarantees a high plasma pressure and therefore a high removing force on the molten metal when the plasma collapses, it solidifies the molten metal into small spherical particles, and it also flushes away these particles. The post-discharge is in fact a crucial stage, during which the electrode gap is cleaned of the removed particles for the next discharge. If particles stay in the gap, the electrical conductivity of the dielectric liquid increases, leading to a bad control of the process and poor machining quality. To enhance the flushing of particles, the dielectric is generally flowing through the gap. In addition, the electrode movement can be pulsed, typically every second, performing a large retreat movement. This pulsing movement also enhances the cleaning, on a larger scale, by bringing “fresh” dielectric into the gap.

The material removal rate can be asymmetrically distributed between the electrode (*wear*) and the workpiece (*erosion*). The asymmetry is mostly due to the different materials of the electrodes. But it also depends on the electrode polarity, on the duration of the discharges and on the discharge current. Note that by convention, the polarity is called *positive* when the electrode is polarized positively towards the workpiece, *negative* otherwise. By carefully choosing the discharge parameters, 0.1% wear and 99.9% erosion can be achieved.

Two main types of machining can be distinguished, as shown in figure 1.3. In die-sinking EDM, the electrode is shaped and will produce its negative form into the workpiece. The wear has to be very low, in order to keep the electrode original shape unmodified during the whole machining process. The asymmetry in the material removal rate is thus crucial for die-sinking. The electrode is generally in copper or graphite, and the dielectric is oil. In wire-cutting EDM, the electrode is a continuously circulating metallic wire (typical diameter 0.1 mm, generally in steel, brass or copper), which cuts the workpiece along a programmed path. Deionized water is used as dielectric, directly injected around the wire. The wire is capable of achieving very small cutting angles. The wear is a lesser problem than in die-sinking, because eroded portions of the wire are continuously replaced by new ones due to the wire circulation. Die-sinking EDM is mainly used to produce injection molds, whereas the main applications of wire-cutting EDM are the production of steel cutting dies and extrusion dies.

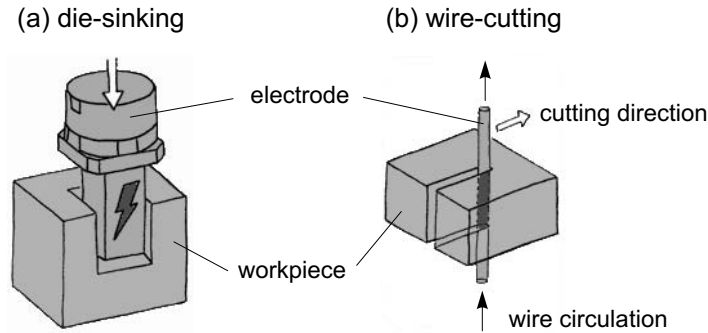


Figure 1.3: Main types of EDM: die-sinking and wire-cutting.

The quality of the machining, i.e. precision and surface rugosity, is directly related to the discharge parameters (current, voltage, discharge duration, polarity...), but also on the dielectric cleanliness. Sparks with strong current produce deep craters: a high removal rate is obtained but with a high surface rugosity. On the other hand, sparks with low current will produce small craters: the surface rugosity is low but the removal rate is also low. For a rough preliminary machining in die-sinking for example, high current, long discharge duration and positive polarity will be chosen, typically 50 A and 1 ms. In wire-cutting, current up to 1000 A can be used, but with shorter duration ($\sim \mu\text{s}$). For surface finishing and polishing, short discharges with low current and negative polarity are used, typically 2 A and 5 μs .

1.1.2 History

The historical roots of EDM date back to the discovery of electric discharges. Besides the discharges produced by natural phenomena, namely lightning, the production of artificial discharges has been closely related to the development of electrical energy sources. First investigations of electrostatic phenomena were performed with frictional machines, during the first half of the 18th century. After that, the first sparks and pulsed arcs were produced with “Leyden jars”, an early form of capacitor invented in Germany and in the Netherlands

around 1745 [4] (see figure 1.4 (a)). More powerful discharges were created by putting several Leyden jars in parallel, creating thus a “battery”. Although scientists of this period sensed that the nature of these artificial discharges was the same as the nature of lightning, the understanding of the observed phenomena was very incomplete.

Joseph Priestley (1733–1804), an English theologian and chemist, was the first to discover in 1766 erosion craters left by electric discharges on the cathode surface:

“June the 13th, 1766. After discharging a battery, of about forty square feet, with a smooth brass knob, I accidentally observed upon it a pretty large circular spot, the center of which seemed to be superficially melted. (...) After an interruption of melted places, there was an intrie and exact circle of shining dots, consisting of places superficially melted, like those at the center.” (see figure 1.4 (b))

“June the 14th, 1766. (...) Examining the spots with a microscope, both the shining dots that formed the central spot, and those which formed the external circle, appeared evidently to consist of cavities, resembling those on the moon, as they appear through a telescope, the edges projecting shadows into them, when they were held in the sun.” [5]

Priestley also investigated the influence of the electrode material and of the discharge current on the craters size.

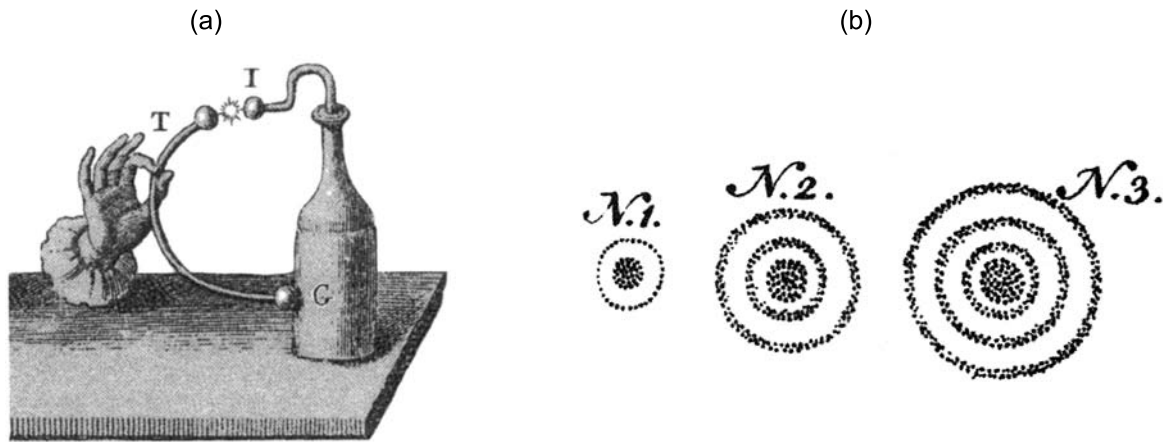


Figure 1.4: (a) Engraved plate sent by Alessandro Volta to Joseph Priestley, showing the spark produced by short-circuit of a Leyden jar (1775) [6]; (b) sketches of erosion craters on cathode surface, observed by Joseph Priestley in 1766 [5].

Whereas the discharges studied by Priestley were pulsed and oscillating (because created by short-circuiting of Leyden jars), continuous discharges could only be produced with battery of electrochemical cells, invented later by Alessandro Volta (1745–1827) in 1799. Developing very large voltaic batteries, the first continuous carbon arc was produced by Vasilii Petrov in St-Petersburg in 1802 [7]. Published in 1803 but only in Russian, his discovery remained ignored and forgotten for over a century. The discovery of electric

arcs is thus often attributed to Humphry Davy (1778–1829). Unaware of Petrov's work, he re-discovered independently carbon arcs around 1808, using the huge voltaic battery of the Royal Institution of London (see figure 1.5 (a)). By separating two horizontal carbon electrodes connected to the battery, Davy created a bright and stable discharge. The shape of this discharge was arched, giving its name to the phenomenon.

Development of devices using electric arcs for lighting purposes followed quickly. Swiss natural philosopher Auguste-Arthur de la Rive (1801–1873) proved in 1820 that arcs can also burn in vacuum, by creating a discharge in an exhausted glass vessel. Figure 1.5 (b) shows examples of these early carbon arc lamps.

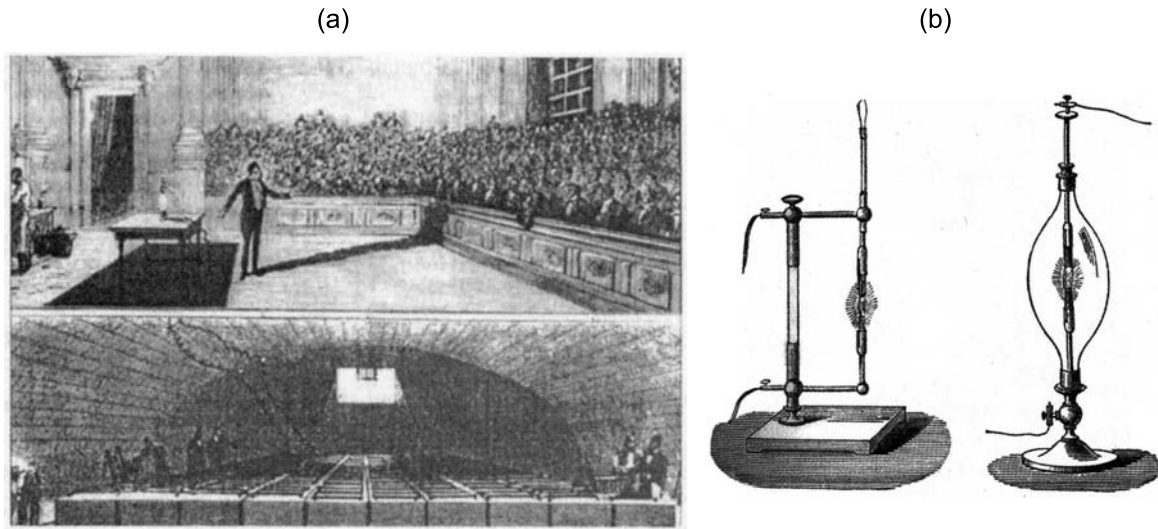


Figure 1.5: (a) Public demonstration of the carbon arc discharge, probably by Humphry Davy in the Royal Institution of London (early 19th century) [7]. The picture below shows the basement filled with a huge battery, used to create the discharge; (b) early carbon arc lamps in air (left) and in exhausted glass vessel (right), also known as “Davy’s electric eggs” or “de la Rive’s electric eggs” [7].

With sophistication of electric sources and industrialization, Auguste de Meritens (1834–1898) developed in 1881 in France a second major application using electric arcs. He used the heat produced by an arc for joining lead plates, inventing the principle of arc welding. Nowadays, electric arcs are also used for coating deposition, metal processing, plasma spraying and as high power switches, for example [8].

The history of EDM itself begins in 1943, with the invention of its principle by Russian scientists Boris and Natalya Lazarenko in Moscow. The Soviet government assigned them to investigate the wear caused by sparking between tungsten electrical contacts, a problem which was particularly critical for maintenance of automotive engines during the second world war. Putting the electrodes in oil, they found that the sparks were more uniform and predictable than in air. They had then the idea to reverse the phenomenon, and to use controlled sparking as an erosion method [9]. Though they could not solve the original wear problem, the Lazarenkos developed during the war the first EDM machines,

which were very useful to erode hard metals such as tungsten or tungsten carbide. The “Lazarenko circuit” remained the standard EDM generator for years.

In the 1950’s, progress was made on understanding the erosion phenomenon [10–12]. It is also during this period that industries produced the first EDM machines. Swiss industries were involved very early in this market, and still remain leaders nowadays. Agie was founded in 1954, and les Ateliers des Charmilles produced their first machine in 1955. Due to the poor quality of electronic components, the performances of the machines were limited at this time.



Figure 1.6: 50 years of evolution in EDM machines: Eleroda D1 (1955) and Robofil 2050 TW (2005) from Charmilles (images © Charmilles Technologies [1]).

In the 1960’s, the development of the semi-conductor industry permitted considerable improvements in EDM machines. Die-sinking machines became reliable and produced surfaces with controlled quality, whereas wire-cutting machines were still at their very beginning.

With the introduction of numerical position control in the late 1960’s and early 1970’s, the movements of electrodes became much more precise. This major improvement pushed forward the performance of wire-cutting machines. Computer numerical controlled systems (CNC) improved further the performance of EDM in the mid 1970’s.

During the following decades, efforts were principally made in generator design, process automatization, servo-control and robotics. Applications in micro-machining became also of interest during the 1980’s [13]. It is also from this period that the world market of EDM began to increase strongly, and that specific applied EDM research took over basic EDM research [14]. Finally, new methods for EDM process control arose in the 1990’s: fuzzy control and neural networks.

1.1.3 State of the art

Fifty years after the first industrial machine, EDM has made considerable progress. Recent improvements in machining speed, accuracy and roughness have been achieved mostly with improvements in robotics, automatization, process control, dielectric, flushing and generator design [15–18]. The other main research domains are the machining of non-conductive materials such as ceramics [19, 20], micro-machining [21–24], characterization and improvement in the machined surface quality [25, 26], and modelling of the EDM process [27–29]. But so far, few studies have been done on the discharge itself, which lies at the heart of the process.

However, in various fields, breakdown in dielectric liquids or solids have already been studied: pre-breakdown and breakdown in different liquids [30, 31] and condensed matter [32], exploding wires in water [33], laser produced plasma in transformer oil [34], and Teflon capillary discharges [35] for example. These plasmas have similar properties to those of the EDM plasma.

Though EDM keeps unmatched abilities such as the machining of hard materials and complex geometries, this technique has to evolve constantly in order to stay competitive and economically interesting in the modern tooling market against other traditional or new machining techniques [17, 18, 36].

1.2 Purpose and structure of the work

Further improvements in EDM performances, especially for micro-machining, require a better control and understanding of the discharge, and of its interaction with the electrodes. A better comprehension of the sparking process will also reduce problems related to its stochastic nature.

Until now, process optimization relied almost only on empirical methods and recipes. It is necessary to go beyond this empirical optimization, and to use reliable numerical models to predict important parameters, such as the material removal rate and wear for example.

Although EDM is quite old, only a few theoretical and numerical studies on the EDM plasma exist [37–40], mainly due to the complex physics involved in this process. The EDM process mixes indeed breakdown of liquids, plasma physics, heat transfer, radiation, hydrodynamics, materials science, electrodynamics... These models still contain several parameters which are empirically determined or artificially introduced. Furthermore, experimental characterization of the EDM plasma is lacking. Some spectroscopic measurements have already been made but remain very incomplete [41, 42]. As we will see later (section 3.6), the EDM plasma is experimentally difficult to investigate. These difficulties are the main cause for the lack of experimental data, which are nevertheless essential as inputs and for the validation of numerical models.

The purpose of this work is thus a systematic experimental investigation of the EDM plasma, in order to measure its physical properties and to improve the understanding of its complex basic physics. Besides the industrial aspect, the study of this plasma is

also of fundamental interest. Other works on similar plasmas, notably measurements of their density and temperature (see sections 2.2 and 2.3), showed that they can be classed among *non-ideal* or *strongly coupled* plasmas. Such plasmas have very interesting physical properties and are still not well known [43–46]. Strongly coupled plasmas produced in the lab are interesting also for astrophysical studies, because deep layers of giant planets and superdense plasmas of the matter of white dwarves are of this kind [43].

This work is one part of a special EDM research project, initiated by the innovation committee of the Technology-Oriented Program NANO 21 (project n° 5768.2). This project was a collaboration involving:

- Charmilles Technologies, as the industrial partner (Dr G. Wälder);
- the Centre de Recherches en Physique des Plasmas (CRPP) of the Ecole Polytechnique Fédérale de Lausanne (EPFL), for the study of the plasma (Dr Ch. Hollenstein);
- the Laboratoire de Simulation des Matériaux (LSMX) of the EPFL, for a numerical model of the temperature evolution in the workpiece surface (Prof. M. Rappaz);
- the Département de Physique de la Matière Condensée (DPMC) of the Université de Genève, for the study of metallurgical processes occurring at the workpiece surface (Prof. R. Flükiger);
- the Electrochemistry group of the Bern Universität, for the study of corrosion aspects of the EDM process (Prof. H. Siegenthaler).

The present manuscript is structured as follows: we will first present in chapter 2 a general background for the understanding of EDM plasmas, i.e. a brief summary of existing knowledge about similar phenomena and plasmas. The different experimental setups and plasma diagnostics used in this work are described in chapter 3, and the experimental results are presented and discussed in chapters 4 (results about pre-breakdown), 5 (imaging results) and 6 (spectroscopy results). Chapter 7 treats the non-ideal character of EDM plasmas, and also gives a summary of their measured physical properties. Finally, general conclusions are given in chapter 8.

Chapter 2

EDM plasmas : Background

Although EDM discharges take place in a dielectric liquid, the first section of this chapter will deal with discharges in gases. They have been extensively studied [47–49], and have common features with discharges in liquids. After that, a brief review about the specific characteristics of discharges in liquids will be given in the second section. Finally, other plasmas similar to the EDM plasmas are presented in the last section.

2.1 Discharges in gases

2.1.1 Spark, arc, glow & co.

Depending on the gas pressure, the electrode gap and the electrode configuration, several discharge regimes can be distinguished. They can be classified according to their current-voltage characteristics, as shown in figure 2.1.

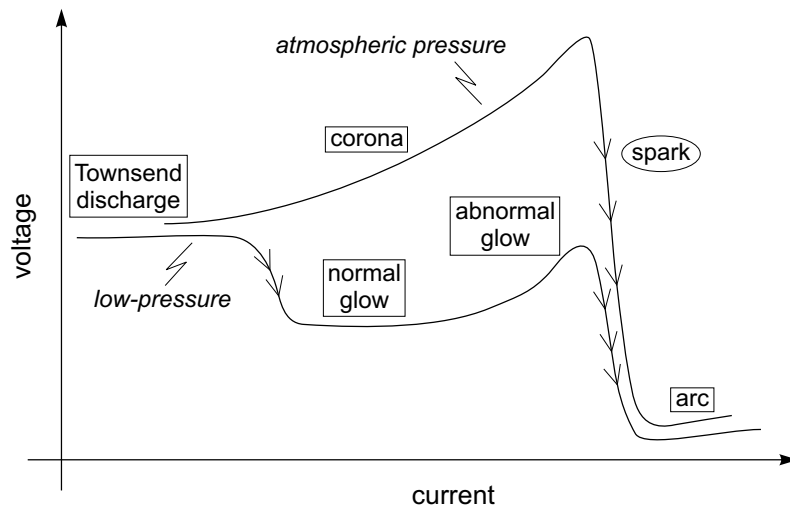


Figure 2.1: Schematic current-voltage characteristics of the different types of discharges in gases [47, 48].

Four main types of *steady* or *quasi-steady* processes exist:

- the **Townsend**'s dark discharge, characterized by a very weak current ($\sim 10^{-8}$ A);
- the **glow** discharge, widely used in many industrial processes, operating at low current ($\sim 10^{-2}$ A), fairly high voltage (~ 1 kV) and low pressure (\sim mbar). The glow plasma is weakly ionized and in a non-equilibrium state, and is visible as a uniform glowing column. As in the Townsend's discharge, electrons are emitted by ion impacts on the cold cathode;
- the **corona** discharge, also at low current ($\sim 10^{-6}$ A) but at atmospheric pressure. Corona discharges develop locally (typically around sharp ends of wires) in strongly non-uniform electric field;
- the **arc** discharge, characterized by high current (~ 100 A), low voltage (~ 10 V) and a bright light emission. The arc discharge differs from the glow discharge in the electron emission mechanism. In arcs, electrons are emitted by thermionic processes, due to the heating of the cathode. The plasma of high pressure arcs can be considered to be in a state of thermodynamic equilibrium.

On the contrary to Townsend, glow, corona and arc discharges, the **spark** discharge is not a *steady* process but a *transient* process, i.e. an unstable transition state of limited lifetime towards a more stable regime (see figure 2.1). To be perfectly rigorous, it would be more proper to say “spark *breakdown*” than “spark *discharge*”, since it is a *transition mechanism* and not a *state resulting from a transition* [48]. However, we will keep (abusively but for clarity) the term *spark discharge* or simply *discharge* when speaking about the period during which the EDM plasma exists (part c in figure 1.2), and the term *breakdown* will refer to the transition from the no-plasma situation to the plasma situation (part b in figure 1.2).

2.1.2 Sparks and streamers

Since the plasma created during the EDM process is precisely a *spark*, it is worthwhile to describe this type of discharge in more detail. Note that lightning shows beautiful examples of giant spark discharges.

The breakdown phenomenon leading to the creation of a spark is complex. The breakdown is too fast to be explained by repetitive electron avalanches through secondary cathode emission, as in low pressure discharges. It consists rather of a very rapid growth of a thin weakly-ionized channel called a *streamer*, from one electrode to the other.

A streamer is formed from an intensive primary electron avalanche, starting from the cathode (see figure 2.2 (a)). A space charge field is associated with this avalanche, due to the polarization of charges inside it. This electric field increases with the avalanche propagation and growth. The avalanche has to reach a certain amplification before it can create a streamer. As soon as the space charge field is comparable or exceeding the applied external field, a weakly ionized region can be created due to this amplification of the electric field: the streamer is thus initiated.

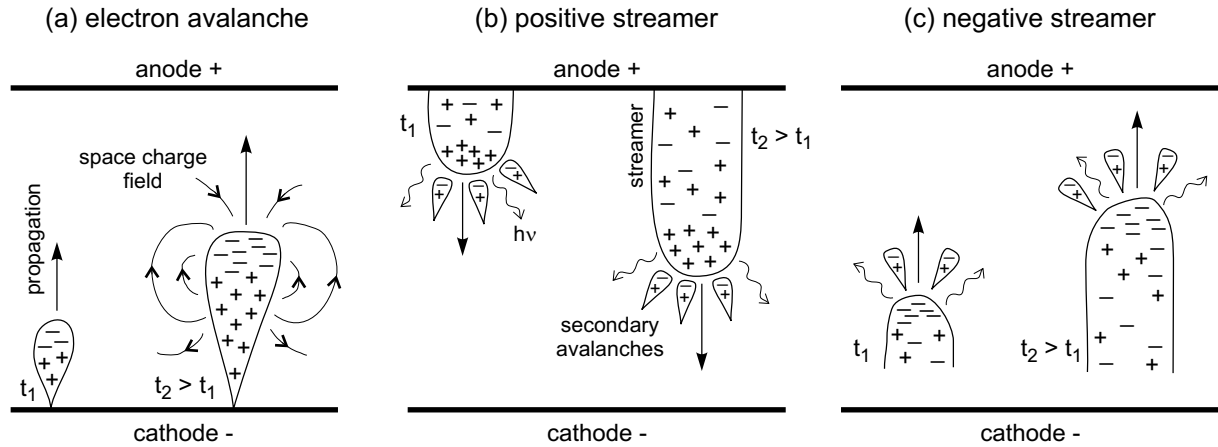


Figure 2.2: Breakdown mechanisms leading to a spark discharge. Propagation of: (a) the primary electron avalanche; (b) a positive streamer; (c) a negative streamer [49].

Once the streamer is initiated, it then grows and propagates, following a zigzagging and branched path due to the random nature of the propagation mechanism. The speed of this propagation is extremely high, reaching 10^6 m/s. The propagation can be directed towards both the anode or the cathode, depending on the gap distance and voltage.

- In **moderate gaps and with moderate voltages**, the avalanche-to-streamer transition occurs only when the primary avalanche has crossed the gap and reached the anode. The avalanche has not grown enough and the space charge field is not high enough to create a ionized region, before the avalanche has reached the anode. Then, the streamer starts from the anode and grows towards the cathode. This kind of streamer is called *cathode-directed* or *positive*. The streamer growth is caused by secondary avalanches, created near the positive head of the streamer (see figure 2.2 (b)). These secondary avalanches are initiated by electrons released by photo-ionization. The electrons of the secondary avalanches are rapidly attracted into the streamer, neutralizing the streamer positive head and leaving behind them the positive ions of the secondary avalanches (ions move much slower than electrons). These positive charges become the new head of the extended streamer. This is how the positive streamer grows.
- In **large gaps and/or with strong gap voltages**, the space charge field of the primary avalanche can be sufficiently high to create the streamer even before reaching the anode. Thus, the avalanche-to-streamer transition occurs *in* the gap. Then, the streamer propagates towards both electrodes at the same time. If the avalanche-to-streamer transition occurs while the avalanche has not yet gone far from the cathode, the streamer grows mostly towards the anode. In this case, the streamer is called *anode-directed* or *negative*. The growth mechanism towards the cathode remains the same as described above, but the growth towards the anode is slightly different. Here, the electrons of the primary avalanche form a negative head for the streamer. These electrons rapidly neutralize the positive ions of secondary avalanches, also

initiated near the streamer head by photo-ionization and by moving electrons (see figure 2.2 (c)). The electrons of the secondary avalanches then form the new head of the extended streamer. Thus, for both positive and negative streamers, the streamer is “feeding” on charges created ahead of its tip by secondary avalanches.

When the electrode gap is closed by a streamer, the breakdown phase is completed and the discharge phase begins. The transition from a weakly-ionized channel (the streamer bridging the gap) to a highly-ionized channel (the spark itself) is poorly understood. It is probably caused by a “back streamer”, similar to the well-known “return stroke” in lightning discharges [49]. If we assume that a streamer is perfectly conducting, the head of a positive streamer, for example, is at the same potential as the anode. When the streamer head is approaching close to the cathode, all the potential fall is located over a very short distance, the distance between the cathode and the streamer head. The electric field is so intense in this region that electrons are emitted in great number from the cathode and from atoms near the cathode. Once the gap is closed by the streamer, these electrons, multiplied at enormous intensity, are accelerated towards the anode in the initial streamer channel, causing strong ionization. This ionization front is propagating “backwards” at $\sim 10^7$ m/s. The formation of the true spark channel is thus probably caused by this back streamer, which strongly increases the degree of ionization in the original streamer channel.

The plasma composing the spark channel is highly ionized and conductive, capable of sustaining a large current ($\sim 10^4$ A). The spark is accompanied by a cracking sound (the thunder in the case of lightning), resulting from the shock wave created by the rapid and localized heating of the gas surrounding the plasma channel. The channel radially expands with time, because the surrounding gas is gradually ionized, by heat conduction and by the shock wave. The temperature of a spark is typically around 1.8 eV (20'000 K), and the electron density around 10^{17} cm $^{-3}$.

If the power source is capable of delivering the discharge current over a certain amount of time, the spark will naturally transform into an arc, since the spark is only a transient process.

2.1.3 Electric arcs and cathode spots

Existing theories, measurements and models about vacuum and atmospheric arcs are abundant [8, 50–56]. It is still a widely studied subject, because cathode phenomena, for example, remain poorly understood due to their extreme complexity. As in the EDM process, it involves solid state, surface and plasma physics, electric and thermal processes. Since arcs erode cathodes by leaving small craters on their surfaces, the knowledge of arc phenomena can be useful to understand the EDM erosion process, although the EDM plasma is not an arc but a spark. Furthermore, the plasma state in a high pressure arc column is found to be relatively similar to that in a spark channel [49].

Cathode region

The cathode is a region of specific interest, because it has to produce the necessary electron current for the arc to survive. A high current density is indeed one of the characteristic feature of electric arcs. While electrons are simply falling from the plasma into the anode because of its higher electrical potential, the cathode has to develop very efficient emission mechanisms to extract electrons from the metal into the plasma. Electrons of the conduction band in the metal need in fact some energy to overcome the energy gap of the metal–plasma interface, also called work function.

The transformation of a spark into an arc is accomplished by the creation of a hot spot on the cathode surface, called *cathode spot*. This small spot ($\sim 10 \mu\text{m}$ in diameter) has astonishing physical properties and is capable of supplying a great electron current. Electrons are emitted from the cathode spot by:

- thermionic emission (emission of the most energetic electrons from a heated metallic surface);
- field electron emission (emission by tunnel effect due to the lowering of the external potential caused by an electric field at the surface);
- thermionic field emission, also called thermo-field emission, which is a combination of the two preceding processes. The electric field enhances the thermionic emission by the Schottky effect. This mechanism dominates by far in electric arc cathodes;
- “thermal runaway”, a non-stationary explosive emission of electrons and explosive evaporation. A significative quantity of cathode material, typically a protrusion at the surface, can be directly evaporated and transformed into a dense plasma. This occurs when there is a sufficiently rapid heating of the cathode, i.e. when the deposited power grows faster than heat conduction in the cathode can remove it [57].

The discharge organizes itself in a such way as to create a strong electron emission from the cathode by the mechanisms cited above, i.e. by raising its temperature and by creating a strong electric field at its surface. The voltage jump is mostly localized near the electrodes, in the so-called anode and cathode layers (see figure 2.3). Consequently,

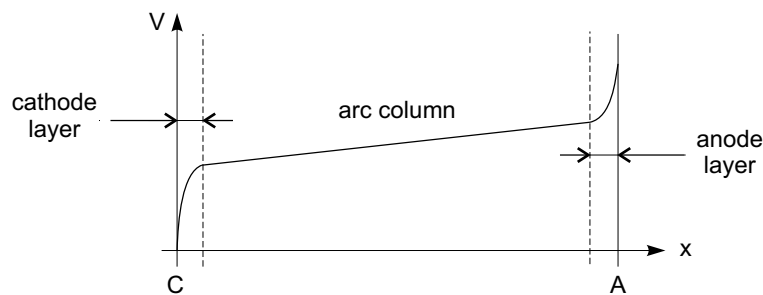


Figure 2.3: Schematic profile of electrical potential in an arc [49].

the electric field is particularly high in these very thin regions. This type of potential profile is due to the presence of space charged regions near the electrodes. The plasma in the cathode layer, usually called cathode spot plasma because it is located in front of the cathode spot, is a small and dense plasma. It remains poorly understood, but its electron temperature is estimated around 5 eV (60'000 K) and its density around 10^{20} cm^{-3} . The cathode spot plasma should thus be dense enough to present non-ideal effects [57].

A detailed structure of the cathode layer is given in figure 2.4. While the plasma of the arc column is assumed to be in thermal equilibrium, the plasma located in the cathode layer is characterized by deviations from equilibrium [53]. First, a deviation of the electron temperature T_e from the heavy particles' temperature T_h is present in a layer of thermal relaxation. Then, we have a violation of the ionization equilibrium. In this ionization layer, the production rate of ions is very high due to collisions with energetic electrons strongly accelerated from the cathode. The ion flux leaving this layer towards the cathode is thus much higher than the flux entering from the layer of thermal relaxation. The dense cathode spot plasma is created in this layer. Finally, the quasineutrality is violated in a very thin sheath near the cathode, where the ion density n_+ is higher than the electron density n_e . This is the space charged region creating the potential profile shown in figure 2.3, and where almost all the voltage drop is located.

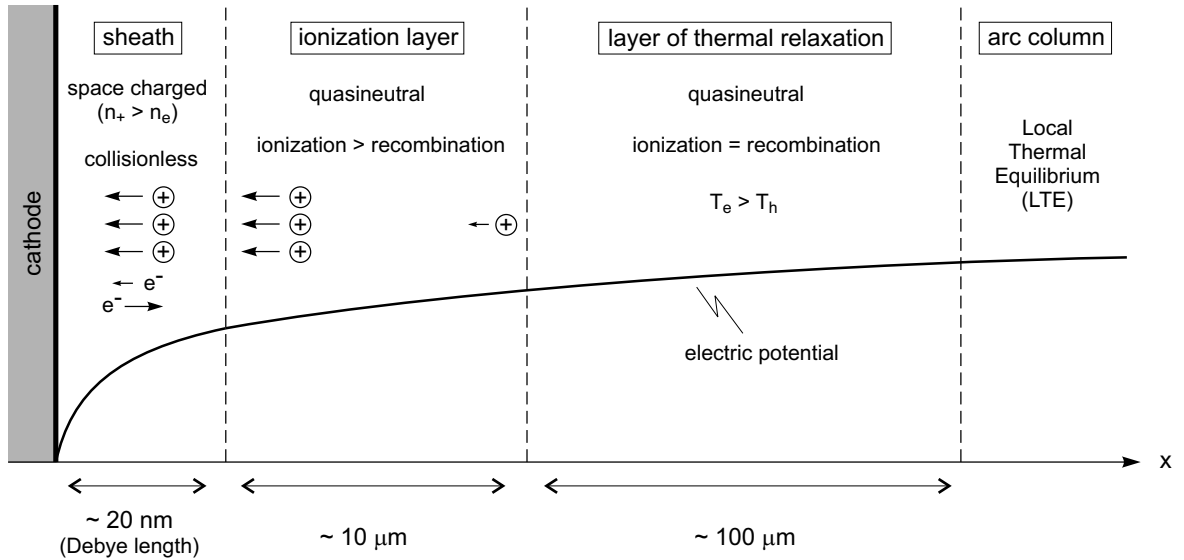


Figure 2.4: Schematic structure of the cathode layer (not to scale). The dimensions of the three layers are evaluated for an argon atmospheric pressure arc plasma at 10'000 K and with a charged particle density of 10^{17} cm^{-3} [53].

By this plasma structure, the cathode spot is strongly heated by the ion bombardment coming from the ionization layer through the collisionless sheath. This heating leads to evaporation and melting, thermionic emission and thermal runaway in some cases. The electron emission is further increased by the electric field produced by the sheath, adding field emission and thermionic field emission. In return, the electrons coming from the cathode are crucial to create a high ionization rate in the ionization layer, producing

the ions that will heat the cathode in a self-consistently balanced regime. This coupled ion/electron production is the sustaining mechanism of the arc discharge.

The terms involved in the energy balance at the cathode spot are multiple. The energy is mainly brought by ion bombardment, but smaller contributions are also given by Joule heating, atom and electron bombardment, recombination in the cathode, plasma radiation (almost negligible [57]) and Thomson effect (also negligible). Energy is mostly dissipated by electron emission and heat conduction in the electrode (slow process), but also by evaporation, surface radiation and droplet emission. The relative importance of all these energy sources and sinks depend strongly on the arc conditions (pressure, materials, current, etc.). Heating mechanisms of electrodes in EDM sparks should be very similar to those occurring in arcs as described here.

The temperature of a cathode spot is typically around 4'000–5'000 K [57], high above the fusion temperatures of metals, which explains the erosive effect of arcs on cathodes. Besides direct evaporation, ejection of cathode melted matter due to the plasma pressure and explosive erosion by thermal runaway, another erosive mechanism can occur also *during* the discharge. If energy dissipation dominates at the surface due to a high radiation and electron emission (this is the case if the surface temperature is very high), the maximum temperature is located below the surface, *in* the cathode spot. This will lead to an internal explosion, and consequently to ejection of solid or liquid matter into the plasma, in the form of μm droplets [57].

Anode region

At the anode, the situation is also complex, depending strongly on experimental conditions with several different modes, and not completely understood. Generally, the current is distributed over a larger surface than at the cathode. The current density is thus lower, and no significative erosion is visible. However, anode spots can develop under certain conditions of current, pressure and anode geometry. In this case, matter can also be evaporated and significant erosion is observed. The plasma structure near the anode has similarities with that near the cathode. A negative space charged region is located directly near the anode surface ($n_e > n_+$), because ions are unable to cross the anode potential barrier. The metal vapor coming from the anode can thus be ionized in the anode layer, due to this space charged region. Energy is brought to the anode by the electron flux and by recombination with ions in the anode; energy is dissipated through evaporation and heat conduction. The temperature of the anode spot is slightly lower than that of the cathode spot, still being around 3'000 K [49].

Inter-electrode plasma

A large quantity of power is dissipated in the arc column by the Joule effect, heat conduction and radiation. On the axis of the column, the plasma temperature is typically around 5 eV (60'000 K) and the electron density around 10^{16} cm^{-3} , but they depend on the gas, the pressure and the current. These values decrease radially, i.e. towards the edges of the column. The plasma of the arc column is thus much less dense than the cathode spot plasma. Due to frequent collisions and thus intensive energy exchange between particles,

the plasma of high-pressure arcs is in local thermal equilibrium. The degree of ionization is also very high, close to 100%.

Arcs in EDM

EDM sparks can sometimes transform into arcs, especially if long discharge durations and graphite electrodes are used. One hot spot is then created on each electrode surface, and the following discharges will systematically take place between these two hot spots and instantly turn into an arc. The result is catastrophic from the erosion point of view, leading to a localized burn of the workpiece surface and to the destruction of the electrode shape. This is particularly problematic when performing smoothing and polishing operations. Hot spots have to be avoided as much as possible during the EDM process, because one of the advantages of this technique is precisely to distribute the erosion spots over the whole workpiece surface. The stochastic change in the localization of the successive spark discharges is thus crucial in EDM.

The arcing phenomenon during EDM is well known, and is generally avoided by stopping the discharge as soon as the voltage reaches a value below a fixed threshold, typically 15–20 V. A decrease in the discharge voltage is the sign of a transition into an arc, because arcs burn with lower voltage than sparks (see figure 2.1). Other arc detection methods exist, based on the measurement of the time lag between the voltage application and the breakdown, on the measurement of the ignition voltage value, or on the measurement of the voltage descending flank at the breakdown [58].

2.2 Discharges in dielectric liquids

The principal difference between discharges in gases and discharges in liquids is the density of the medium in which the breakdown occurs. The higher density of liquids makes them more difficult to break down, i.e. it requires a higher electric field. As described below, the breakdown mechanism is also slightly different, and the plasma properties are strongly influenced by the pressure imposed by the surrounding liquid.

Breakdown in dielectric liquids have been widely studied, especially for insulation problems of electric transformers [32]. Published articles on breakdown phenomena in liquids are very numerous, and the existing knowledge is summarized in a few review articles [32, 59–63]. A wide range of liquids have been investigated: water [64], salted water solutions [65], oils with different aromatic constituents [30, 66, 67], silicon fluids [59], liquid argon and nitrogen [31, 68], benzene, toluene, carbon tetrachloride [69], and other hydrocarbon liquids [70–72] such as propane, pentane, cyclopentene, hexane, cyclohexane, isooctane, decane, etc. The influences of hydrostatic pressure, conductivity [65], viscosity [59], additives [73] and particles [74, 75] on the breakdown mechanism have also been studied.

As in high-pressure gases, streamers are involved in breakdown in liquids. Two types of streamer exist: the *positive* streamer starting from the anode, and the *negative* streamer starting from the cathode. The use of a point-to-plane geometry permits a separate obser-

vation of the two types of streamer, depending on the polarity of the electrodes. Contrary to the situation in gases, the structure and propagation speed of positive and negative streamers are different. As shown in figure 2.5, the positive streamer is “filamentary” and “fast” ($\sim 1\text{--}10\text{ km/s}$), and the negative streamer is “bushy” and “slow” ($\sim 100\text{ m/s}$). In point-to-point geometry, the two types of streamer are emitted from both electrodes.

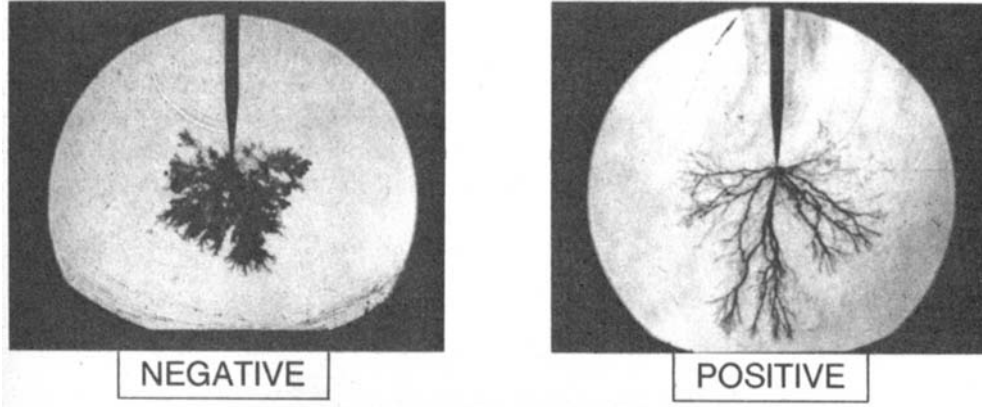


Figure 2.5: Shadowgraphs of negative and positive streamers in oil (taken from [30]).

The sequence of events leading to breakdown can be broken down as follows:

1. Initiation

The initiation of the breakdown mechanism differs from that in gases. Direct propagation of electrons into the liquid and impact ionization are difficult, due to the strong collisions between electrons and molecules occurring in this dense medium. An avalanche of electrons in the liquid phase is thus unlikely, or at least only of short range. It is generally accepted that the development of the primary avalanche, which will create the streamer, takes place in a region of lower density, created beforehand near the electrode. If the liquid pressure is not too high, this low density region is a *vapor bubble* (or a vortex of hot liquid in very viscous liquids [59]).

However, this point is controversial. According to [70, 76], the positive streamer would be a purely electronic process occurring in the bulk liquid, while negative streamer would first involve the formation of a bubble. This should explain the different propagation speed of the two types of streamer. On the other hand, other authors claim that the breakdown process cannot be initiated without the presence of bubbles [77, 78]. The effect of the pressure on streamer initiation, for example, is in good agreement with this second theory. Increasing the pressure inhibits in fact streamer development and increases the breakdown voltage. This shows that the phenomena involved in the breakdown mechanism occur in a gaseous medium. Additional experimental evidence seems to demonstrate that the role of bubbles in the breakdown triggering is indisputable [79].

Micro-bubbles can pre-exist in the liquid [78] or form electrically, i.e. from heat released by small electron avalanches in the liquid or by field emission near electrode

asperities [68, 80]. In salted solutions, ionic currents can also slightly enhance the formation of bubbles [62].

2. Streamer formation

The propagation of the primary electron avalanche is strongly facilitated in the bubble. Since electrons are continuously heating the liquid in the front of the avalanche, and consequently lowering its density, the bubble is growing (time scale ~ 10 ns). New avalanches are formed and thus new bubbles grow ahead of the preceding ones. The ionization of a channel in the liquid, i.e. the formation of the streamer, is caused by this cycle of heating, density lowering and avalanche growth.

3. Streamer propagation

The streamer then grows and propagates according to the mechanism described above, governed by a combination of electrostatic and hydrodynamic forces and even instabilities [32, 59]. This mechanism is quite similar to that in gases, but more complex. The structure of the streamer is systematically branched, more than in gases. This reflects the difficulty for the ionization front to propagate in a dense medium. It could also be due to other inhomogeneously distributed micro-bubbles leading the streamer path, or due to electrostatic repulsion between adjacent streamer branches [78]. Small electric currents (in the form of bursts of fast pulses), localized weak light emission and shock waves are associated with the propagation of streamers.

4. Gap completion and breakdown

When the streamer reaches the other electrode, a reverse ionizing front is observed as in gases, starting from the reached electrode and going back towards the initial electrode. The ionized channel thus thickens, establishing the spark or arc discharge. With negative streamers, the return stroke can even be emitted before the streamer has reached the anode [76]. Intense emission of light is recorded simultaneously with the gap completion, as shown in figure 2.6.

This general description of the breakdown mechanism does not take into account the effects of the numerous experimental parameters. The characteristics of the streamers depend on the gap voltage and distance, on the electrode materials, geometry and surface state, on the liquid pressure, viscosity, density, conductivity, temperature, composition, molecular structure, purity, etc. The presence of particles, for example, strongly facilitates the triggering of a breakdown. The contamination of the dielectric is thus as important as its type for the initiation of a breakdown. The addition of so-called “electron scavengers” can also increase the propagation speed of negative streamers by one order of magnitude. This type of additive (e.g. SF_6 or $\text{C}_2\text{H}_5\text{Cl}$ [30]) increases the electronic affinity of the dielectric molecules. Though streamers are of gaseous nature (cf. influence of pressure, shock waves, role of bubbles), this dependence on electron scavenging additives show that electronic processes are also operating. The emission of light is another evidence of this fact.

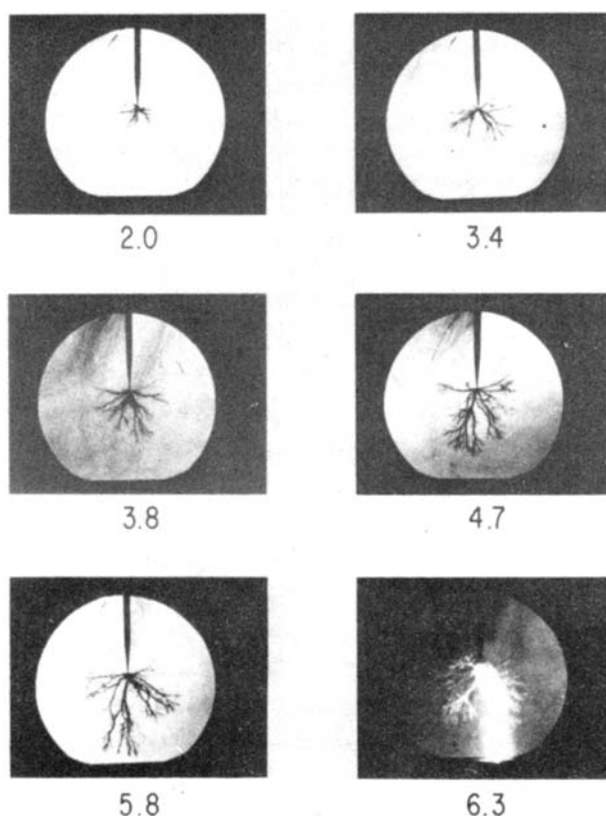


Figure 2.6: Propagation of a positive streamer and breakdown in oil (time in microseconds, gap 1.27 cm, 82 kV, taken from [30]).

Spectroscopic analysis of the light emitted by streamers in hydrocarbon liquids and oil shows the presence of C_2 , C_3 and H_2 molecules, but atomic hydrogen as well [34, 70, 81]. In liquid nitrogen, CN molecules are observed, probably produced by recombination of nitrogen atoms with carbon atoms coming from the electrodes [31]. These results indicate that the fluid molecules are decomposed inside the streamers. Temperatures and densities in streamers have also been measured with spectroscopy. The rotational and vibrational temperatures of N_2 molecules in streamers in liquid nitrogen are 500 and 4000 K respectively [31]; the electron temperature of streamers in oil are about 5'000–10'000 K [34]. The electron density is very high, about $10^{17} - 10^{19} \text{ cm}^{-3}$ for positive streamers, and about $10^{16} - 10^{17} \text{ cm}^{-3}$ for negative streamers [31, 34, 81]. As a general rule, streamers and resulting plasmas in liquids have smaller dimensions and higher densities than those in gases, due to the pressure imposed by the liquid.

To conclude about discharges in liquids, we mention that specific applications have already been developed. Streamer discharges can produce chemical reactants in liquids, which will be used, for example, to degrade organic pollutants by oxidation [82]. Another application is the sterilization of microorganisms present in water, with the aid of chemical species (e.g. H_2O_2) produced by electric discharges [83].

Furthermore, bubbles are of great interest since *single-bubble sonoluminescence* has been discovered. A gas micro-bubble, trapped in a liquid and periodically driven by intense acoustic waves, can emit light when it is violently collapsing. This phenomenon is called sonoluminescence, and still remains puzzling [84]. The emitted light is in the UV range, which implies a high energy density inside the bubble. Recent experiments seem to prove the existence of a plasma inside a sonoluminescing bubble [85]. Its temperature would be above 15'000 K. Thus, these bubbles could possibly be used to produce thermonuclear fusion.

2.3 Other similar plasmas

Besides sparks and high-pressure arcs in gases, other plasmas have similar properties to those created by electric discharges in dielectric liquids and to EDM plasmas.

Exploding wires

Plasmas in liquids can not only be created by applying high voltage between two immersed electrodes. They can also be formed by exploding wires. In such experiments, a thin metal wire placed in water is rapidly vaporized due to the flow of a strong current (~ 100 kA on μ s time scale). The plasmas produced in this way have extremely high electron densities ($10^{21} - 10^{22} \text{ cm}^{-3}$) and pressure (~ 10 kbar), and temperatures of a few eV ($10'000 - 30'000$ K) [33, 86–88]. These high densities are caused by the strong confinement created by the liquid inertia. Such plasmas are so dense that their core is optically highly opaque. Explosives have even been used to further increase the plasma confinement, and consequently increase the plasma pressure and density [89].

Capillary discharges

In this type of discharge, the confining medium is a small capillary made of glass or another dielectric (Teflon, polyethylene, alumina, BeO for example), typically with an inner diameter of 1 mm. This tube is in contact with two electrodes applying a fast current pulse (~ 1 kA over 100 ns). The plasma is formed by ablation of the capillary walls. The electron densities reached are also high ($10^{16} - 10^{19} \text{ cm}^{-3}$), and the temperatures are of a few eV [35, 90–92].

Laser-produced plasmas

Plasmas of metals and alloys can be created by focusing energetic Nd:YAG laser pulses on solid targets, placed in a vacuum chamber. Typical pulses have a power density of 10^{10} W/cm^2 , a duration of 7 ns, a repetition frequency of 30 Hz, and can be focused on a $300 \mu\text{m}$ diameter spot. These plasmas have an electron density of $10^{16} - 10^{18} \text{ cm}^{-3}$, and a temperature of about 1–1.5 eV ($10'000 - 15'000$ K) [93–95].

Shock waves

The compression by shock waves of gases or metal vapor is another way to produce a dense plasma. The gas is generally contained in a tube heated by a resistor furnace. The shock wave is generated with a system of chambers at different pressures, or with condensed explosives for powerful compression [43, 96]. The gas is then irreversibly compressed and heated. This method produces plasmas with spectacular pressure (~ 100 kbar) and densities ($\sim 10^{23}$ cm $^{-3}$), with temperatures around 10 eV (100'000 K). The use of underground explosions and even nuclear (!) explosives permitted Russian scientists to obtain gigantic pressures, up to hundreds of Mbar [43].

Astrophysical plasmas

Electron densities of plasmas present in the universe cover an astonishingly broad range: from 1 cm $^{-3}$ for interstellar matter and solar wind for example, up to 10^{30} cm $^{-3}$ for white dwarfs, which are the late evolution stage of stars having a mass comparable or lower than that of the sun. Among the most dense plasmas, let us cite the plasmas of the deep layers of giant planets (hydrogen plasma, $6 \cdot 10^{24}$ cm $^{-3}$, 1 eV for Jupiter), the interior of the sun (hydrogen plasma, $6 \cdot 10^{25}$ cm $^{-3}$, 1.5 keV), and other exotic objects such as the matter of brown dwarfs (hydrogen plasma, 10^{28} cm $^{-3}$, 1 keV) and the matter of white dwarfs (carbon plasma, $5 \cdot 10^{30}$ cm $^{-3}$, 10 keV) [43, 44]. Dense plasmas can also be produced by spacecraft entering the bottom layers of giant planet atmospheres. The atmospheric pressure on these planets is very high, due to their strong gravitational field. Thus, a dense plasma will be formed ahead of a travelling spacecraft by heating of the atmosphere.

Micro-plasmas

In contrast to the plasmas described above, micro-plasmas do not resemble to EDM plasmas by their densities, but by their typical gap distance. Plasmas with micro- and submicrometric gaps have recently been produced in air and other gases, mainly due to progress in scanning probe microscopy (SPM) piezoelectric gap controllers [97, 98], and progress in fabrication of micro-devices by photolithography [99]. Typical electron density is $10^{12} - 10^{15}$ cm $^{-3}$, and the electron temperature around 5 eV [99, 100]. Chips creating micro-discharges can be used as ionizing sources for micro-sensors, gas analyzers and mass spectrometers [101, 102], or as integrated plasma chemical vapor deposition (PCVD) apparatus, for example [103]. Micro-plasmas are also studied for plasma display panel (PDP) applications [104]. Recent progress and applications of micro-plasmas have been reviewed in [105].

Moreover, micro-gaps are of fundamental interest and new physical questions are arising. Since the gap distance becomes of the same order as the sheath thicknesses and even as the plasma Debye length, the discharge has perhaps to organize itself differently from the traditional macro-gap discharges.

Chapter 3

Experimental setup and diagnostics

The first section of this chapter presents the EDM device used in this work, along with the machining parameters. The various plasma diagnostics are then described in the following sections. Finally, in the last section we address the specific difficulties related to the experimental study of EDM plasmas.

3.1 Electrical discharge machining device

Figure 3.1 presents different views of the machining equipment at the CRPP. We use a small and versatile die-sinking EDM machine, equipped with a generator of the Roboform type from Charmilles Technologies. The electrode is cylindrical, with a diameter of 3 or 5 mm. In order to better control the localization of the sparks, its tip is conical. The servo-controlled movement of the electrode is only vertical. The workpiece used in our experiments is generally a flat cylinder, 5 cm in diameter. In order to flush the particles contaminating the electrode gap during machining, the dielectric can be pumped, and re-injected into the gap with a shower. No dielectric cleaning is performed during this closed circuit circulation.

The dielectric, the electrode and the workpiece can easily be changed. We use:

- deionized water (typical conductivity $1.5 \mu\text{S}/\text{cm}$), mineral oil (FluX Elf 2, oil for EDM, viscosity 6) or liquid nitrogen as dielectric. With liquid nitrogen, the workpiece is placed in a dewar to avoid boiling as much as possible;
- electrodes in copper, tungsten, graphite and zinc;
- workpieces in W300 steel (AISI Type H11).

The machining process is completely controlled by the generator. It supplies the discharge voltage and current, regulates them, and controls the servomotor for the electrode displacement. The generator uses principally the measurement of the gap voltage to regulate and control the process.

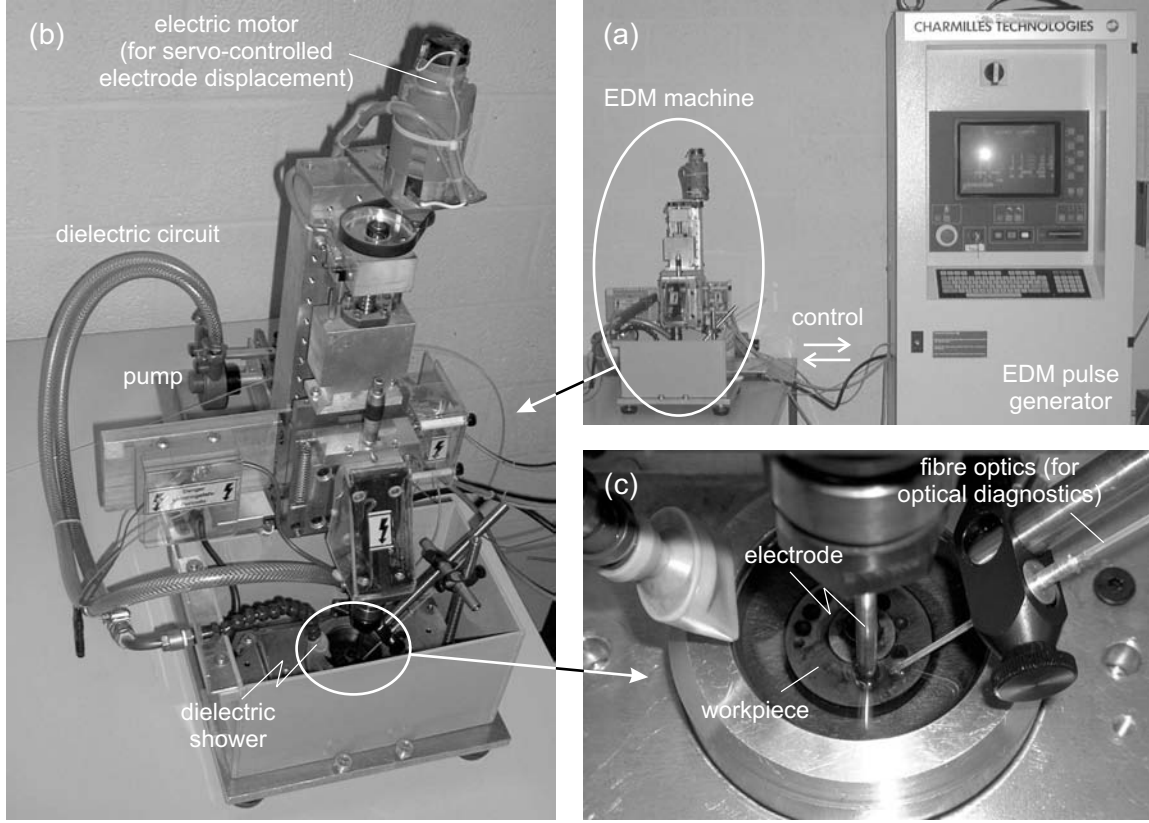


Figure 3.1: EDM device. (a) General view; (b) EDM machine; (c) electrodes.

Figure 3.2 shows the discharge parameters which can be set with the generator: ignition voltage V , discharge current I , discharge on-time, off-time (pause between the end of a discharge and the voltage rise for the next one), electrode polarity.

It is impossible to control the pre-breakdown duration, i.e. the time lag between the voltage application and the breakdown, because it depends on the electrode gap and on physico-chemical properties of the dielectric. Note that the pre-breakdown duration is also called “ignition delay time” or “breakdown time lag”. The value of the voltage *during* the discharge can not be set by the generator either. Its value depends on electrode materials, but is typically around 20–25 V. The values that we can choose with our generator for V , I , on-time and off-time are given in table 3.1.

The machining mode schematically presented in figure 3.2 is called Isopulse, because every discharge has the same on-time, independently of the pre-breakdown duration. This mode is the standard machining mode used in this work. By adding a capacitor in parallel to the gap, it is possible to use the generator in a *capacitive mode*, generally used for surface finishing [106]. The sparks are produced by successive discharges of the capacitor. In this mode, the polarity is always chosen negative. The discharge on-time and current are not controlled, and thus can slightly vary from a discharge to the other, in contrary to the Isopulse mode. Typically, with a 10 nF capacitor, the discharge duration is around 1.5 μs and the current around 6 A.

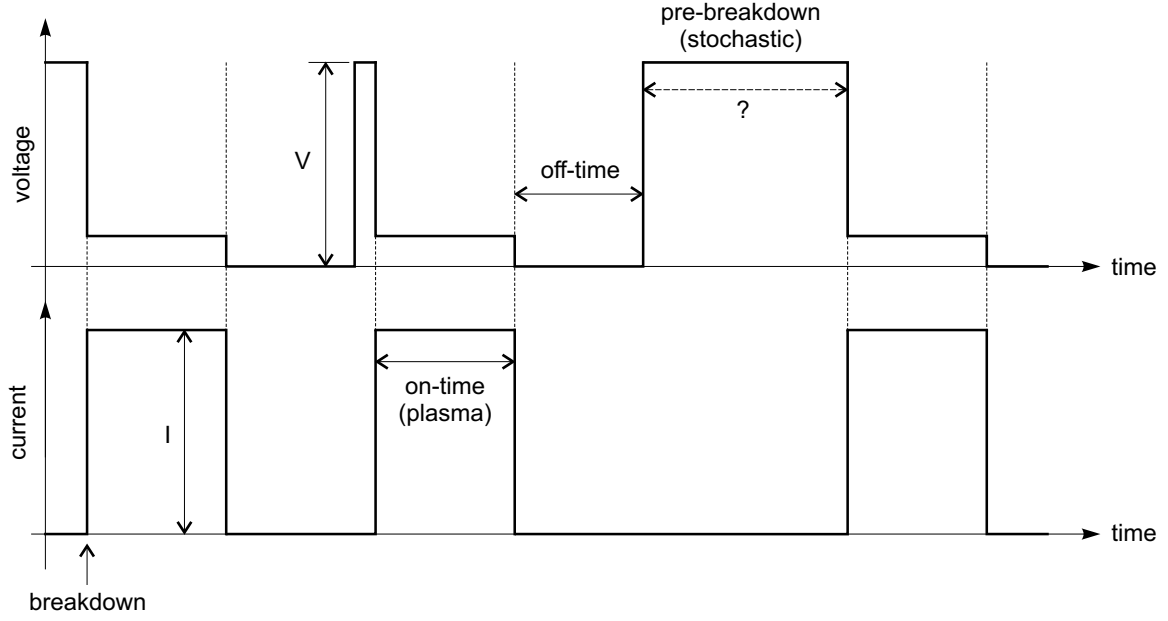


Figure 3.2: Main adjustable discharge parameters in Isopulse mode: V , I , on-time and off-time.

Parameter	possible values
V [V]	$\pm 80, \pm 120, \pm 160, \pm 200$.
I [A]	0.5, 1, 1.5, 2, 3, 4, 6, 8, 12, 16, 24, 32, 48, 64.
on-time [μs]	0.4, 0.8, 1.6, 3.2, 6.4, 12.8, 25, 50, 100, 200, 400, 800, 1600, 3200.
off-time [μs]	0.8, 1.6, 3.2, 6.4, 12.8, 25, 50, 100, 200, 400, 800, 1600, 3200.

Table 3.1: Discharge parameters: possible values.

3.2 Electrical measurements

3.2.1 Discharge measurements

The most basic plasma diagnostics consist in measuring the evolution of voltage and current during a discharge. The voltage is measured with a differential probe (SI-9002 by Sapphire Instruments, 25 MHz), connected in parallel to the electrode gap, as shown in figure 3.3. We use two current probes depending on the application:

- a fast current transformer (FCT from Bergoz Instrumentation, 1.6 GHz) for fast measurements, typically for the breakdown study;
- a DC – 50MHz probe (AP015 from LeCroy), for a general characterization of the discharges.

The probe is placed around the current cable, near to the upper electrode. Both voltage and current probes are connected to a fast oscilloscope (WavePro 950 from LeCroy, 1 GHz).

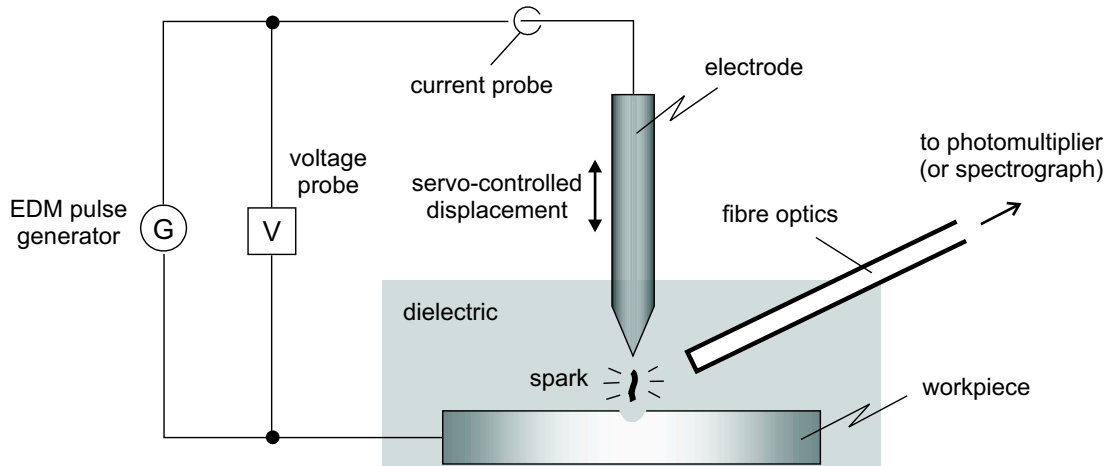


Figure 3.3: Schematic drawing of the diagnostics experimental setup.

Figure 3.4 shows a comparison of measurements with the two current probes. Since the FCT probe acts as a passive transformer, it differentiates DC currents as shown in figure 3.4 (a). On the other hand, this probe is well suited for fast measurements. One can see in figure 3.4 (b) that the response of the DC probe is slower than that of the FCT probe.

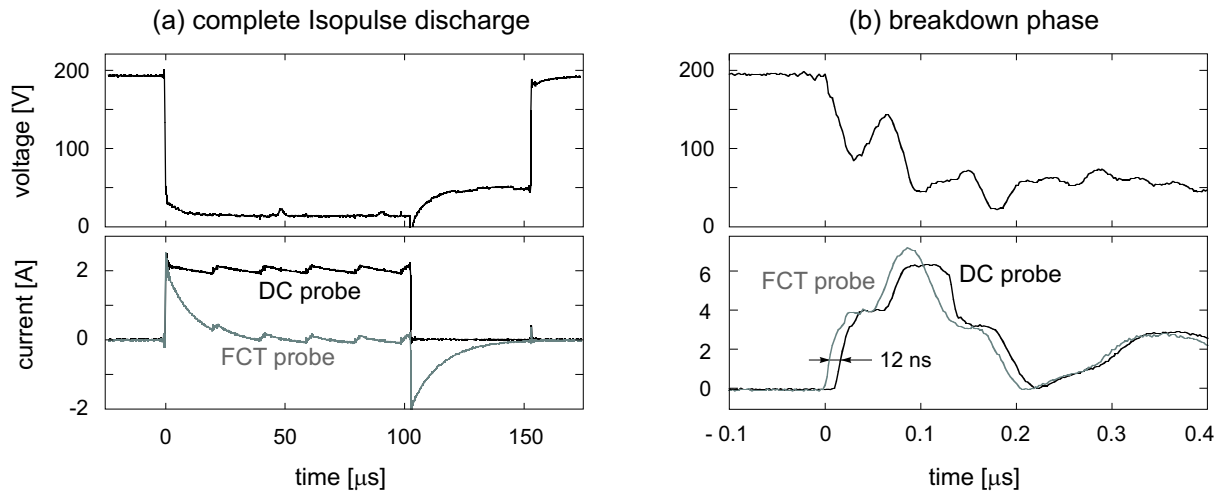


Figure 3.4: Comparison of the two current probes. (a) Measurements during a complete Isopulse discharge; (b) measurements at the breakdown.

3.2.2 Pre-breakdown measurements

For pre-breakdown study, the gap voltage is simply supplied by a standard DC source rather than by the EDM generator, as shown in figure 3.5. Pre-breakdown currents are in

fact weak and fast signals (see section 4.2). The EDM generator produces regular electrical interferences due to its current regulation system, even before a discharge. The intensity of these interferences are of the same order of pre-breakdown current and strongly perturb their measurement. Since the interesting point studied here is pre-breakdown phenomena, a DC source is sufficient to simply maintain a constant electrode gap voltage, without producing any parasitic signal.

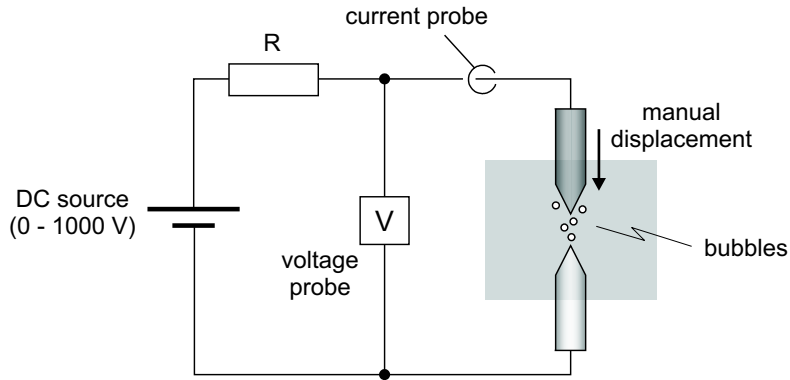


Figure 3.5: Experimental setup for pre-breakdown current measurements.

Without the EDM generator, the upper electrode has to be moved manually, with a micro-screw system. An additional resistance (typically $R = 12 \text{ k}\Omega$) is placed in series, in order to avoid short-circuiting of the DC source when the electrodes come into contact. Both electrodes used are pointed, because this geometry is found to enhance the occurrence of pre-breakdown current and the bubble generation.

3.3 Plasma light intensity measurements

The temporal evolution of the light intensity emitted during a discharge is measured with a fast photomultiplier (H6780 from Hamamatsu, spectral sensitivity 200 – 800 nm, rise time 0.78 ns). The light is transmitted to the photomultiplier by a quartz fibre located near the plasma (see figure 3.3). Inside the photomultiplier, the photons are transformed into electrons by a photocathode, and then multiplied by dynodes. The photomultiplier delivers an output current, which is proportional to the incoming light intensity. To further improve the sensitivity of the measurement, the output current is amplified again (with a C6438 amplifier from Hamamatsu, DC – 50 MHz). Finally, the current is measured with the oscilloscope.

This measurement is not an absolute intensity measurement, which would require a specific calibration. This is not necessary, since the interest of this measurement is simply to determine how the emitted light intensity evolves during the discharge.

3.4 Imaging

Due to the small size of the electrode gap, close images of the electrode region show details which are not visible to the naked eye. It gives useful information about the EDM process, especially for its control: influence of bubbles, short-circuit, localization of the discharges, behavior of eroded particles, etc. Imaging of the plasma itself is also interesting, particularly to see the evolution of the plasma size and shape, from the breakdown to the afterglow. Analysis of the plasma development at the breakdown requires a fast camera, because of the rapidity of the phenomenon (< 100 ns).

The most convenient way to acquire images of EDM plasmas is to use an endoscope. This instrument, well-known for medical applications, is composed of thousands of individual optical fibres, which make the “sampling” of the studied object image. The flexibility of the endoscope makes it very easy to position near the electrode gap.

Here we use an endoscope from Myriad Fiber Imaging, 1.5 mm in diameter, composed of 30'000 quartz fibres. The endoscope is equipped with a small built-in quartz lens at its tip, in order to have a magnification of the plasma region. To obtain a compact geometry, this lens is not a conventional one, but a gradient index lens. The light rays are bent *inside* the lens, because it is made of a material with a gradually varying index of refraction. The minimal working distance of the endoscope is 4 mm, the depth of field 2.5 – 15 mm, the field of view 30° in air and $20 - 25^\circ$ in water. An example of an image obtained with the endoscope is given in figure 3.6. The individual fibres composing the instrument can be seen on the zoomed image.

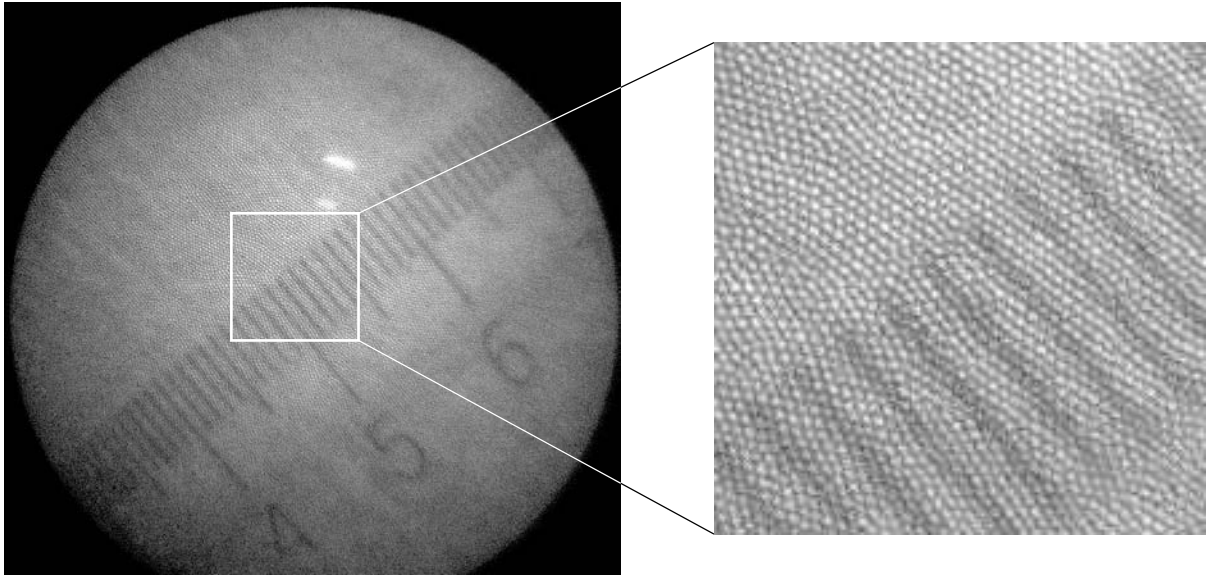


Figure 3.6: Image of a ruler graduated every $100\ \mu\text{m}$, taken in air with the endoscope at a distance of 4 mm.

Figure 3.7 shows the experimental arrangement for imaging. The endoscope is directly immersed in the dielectric. Due to its short working distance, it can be placed a few

millimeters from the spark, assuring therefore a good image magnification and small light absorption by the dielectric. When studying the EDM process in general, the endoscope is placed a few centimeters from the electrode gap and slightly above, in order to have a general view of the electrodes and their surrounding environment. To observe the electrodes, an external lighting is necessary to illuminate them, because our endoscope is not equipped with a source for illumination. We use two halogen lamps for this purpose. For plasma imaging, the endoscope is placed much closer to the plasma (5 mm typically), and the flat workpiece is replaced by a pointed one. With this point-to-point geometry, the plasma is thus localized as much as possible.

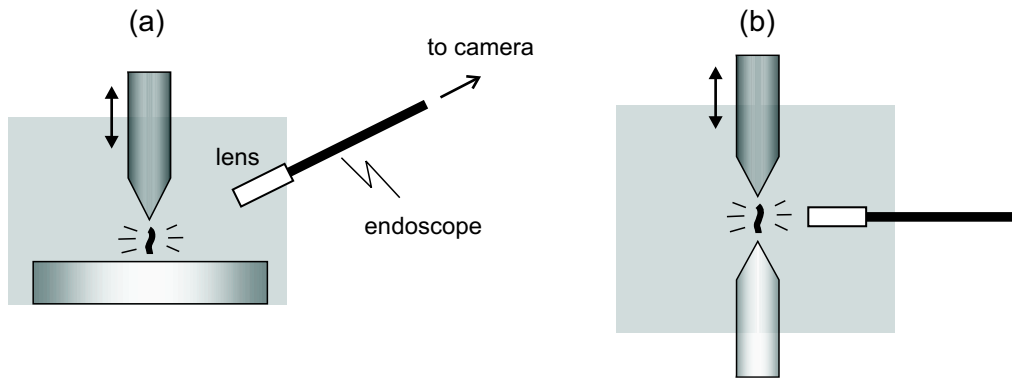


Figure 3.7: Schematic drawing of the experimental setup for imaging. (a) Imaging of the EDM process; (b) plasma imaging.

The endoscope is directly connected to a CCD camera (SensiCam Fast Shutter from PCO Imaging, 12 bit, exposure time 100 ns – 10 ms, 1280×768 pixels). The image focusing is done by a lens with adjustable focal length, placed between the end of the endoscope and the CCD camera.

For time-resolved imaging, i.e. acquisition of successive images of short exposure time taken at different moments of the discharge, the camera can be gated. In this mode, the exposure begins with an external trigger signal, produced by a pulse generator. The delay between the breakdown ($t = 0$) and the beginning of the exposure is set by the pulse generator. The $t = 0$ trigger is obtained by measuring the current rise or the voltage drop which occur at the breakdown.

For fast imaging, we use another camera, an intensified CCD camera (ICCD PI-MAX camera from Princeton Instruments, 16 bit, < 2 ns gating, 1024×1024 pixels). Since short exposure time implies low measured intensities, light intensification is required. This is performed in ICCD cameras by a micro-channel plate (MCP) placed just behind a photocathode. The electrons created in the photocathode are multiplied in the MCP, and then re-transformed into photons by a fluorescent screen. The MCP is also used as a shutter for gated exposure. Since the electrons in the MCP can be abruptly blocked by reversing the electric field, fast gating is achievable with ICCD cameras. For time-resolved imaging with the PI-MAX camera, the delay from the breakdown can be set without a pulse generator. The $t = 0$ trigger is directly sent to the camera controller, and the delay is set by software.

3.5 Optical emission spectroscopy

Optical emission spectroscopy (OES) is a classical plasma diagnostic. Several important plasma measurements can be performed with this non-intrusive method: chemical composition, temperatures, densities, electric and magnetic fields present in the plasma [107–109].

3.5.1 Principles

OES consists in the spectral analysis of the light emitted in the visible region by the plasma. The light is dispersed in a spectrograph, generally by a grating, and detected by photodiodes, a photomultiplier or a CCD camera.

Atoms, ions and molecules emit light with a discrete spectrum when they pass from an excited state to a state of lower energy, i.e. when an electron makes a transition from an upper energy level E_i to a lower energy level E_j inside the atom, ion or molecule. The wavelength λ of the spectral line emitted during this transition will be

$$\lambda = \frac{hc}{E_i - E_j} \quad , \quad (3.1)$$

where h is Planck's constant and c the speed of light. Since the atomic or molecular quantum energy levels are different for every element or molecule, the discrete spectrum emitted by these electronic transitions, called bound-bound transitions, is like a characteristic signature of the emitting species. The plasma composition can thus be determined with OES by identifying the different emitted spectral lines.

While the wavelength of a spectral line is only determined by the type of the emitting species, the intensity of this line depends on the abundance of the emitter, i.e. on its density, and also on the population of the excited state considered. This means that line intensities are dependent on the plasma temperature.

The energy levels of the hydrogen atom can be exactly calculated with quantum mechanics. The main levels are the eigenvalues of the Hamiltonian describing the electron of the hydrogen atom, and are given by

$$E_n = -\frac{13.6 \text{ eV}}{n^2} \quad , \quad n = 1, 2, 3 \dots \quad (3.2)$$

The energy $E = 0$ corresponds to the ionization threshold. A special terminology is used for the lines emitted by atomic hydrogen. They are given in figure 3.8.

A plasma can also emit light with a continuous spectrum. This occurs when free electrons recombine in atoms or molecules: they pass from a state $E > 0$ in the energy continuum (i.e. with no defined energy) to a discrete level inside an atom or a molecule. These transitions are called free-bound transitions. Continuous light is also emitted when free electrons lose energy by passing near an ion or an atom. This is the well-known *Bremsstrahlung*, or free-free radiation.

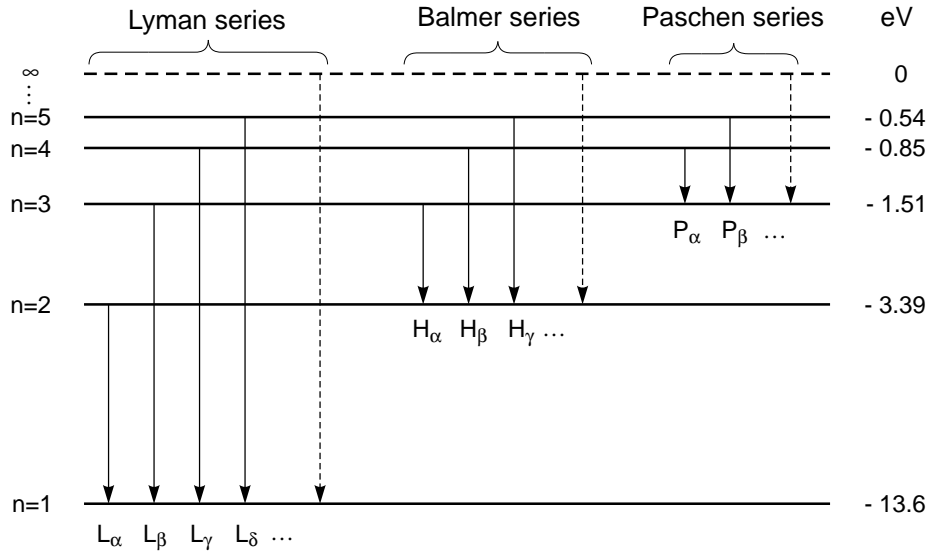


Figure 3.8: Main quantum levels and emission lines of the hydrogen atom.

3.5.2 Electron temperature measurement

To determine the different temperatures of the species present in a plasma, several spectroscopic methods exist [107, 108]. In practice, their respective applicability depends on the type of spectrum emitted by the plasma studied: atomic lines, ionic lines, molecular bands, continuum emission... Most of these methods require the assumption of thermal equilibrium, or at least of local thermal equilibrium (LTE). They need a theoretical relation between the populations of the various excited states and the temperature or the pressure, for example. In case of LTE, this relation is simply given by equilibrium statistical mechanics or thermodynamics. In case of non-equilibrium plasmas, it is much more complicated to develop a theoretical model.

Here, for the electron temperature determination in EDM plasmas, we use the two-line method. This method, which is a particular case of the Boltzmann plot method, is based on measurements of the intensity ratio of two spectral lines, emitted by atoms or ions of the same element [107, 108]. Since it is a relative and not an absolute intensity measurement, the calibration of the absolute spectral sensitivity of the optical arrangement is not necessary.

If we assume that the plasma is in a state of LTE (the validity of this assumption for EDM plasmas will be discussed later, in § 6.1.7), the distribution of atoms and ions in the different excited states is described by the Boltzmann distribution. Thus, the density n_i of a certain type particle, atom or ion, in an excited state i is given by

$$n_i = \frac{n_0 g_i}{Z} \cdot \exp\left(-\frac{E_i}{k_B T_e}\right), \quad (3.3)$$

where n_0 is the total density of the considered particles in the plasma, g_i the statistical

weight of the excited level and E_i its energy, Z the partition function, k_B the Boltzmann constant and T_e the electron temperature. In case of LTE, T_e is also equal to the ion temperature and to the gas temperature; T_e could thus be replaced in (3.3) with a unique plasma temperature T .

The emission coefficient ε of the line emitted by the transition from the upper state i to a lower state j is

$$\varepsilon = \frac{1}{4\pi} \cdot \frac{hc}{\lambda} \cdot A_{ij} n_i, \quad (3.4)$$

where λ is the line wavelength and A_{ij} the probability for the transition from the state i to the state j . Replacing n_i by its expression given in (3.3), we obtain

$$\varepsilon = \frac{hc}{4\pi} \cdot \frac{n_0}{Z} \cdot \frac{g_i A_{ij}}{\lambda} \cdot \exp\left(-\frac{E_i}{k_B T_e}\right).$$

Considering now two lines λ_1 and λ_2 emitted by the same species, i.e. by atoms or even charged ions of the same element, the ratio of their intensities is given by

$$\frac{I_1}{I_2} = \frac{\varepsilon_1}{\varepsilon_2} = \frac{g_1 A_1}{\lambda_1} \cdot \frac{\lambda_2}{g_2 A_2} \cdot \exp\left(\frac{E_2 - E_1}{k_B T_e}\right),$$

where g_i , A_{ij} and E_i for the line k ($k = 1, 2$) are noted g_k , A_k and E_k respectively. Extracting T_e from the preceding equation, we finally obtain

$$T_e = \frac{E_2 - E_1}{k_B} \cdot \left[\ln \left(\frac{I_1 \lambda_1 g_2 A_2}{I_2 \lambda_2 g_1 A_1} \right) \right]^{-1}. \quad (3.5)$$

The ratio I_1/I_2 is experimentally determined from an emission spectrum. The electron temperature can be thus calculated with equation (3.5) if E_k , λ_k , g_k and A_k are known values for the two lines.

Practically, the choice of the two lines is of importance. Since the relative error on the temperature is

$$\frac{\Delta T_e}{T_e} = \frac{k_B T_e}{|E_2 - E_1|} \cdot \frac{\Delta(I_1/I_2)}{I_1/I_2}$$

according to (3.5), it is crucial to choose two lines with a difference $|E_2 - E_1|$ as large as possible. Moreover, the chosen lines have to be intense and isolated from other lines, in order to avoid overlapping and to minimize $\Delta(I_1/I_2)$. It is also desirable that λ_1 and λ_2 are close to each other. In this case, the absorption by the dielectric and the spectral sensitivity of the optical arrangement can be considered equal for the two lines. No spectral correction is then required for the calculation of I_1/I_2 . Finally, the lines have to be non-resonant ones, to avoid self-absorption. It has to be emphasized that with the two-line method, a minimum error of 10% on T_e is expected [107].

As we will see in chapter 6, copper lines are emitted by EDM plasmas when using a copper electrode. Three atomic copper lines fulfil the conditions cited above. Their parameters are given in table 3.2. Since $|E_2 - E_1|$ must be large, we can use the pairs (a)–(b) and (a)–(c) for the determination of T_e with the two-line method.

Line	λ [nm]	upper state (i)	lower state (j)	E_i [eV]	E_j [eV]	g_i	g_j	A_{ij} [10^8s^{-1}]
(a)	510.554	$4p \ ^2P_{3/2}$	$4s^2 \ ^2D_{5/2}$	3.817	1.389	4	6	0.02
(b)	515.324	$4d \ ^2D_{3/2}$	$4p \ ^2P_{1/2}$	6.191	3.786	4	2	0.6
(c)	521.820	$4d \ ^2D_{5/2}$	$4p \ ^2P_{3/2}$	6.192	3.817	6	4	0.75

Table 3.2: Line parameters of the Cu I lines used for electron temperature determination [110].

In practice, to calculate the line intensities from a spectrum, the background has to be subtracted first. Then the line shapes are fitted with Lorentzian functions (see § 3.5.3), and eventually deconvolved if there are adjacent lines. The line intensity I is not simply the maximum value of the peak, but the whole area under the Lorentzian fit.

3.5.3 Electron density measurement

With the electron temperature T_e , the electron density n_e is another important physical parameter characterizing a plasma, which can also be determined with optical emission spectroscopy. Again, there are several methods based on measurements of line and continuum intensities, but also on measurements of line profile [107, 108, 111]. The electron density has in fact a direct influence on line shapes, while they are relatively insensitive to electron and ion temperatures. Spectral lines are broadened and shifted from their theoretical position, increasingly with the electron density. The influence of the density on line broadening can be qualitatively explained as follows: the collision frequency will increase with density, and so the lifetime of atoms in excited states will decrease due to collisions. By the Heisenberg principle, this will increase the uncertainty on the energy levels, i.e. the uncertainty on the emitted wavelength. Spectral lines are thus more broadened in a dense plasma.

There are several broadening mechanisms:

- the natural broadening, due to the finiteness of the lifetime of an atom in an excited state;
- the broadening due to collisions, such as:
 - the pressure broadening, caused by collisions between emitters and neutral atoms or molecules;
 - the Stark broadening, caused by collisions between emitters and charged perturbers. The atomic quantum levels of emitters are modified by the Stark effect, due to the electric field created by the colliding ions or electrons;

- the Doppler broadening, due to the thermal movements of the emitters along the line of sight.

Stark broadened lines are experimentally valuable for the density determination, because the Stark broadening is particularly sensitive to the electron density. In a dense plasma, and this is the case of EDM plasmas as we will see in chapter 6, this broadening mechanism will dominate by far all the others [34, 111]. For more details on the Stark effect and its consequences on line emission, see appendix A.

The Doppler broadening leads to a Gaussian line shape, while processes involving particle impacts, such as the Stark broadening, lead to a line shape close to a Lorentzian. If both effects take place, the line profile will be a Voigt profile, i.e. a combination of the two. Since Stark broadening prevails in EDM plasmas, our lines have a shape close to a Lorentzian.

In our case, we use the H_α line emitted by atomic hydrogen at 656.28 nm to determine the electron density. Along with H_β , this line is a classical candidate for density measurement, because the hydrogen atom is particularly sensitive to the Stark effect. Furthermore, Stark broadening and shift of the hydrogen Balmer lines have been well studied since many years, because this type of diagnostic is particularly important in fusion experiments and astrophysics, for example. Thus, numerous theoretical and experimental works have been published about Stark broadening and shift of the H_α line, especially for electron density calculations from full width at half maximum (FWHM) measurements [112–115] and from shift measurements [113–117].

Computation of spectral lineshapes is quite difficult, because collisions of both electrons and ions with the emitter have to be taken into account as the broadening mechanism. But in recent years progress has been made to include several dynamic effects in calculations, especially ion dynamics. Here we used the theories of Gigos and Cardenoso on broadening [112] and of Oks on shift [115] to calculate the electron density.

Figures 3.9 (a) and (b) show respectively the simulation results for the dependence of the FWHM and of the shift of H_α on the electron density. Though the plasma temperature has a weak influence on the line profile, the simulations of FWHM are calculated for different temperatures and for different reduced mass μ of the emitter–perturbing particle pair. Here, we use the calculation for a plasma of 10'000 K (which is close to the actual EDM plasma temperature, see chapter 6), and with $\mu = 1$ (i.e. hydrogen atoms perturbed by heavy particles). For the shift simulation, we use calculations made for plasmas with temperatures from 13'000 to 20'000 K. EDM plasmas are cooler, but simulation results for lower temperature are not available. The determination of n_e is more precise with the FWHM measurements, because the broadening of H_α is experimentally easily measurable for densities at which the shift is still very low. At $5 \cdot 10^{17} \text{ cm}^{-3}$ for example, the FWHM is 3 nm but the shift is only 1.7 Å.

By fitting the simulation results of the figure 3.9, we obtain two equations giving the electron density as a function of the H_α FWHM and of the H_α shift. Thus, to calculate n_e from our FWHM and shift measurements, we use the following relations:

$$n_e = 8.8308 \cdot 10^{16} \cdot (\Delta\lambda_W)^{1.6005} \quad (3.6)$$

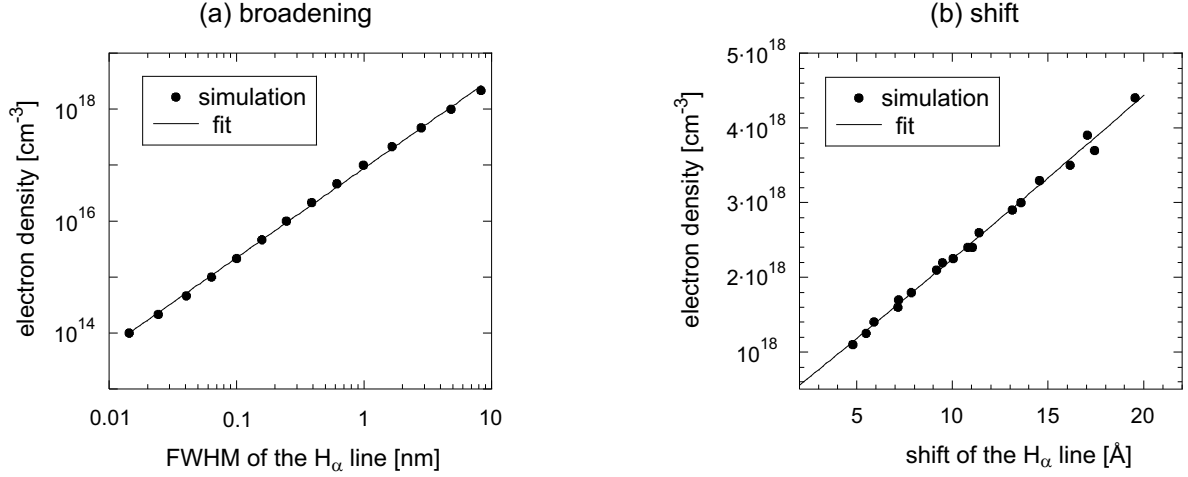


Figure 3.9: Relation between the electron density and: (a) the full width at half maximum (FWHM) of the H α line (simulation results for a 10'000 K plasma with $\mu = 1$, according to [112]); (b) the shift of the H α line (simulation results for plasmas from 13'000 to 20'000 K, according to Oks [115]).

with n_e in cm⁻³ and the FWHM $\Delta\lambda_W$ in nm, and

$$n_e = 10^{17} \cdot (1.3591 + 2.0757 \cdot \Delta\lambda_S + 0.0037 \cdot \Delta\lambda_S^2) \quad (3.7)$$

with n_e in cm⁻³ and the shift $\Delta\lambda_S$ in Å.

In practice, we have to take into account the broadening caused by the spectrograph. This experimental broadening is measured with a laser, which theoretically emits a single wavelength. The H α line is treated as the copper lines for T_e determination: background subtraction and Lorentzian fit. Then, the line FWHM is obtained by subtracting the experimental broadening from the FWHM of the Lorentzian fit.

3.5.4 General experimental setup

The general experimental setup for OES is presented in figure 3.10. The emitted light is collected by a quartz fibre, 1 mm in diameter. The fibre is immersed in the dielectric, located a few millimeters from the spark to optimize the collected light intensity and to reduce absorption from the dielectric. The light is then dispersed by a spectrograph equipped with gratings, and detected by a CCD camera or photodiodes. Finally, the signal is digitalized and treated with a computer.

We use different spectrographs and detectors depending on the application:

- for time-integrated spectroscopy, a 0.275 m spectrograph (SpectraPro 275 from Acton Research Company) with three gratings (150, 600 and 1200 grooves/mm),

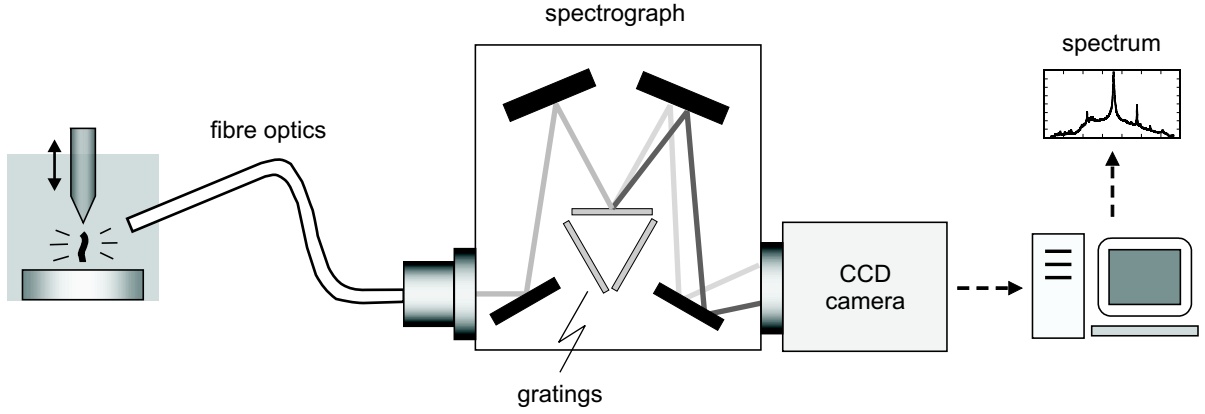


Figure 3.10: Schematic drawing of the experimental setup for optical emission spectroscopy.

equipped with a CCD camera (TE/CCD-1024E from Princeton Instruments, 16 bit, 1024×256 pixels);

- for time-resolved spectroscopy, the same spectrograph SP275 as above, equipped with a detector composed of an array of 700 gated photodiodes (OMA III system from EG&G PARC, 14 bit, 100 ns – 10 ms gating);
- for spatially-resolved spectroscopy, a 0.75 m imaging spectrograph (SpectraPro 750i from Acton Research Company) with three gratings (150, 600 and 1800 grooves/mm), equipped with a CCD camera (Spec-10:400B from Princeton Instruments, liquid N_2 cooled, 16 bit, 1340×400 pixels);
- for time- and spatially-resolved spectroscopy, the same spectrograph SP750i as above, equipped with the ICCD PI-MAX camera used for fast imaging (see section 3.4).

The resolving power and the spectral range for each configuration are given in table 3.3.

	spectrograph SP275						spectrograph SP750i					
	CCD camera			photodiodes			CCD camera			ICCD camera		
	150	600	1200	150	600	1200	150	600	1800	150	600	1800
resolving power [nm]	1.25	0.35	0.17	2.8	0.8	0.25	0.5	0.12	0.03	0.33	0.09	0.02
spectral range [nm]	650	160	70	450	100	45	240	60	15	120	30	10

Table 3.3: Resolving power and spectral range for the different experimental configurations (spectrograph / detector / grating).

The spectral sensitivity of the optical system (fibre + spectrograph + detector) has been measured with a reference light source, whose real emission spectrum is known.

The sensitivity is calculated by dividing the spectrum of the reference source measured through the optical system by the real spectrum. Figure 3.11 shows the results for the spectrograph SP275 with the CCD camera.

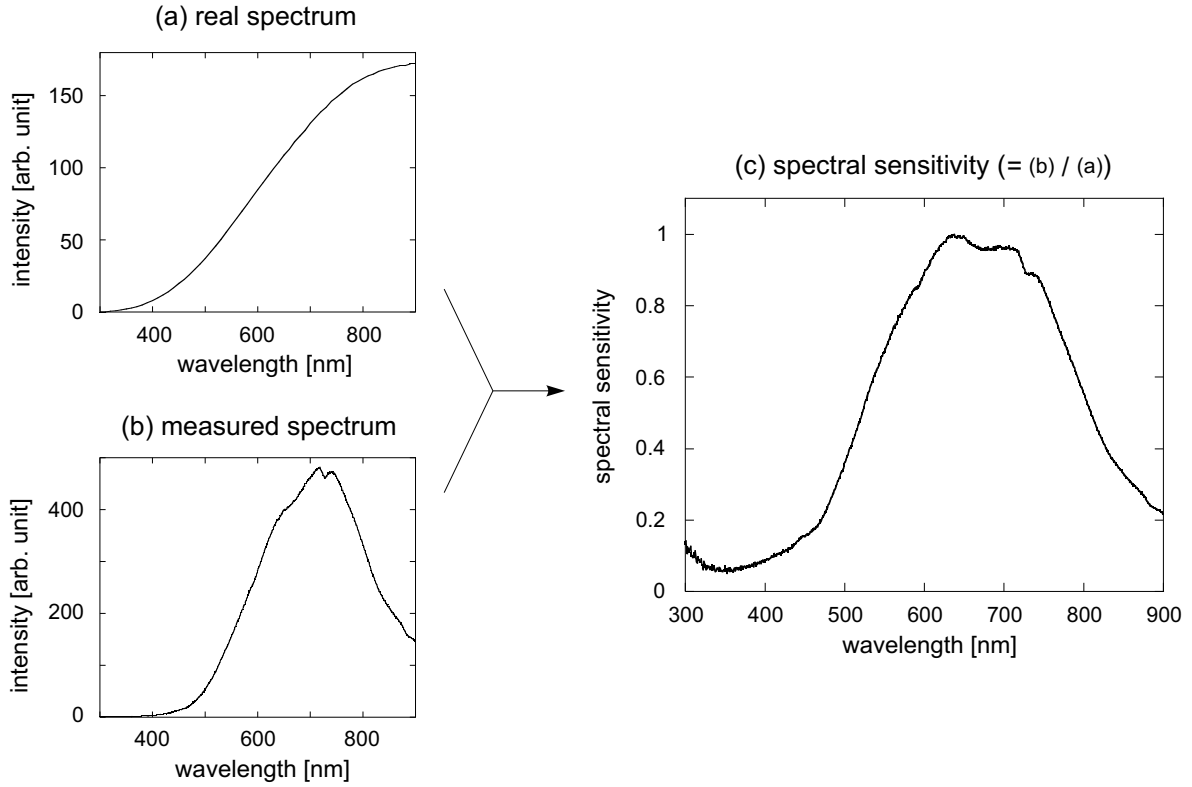


Figure 3.11: Spectral calibration of the optical system composed of the quartz fibre, the spectrograph SP275 and the CCD camera. (a) Real spectrum of the reference light source; (b) spectrum measured through the optical system; (c) spectral sensitivity (normalized).

The spectral sensitivity is maximum between 600 and 750 nm, and falls off below 500 nm and above 900 nm, mainly due to the quantum efficiency of the CCD camera. For all spectrograph-detector configurations, the optical system is sensitive to light emitted roughly between 300 and 1000 nm.

The spectral calibration was made under different conditions: without dielectric, with clean oil and with oil contaminated by eroded particles. Though the light absorption by the dielectric increases drastically in contaminated oil, the relative spectral sensitivity remains approximately the same without oil, in clean or contaminated oil.

Though the plasma light is intense enough for imaging (even with short exposure time $< 1 \mu\text{s}$), it is not possible to perform emission spectroscopy of a single spark. For imaging, the total plasma light is concentrated on a few pixels of the CCD chip. But for spectroscopy, the light is dispersed in the spectrograph and spread over the whole chip. The intensity of a single spark is then far too weak to be measured. The light has to be accumulated over thousands of discharges.

3.5.5 Experimental setup for time-resolved spectroscopy

Time-resolved spectra are obtained with gated photodiodes. As for time-resolved imaging, a pulse generator is used to generate the detector gate. The light is detected only during a short period of the discharge, which is the time resolution of the measurement. Changing the delay between the beginning of the discharge and the beginning of the light acquisition, we obtain a succession of spectra. Each spectrum is obtained by accumulating the light of the same part of thousands sparks, as shown in figure 3.12.

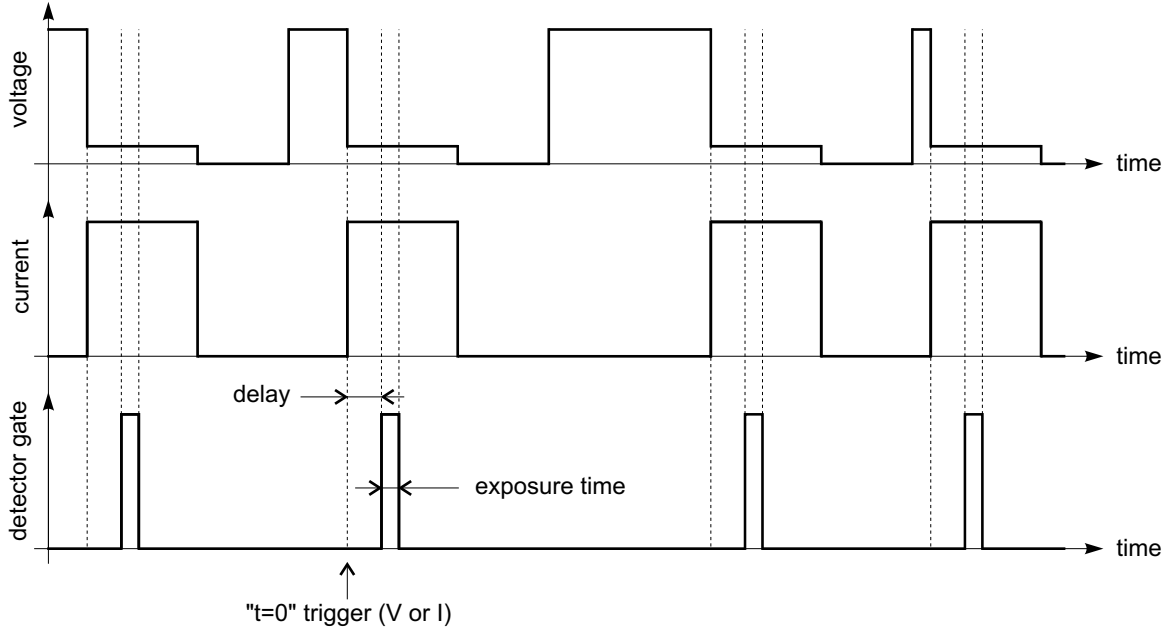


Figure 3.12: Timing diagram for time-resolved spectroscopy.

3.5.6 Experimental setup for spatially-resolved spectroscopy

Figure 3.13 shows the experimental setup for spatially-resolved optical emission spectroscopy.

In order to have a spatial sampling of the emitted light, the magnified plasma image captured with the endoscope is projected onto an in-line array of 16 fibres, arranged over 2 mm. In this way, each fibre collects the light coming from a different zone of the emitting region. With a typical endoscope-plasma distance of 5 mm, the achievable resolution is $\sim 20 \mu\text{m}/\text{fibre}$.

The fibre bundle brings the sampled light into the imaging spectrograph. The 16 different spectra are recorded simultaneously with the CCD camera. Due to the small size of the light emitting region (see section 5.2), this arrangement is the easiest way to perform the spatial sampling. In principle, it could be done directly without the endoscope but with an array of fibres directly located near the plasma, but in this case the miniaturization of the fibres in the bundle is then an issue.

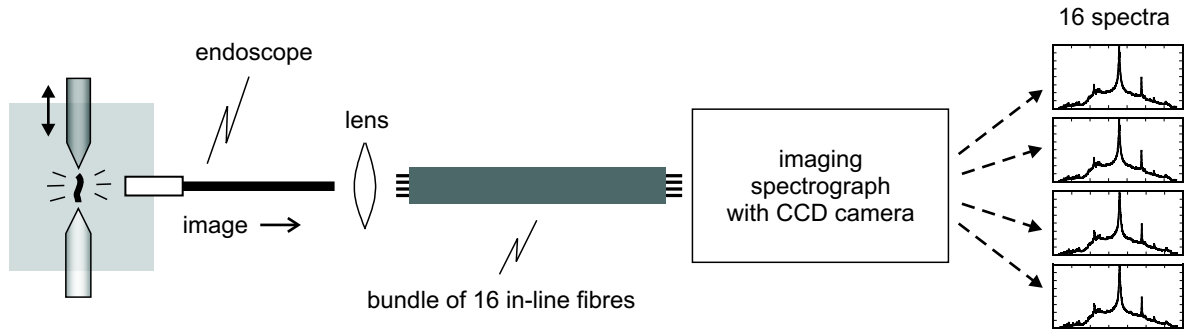


Figure 3.13: Experimental setup for spatially-resolved spectroscopy.

Since the light acquisition is made over thousands of discharges due to the weak emitted intensity, it is necessary that the successive plasmas stay located, as far as possible, in the same position with respect to the endoscope. Otherwise, one fibre of the bundle would sample light coming from different zones of the plasma, and the spatial sampling is no longer valid. As for plasma imaging, we use a point-to-point electrode geometry to localize the sparks as well as possible. Discharges with high current are also avoided, because they produce large craters, and so large variations in the plasma localization already after a few discharges.

For time- and spatially-resolved spectroscopy, the setup is the same as shown in figure 3.13, but the CCD camera is replaced by the ICCD camera, which can be gated.

3.6 Experimental difficulties

The experimental investigation of EDM plasmas is not straightforward. Since this work is precisely an experimental characterization of these plasmas, it is important to emphasize the practical problems encountered.

The main source of difficulties comes from the small size of the plasma. With a typical electrode gap of $10 - 100 \mu\text{m}$, moreover in a liquid environment, it is almost impossible to apply all the classical plasma diagnostics: electrostatic probes, mass spectrometry, microwave diagnostics, actinometry... Intrusive and active methods either are not applicable, or too difficult. Optical methods, such as emission spectroscopy and imaging, are almost the only usable diagnostics.

Furthermore, even the optical diagnostics are difficult to implement in practice. A spatial characterization of such a small plasma is challenging. In addition to the problems related to the miniaturization of light acquisition instruments (optical fibre, endoscope), the weak intensity emitted by the plasma is also an issue. It is necessary to have sensitive detectors and to make the measurements in a dark environment. Even so, measurements of a single discharge remains extremely difficult.

The short duration of the discharges is also problematic. Since the timescale of the discharges is $1 - 100 \mu\text{s}$ and the timescale of breakdown phenomena is $10 - 100 \text{ ns}$ typ-

ically, the measuring devices must have a fast response. Related to the rapidity of the phenomena studied, electrical interference is another problem. In a typical discharge, the current rises at breakdown from 0 to 12 A in ~ 200 ns, for example. The electromagnetic waves associated with this sudden current rise perturb all the electrical measurements, especially weak signals such as photomultiplier signals. Shielding of the measuring instruments becomes of importance.

Another major source of difficulties is the poor reproducibility of the discharges, even with the *same* experimental conditions (see § 5.1.4). The localization of the successive plasmas is constantly changing, due to the evolution during machining of the dielectric cleanliness and of the electrodes surface and geometry. Even the plasma properties can vary, also because of the intrinsic stochastic nature of the breakdown process. In such conditions, one spark can be quite different from another. Since our spectroscopic measurements have been done over thousands of discharges due to the weak intensity of a single spark, this light accumulation can be viewed as a way to overcome the reproducibility problem. In other words, our spectroscopic results are describing an “average plasma”.

Variation in the plasma localization is particularly problematic for time- and spatially-resolved spectroscopy (section 6.4). For such measurements, we need short exposure times in order to have a fine temporal resolution. At the same time, the plasma has to be localized and as stable as possible for the spatial sampling. For a sufficient measured intensity, a short exposure time requires a large number of recorded discharges (typically 100'000 for 2 μ s exposure). But a large number of discharges leads to significative erosion, and thus to movements of the plasma. After a certain time of machining, the workpiece surface is in fact no longer flat and presents the beginning of a hole. Then the following plasmas begin to “move” around the pointed electrode (they are located where the gap is the smallest, i.e. between the electrode tip and the side of the newly machined hole). Figure 3.14 shows an experimental arrangement which minimizes the plasma movements when performing time- and spatially-resolved spectroscopy.

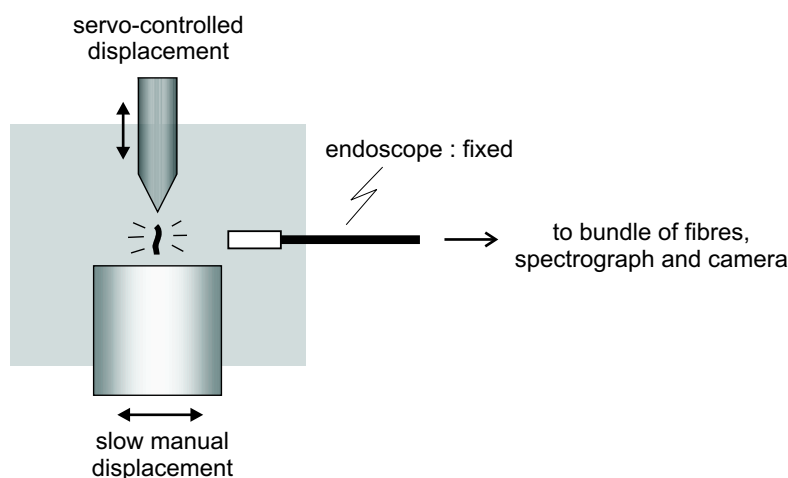


Figure 3.14: Experimental setup for time- and spatially-resolved spectroscopy.

The erosion is considerably reduced by using a workpiece with a large flat surface, which is manually and slowly moved horizontally. Even with a large number of sparks, the erosion is distributed over the whole surface, which remains roughly flat. The plasma movement is thus minimized, permitting a good spatial sampling with a short exposure time.

Chapter 4

Pre-breakdown of EDM discharges

The first of the four chapters presenting experimental results is dedicated to the pre-breakdown phase. The study of the mechanisms leading to breakdown is physically of great interest, but it is also important from the industrial point of view. Since no material removal is performed during this phase, it would be interesting to understand it and to control its duration, in order to reduce this “waste of time” as much as possible.

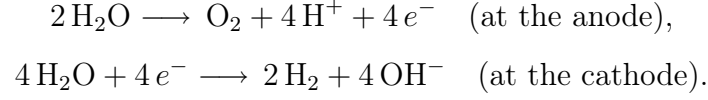
The first section of this chapter summarizes some observations made about the bubbles created during the pre-breakdown. Current measurements are presented in the second section, and finally a short analysis of the pre-breakdown duration is given in the last section. These results are certainly not exhaustive, but they give a first insight into pre-breakdown phenomena.

4.1 Bubbles

Depending on the conditions, small bubbles can be generated at the electrodes as soon as the gap voltage is applied. One can observe that:

- bubbles are created only in water, and not in oil;
- more bubbles are generated when the electric field in the gap is increased. A few bubbles are already visible with a gap of 15 mm and 80 V, and the emission is strongly increased by diminishing the gap distance and/or increasing the gap voltage (see § 5.1.2 for images). Note that no bubbles are generated in oil even with a gap of 100 μm and 1 kV;
- bubbles are created at the cathode;
- the contamination of the water, and consequently its conductivity, has an effect. For example, very few bubbles are generated in clean conditions (water conductivity $< 3 \mu\text{S/cm}$).

These observations suggest that the bubbles are produced by *electrolysis* of the water. The flow of a small electric current in the water releases gaseous hydrogen and oxygen at the electrode surfaces, according to the following reactions:



The observed influences of the electric field and of the water conductivity on bubble generation is a direct sign that bubbles are related to the flow of an electric current. Since we observe only bubbles coming from the cathode, they are bubbles containing hydrogen. The oxygen released at the anode is probably directly consumed for the oxidation of the anode surface. One can in fact observe that the anode, in copper or in steel, is rapidly oxidized after a few minutes.

To confirm that electrolysis is really the source of bubbles, a basic analysis of the bubble gas was performed. Bubbles were collected in a test tube as shown in figure 4.1, and the gas was tested with a detector sensitive to explosive gases (hydrogen, methane or propane for example). The detector was quickly saturated already with a small volume of gas, indicating that the bubbles are certainly made of hydrogen.

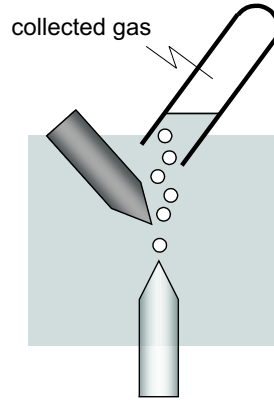


Figure 4.1: Experimental setup for bubbles collection.

Note that the electric field responsible for the electrolysis is much higher than the value simply obtained by dividing the gap voltage by the gap distance. Since we use a point-to-point geometry, the field near the electrode tip is strongly enhanced by the point effect. Figure 4.2 shows a calculation for a gap of 5 mm and 200 V, assuming electrode tips with a curvature radius of 100 μm . The field at the tip can reach 2'300 V/cm, nearly six times higher than the plane electrode, uniform field value of 400 V/cm.

4.2 Pre-breakdown current

Before the breakdown, which is characterized by a large voltage drop and current rise, fast current pulses are sometimes measured. An example of such pre-breakdown current is given in figure 4.3. The measured current pulses reach a few milliamperes and last about 5–20 ns.

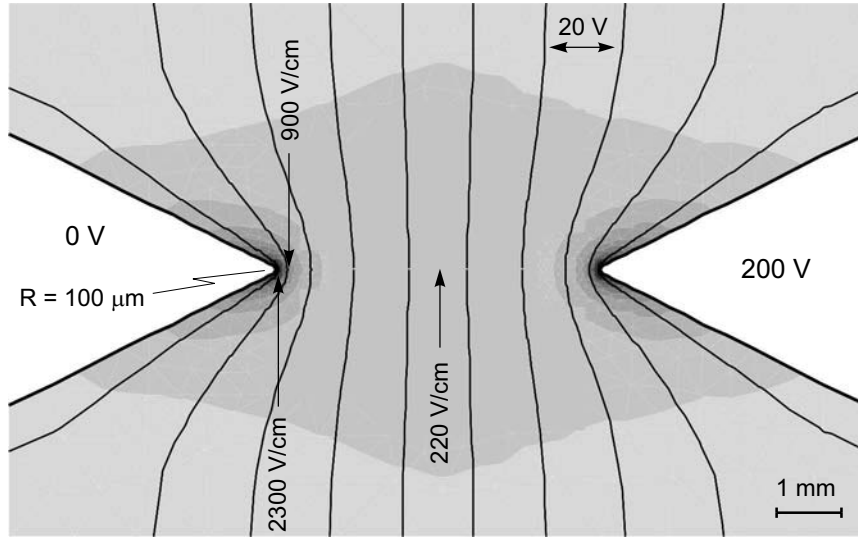


Figure 4.2: Increase in the electric field due to the point effect. Simulation result for a point-to-point geometry, $100\ \mu\text{m}$ curvature radius, 5 mm gap, 200 V, in water: lines of equipotential and electric field strength (in grey scale).

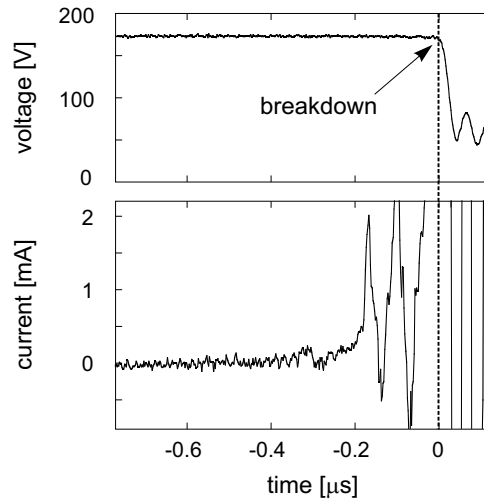


Figure 4.3: Typical pre-breakdown current (AC component) measured in $1.5\ \mu\text{S}/\text{cm}$ water (gap voltage 180 V).

We observe this type of current not necessarily just before a breakdown as in figure 4.3, but randomly as soon as the gap voltage is applied, provided that the electrode spacing is small enough. The occurrence of these irregularly-spaced pulses increases when moving the electrode towards the workpiece. Figure 4.4 shows, on a longer timescale, the multiplication of these current bursts when reducing the gap distance. A DC component is measured (electrolysis current), because the water used is not a perfect dielectric due to its contamination. The water filling the gap acts therefore as a resistance, whose value

is roughly proportional to the gap distance. This explains why we measure a decrease in the gap voltage and an increase in the DC current, when the gap distance is reduced.

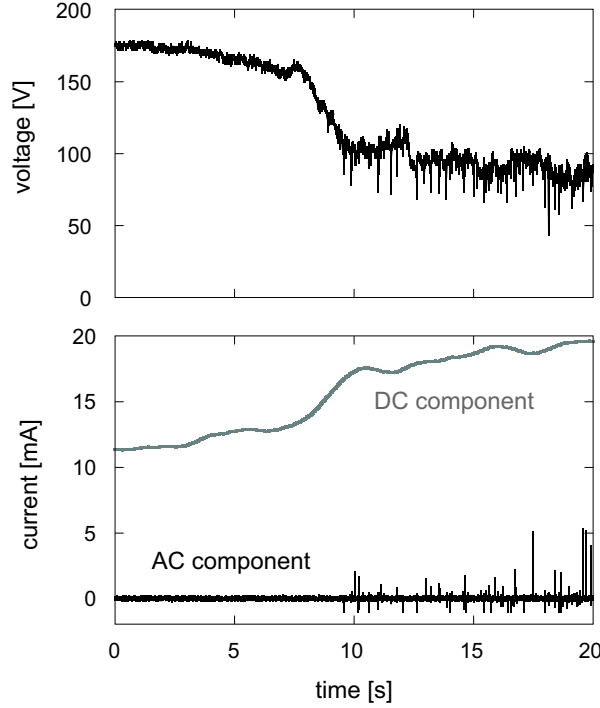


Figure 4.4: Current bursts measured in water when the gap distance is slowly diminished (the electrode is moved manually towards the workpiece).

As mentioned in section 2.2, this type of current signal is typically associated with the propagation of streamers in the gap [31, 34, 63, 66, 72]. Each pulse is due to a sudden growth of the ionized channel. A small current can be measured, because this propagation involves a movement of charged species. The electrode polarity should influence the shape of the pre-breakdown current signal, since positive and negative streamers propagate slightly differently. However, no clear effect can be observed in our measurements, because our electrode geometry is symmetric (point-to-point). To clearly differentiate current signals of the two types of streamer, a strongly asymmetric electrode configuration must be used (point-to-plane, for example [63]).

As for the bubble generation, oil and water behave differently. No AC or DC pre-breakdown current are measured in oil, for any condition. This remarkable point emphasizes the crucial role of gaseous bubbles for the propagation of streamers, as shown also in other studies [77–79]. In water, their initiation and propagation are strongly facilitated by the pre-existing bubbles, created by electrolysis. On the other hand, the creation of a bubble in oil is more difficult, because electrolysis does not occur. The initiation of a streamer in oil requires a higher electric field than that created with our source ($\sim 0.1\text{--}10\text{ MV/cm}$ is necessary, according to [30, 60, 63, 72]). This explains the absence of pre-breakdown current in oil in our measurements.

Although the breakdown mechanisms in water and in oil should not be completely different and should follow the general sequence described in section 2.2, they can nevertheless be influenced by different parameters. In water, the breakdown triggering is certainly enhanced by the presence of bubbles. In oil, there are rather the contaminating particles that could play this role, by forming a “conductive bridge” [3,75]. Although both bubbles and particles certainly influence the breakdown in water as in oil, the dominant contribution is not the same in the two types of dielectric.

As expected, the conductivity of the water has an influence on pre-breakdown current [65]. Figure 4.5 presents measurements in clean water, in water contaminated with eroded particles, and in a slightly salted solution.

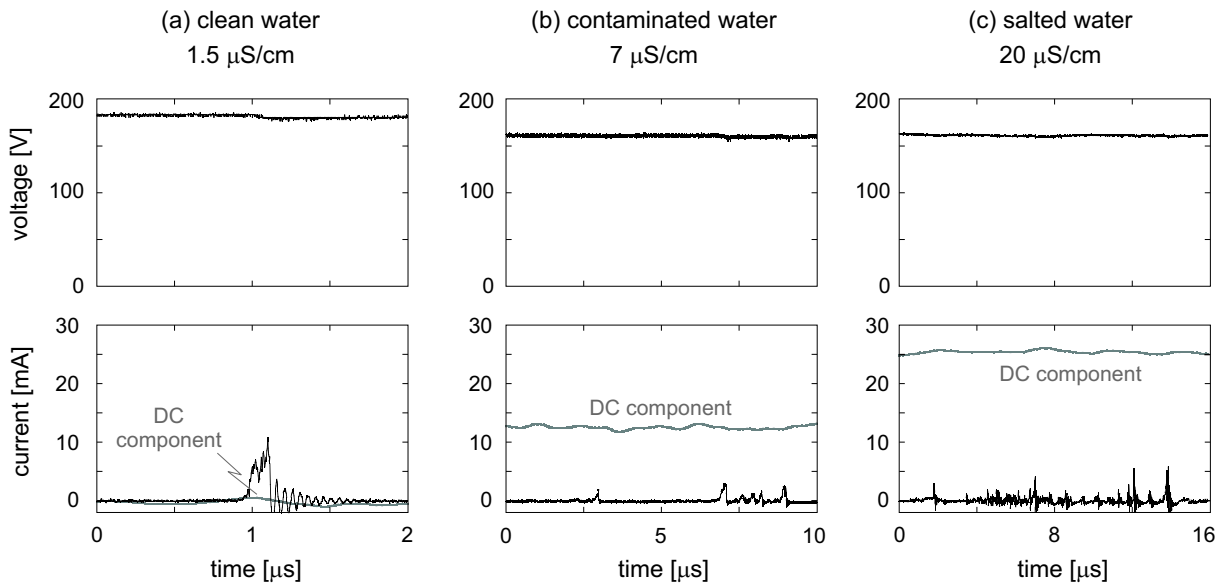


Figure 4.5: Effect of the water conductivity on pre-breakdown current: (a) clean water; (b) water contaminated with eroded particles; (c) salted water.

Increasing the conductivity naturally also increases the DC current. Therefore, the bubble generation by electrolysis will be more efficient and pre-breakdown currents more frequent. This is exactly what we observe in our measurements. In clean water, the DC current is almost zero and current pulses are seldom measured (typically < 1 pulse every $10 \mu\text{s}$). Then, the average number of current pulses per time unit increases with the conductivity.

The addition of external particles or other additives to the dielectric thus certainly influences and facilitates the breakdown mechanism. But for a stable machining process, these additives should not increase the liquid conductivity too much. The liquid has to keep some of its insulating properties. In the salted solution (c), short-circuits become very frequent. A water conductivity higher than $20 \mu\text{S/cm}$ will thus lead to an unstable situation, prejudicial to the quality of the machining process. In real conditions of machining, the dielectric is always contaminated with particles, despite continuous filtering

and cleaning of the liquid. Figure 4.5 (b) thus reflects a more realistic situation than (a) and (c).

Other studies have shown that light is emitted during the propagation of streamers. The light intensity follows the same evolution as the current [31,34,63,66,72]. An example of light emission measured with a photomultiplier during the pre-breakdown is given in figure 4.6.

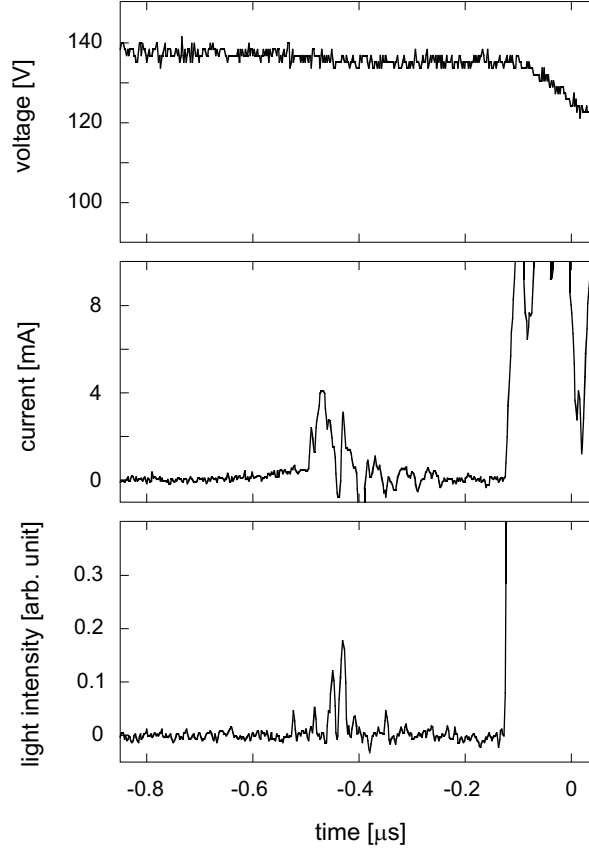


Figure 4.6: Light emission associated with pre-breakdown current in water (gap voltage 140 V).

Whereas the light at the breakdown is intense (saturation of the detector), the emission associated with streamers is very weak. Therefore, the gain of the photomultiplier has to be set high, and this produces considerable electronic noise on the output signal. This kind of measurement is therefore quite difficult. Nevertheless, one can see that the light emission is clearly correlated with the current, as expected.

4.3 Pre-breakdown duration

Once the gap voltage is applied, it takes a certain amount of time until a breakdown occurs. This duration is not constant from a discharge to another, even if they have the

same parameters. Statistics of the pre-breakdown duration have been done for different types of discharges. The mean duration differs according to the discharge parameters, but the duration distribution is always of the same kind. Figure 4.7 shows histograms of the pre-breakdown duration measured on two types of discharges.

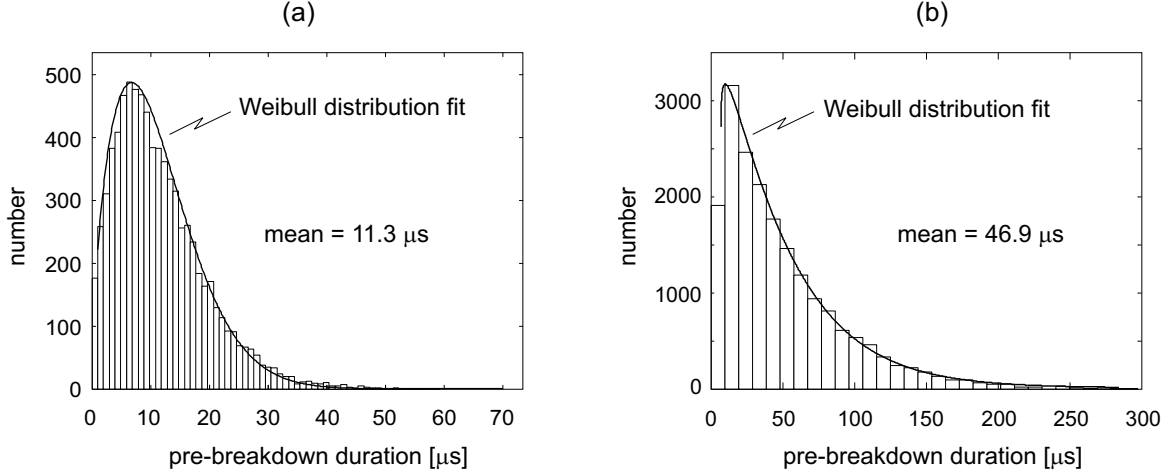


Figure 4.7: Histograms of the pre-breakdown duration. (a) Statistics on 8'000 similar discharges: 6 A, 8 μs on-time, 8 μs off-time, -200 V, in water; (b) statistics on 19'000 similar discharges: 6 A, 50 μs on-time, 50 μs off-time, +200 V, in water.

The distribution of pre-breakdown duration can be well fitted with the *Weibull distribution* [118]. The probability density function of this type of distribution is

$$P(x|a, b) = a b x^{b-1} \cdot \exp(-ax^b) \quad (x > 0),$$

where a and b are constant parameters. The general shape of this distribution is, starting from zero, an increase to a maximum value, followed by an exponential decay. The Weibull distribution is known for describing, among others, the repartition of the pre-breakdown duration in various dielectric liquids [119, 120]. The breakdown process in EDM has thus a strong stochastic nature, which clearly appears in these measurements. Although we can optimize discharge parameters and experimental conditions to reduce the mean pre-breakdown duration (addition of electron scavengers in the dielectric for example), we will always have distributed values. The poor reproducibility of EDM discharges can undoubtedly be related to this stochastic aspect of the breakdown.

As we will see in the next chapter, the stochastic nature of the breakdown has a practical consequence for plasma imaging. Since it is impossible to predict precisely when the next breakdown will occur, the camera opening for the exposure of a given discharge can only be triggered with the beginning of this very discharge. We cannot anticipate the beginning of the next discharge, as could be done with pulsed RF plasmas, for example.

Chapter 5

Imaging diagnostics of EDM discharges

The first section of this chapter presents images taken from films that were recorded during the EDM machining process. Images of the plasma itself are analyzed in the second section. Finally, the third and fourth sections are respectively dedicated to images of the plasma at the beginning and at the end of the discharge.

5.1 Imaging of the EDM process

5.1.1 Erosion

Figure 5.1 shows a typical example of what can be observed during machining.

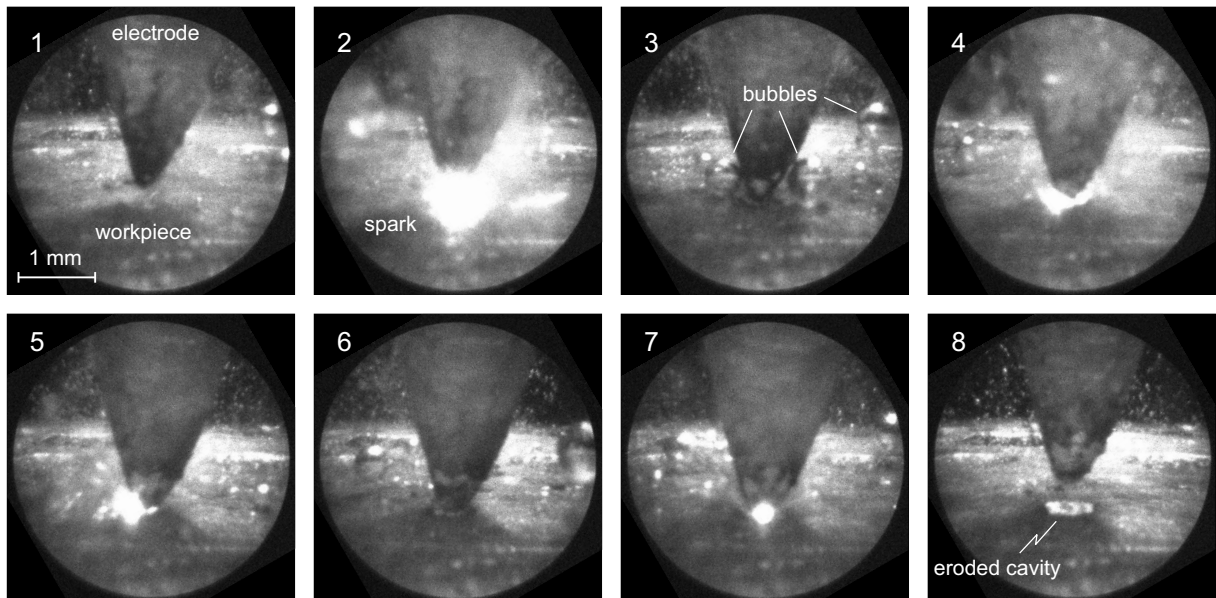


Figure 5.1: Images taken during the machining process (1 ms exposure; Cu electrode, steel workpiece, 8 A, 50 μ s on-time, + 200 V, water). Sparks and bubbles are clearly visible. The duration of the whole sequence is approximatively 40 s.

The workpiece surface, completely flat on image 1 before machining, is slightly eroded by the successive sparks. After a few tens of seconds of machining, i.e. after a few hundreds of thousands of sparks, a small cavity is formed (image 8). Some of these sparks are visible on images 2, 4, 5 and 7. The heat released by the discharges generates vapor bubbles close to the electrode gap. They can be clearly seen on images 3, 6 and 7 for example.

5.1.2 Bubbles

Different types of bubbles can be observed. As mentioned in section 4.1, hydrogen bubbles are released during pre-breakdown in water by electrolysis. During machining, the heat of the plasma is generating vapor bubbles, in water as in oil. Images of these different kinds of bubbles are given in figure 5.2.

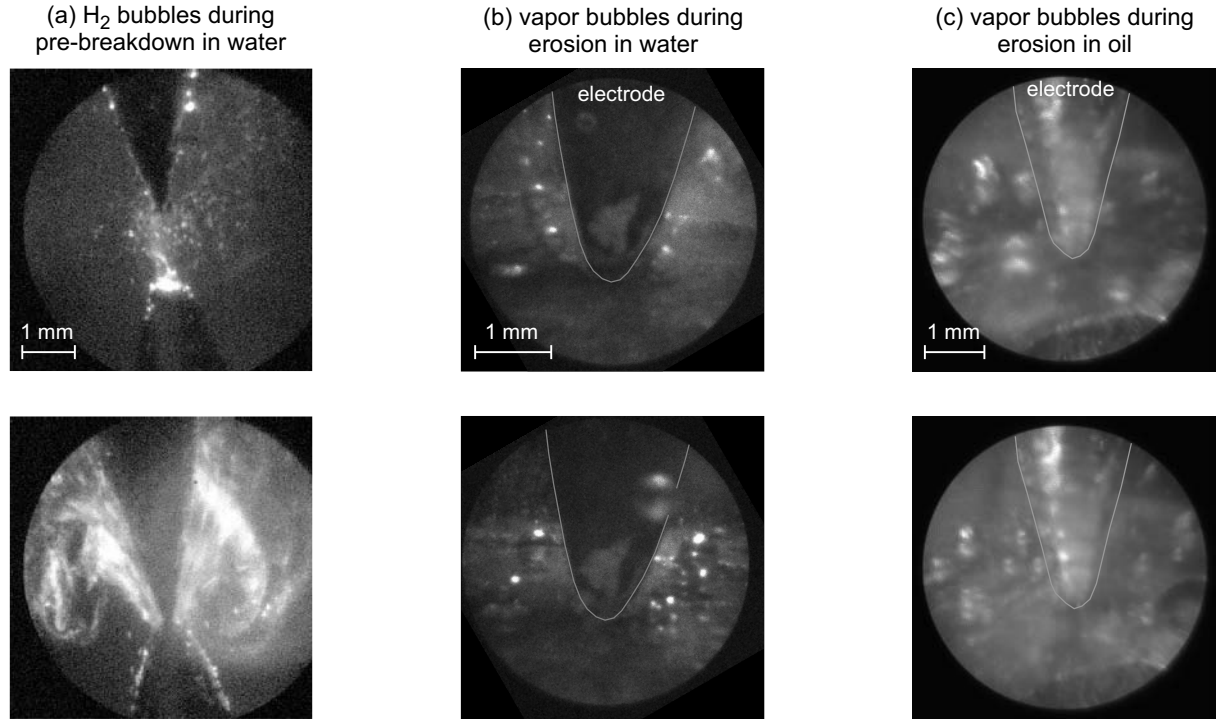


Figure 5.2: Different types of bubbles generated during the EDM process: (a) small hydrogen bubbles created by electrolysis during pre-breakdown in water (large and small gap, + 200 V); (b) water vapor bubbles thermally induced during machining (8 A, 50 μ s); (c) oil vapor bubbles thermally induced during machining (6 A, 6 μ s).

By zooming on the images of figure 5.2 (a), the diameter of the electrolysis bubbles can be roughly estimated around 30 – 100 μ m. The generation of these hydrogen bubbles is strongly enhanced with an increase in the electric field. With a small gap (bottom image of figure 5.2 (a)), one can in fact observe numerous bubbles ejected from the gap with high velocity, leading even to turbulent phenomena (vortices).

On the other hand, the thermally-induced vapor bubbles are much larger. Their diameter is $\sim 500 \mu\text{m}$, in water as in oil (figure 5.2 (b) and (c)). When machining in water, both hydrogen and vapor bubbles are created. This can be seen on figure 5.1, image 6 for example: two large vapor bubbles are visible, along with several small hydrogen bubbles going up on both sides of the pointed electrode. In oil, only large vapor bubbles can be observed.

5.1.3 Short-circuit

Imaging permits also the observation of undesirable phenomena, such as the short-circuit of the electrodes. The phenomenon shown in figure 5.3 has been observed both in water and in oil.

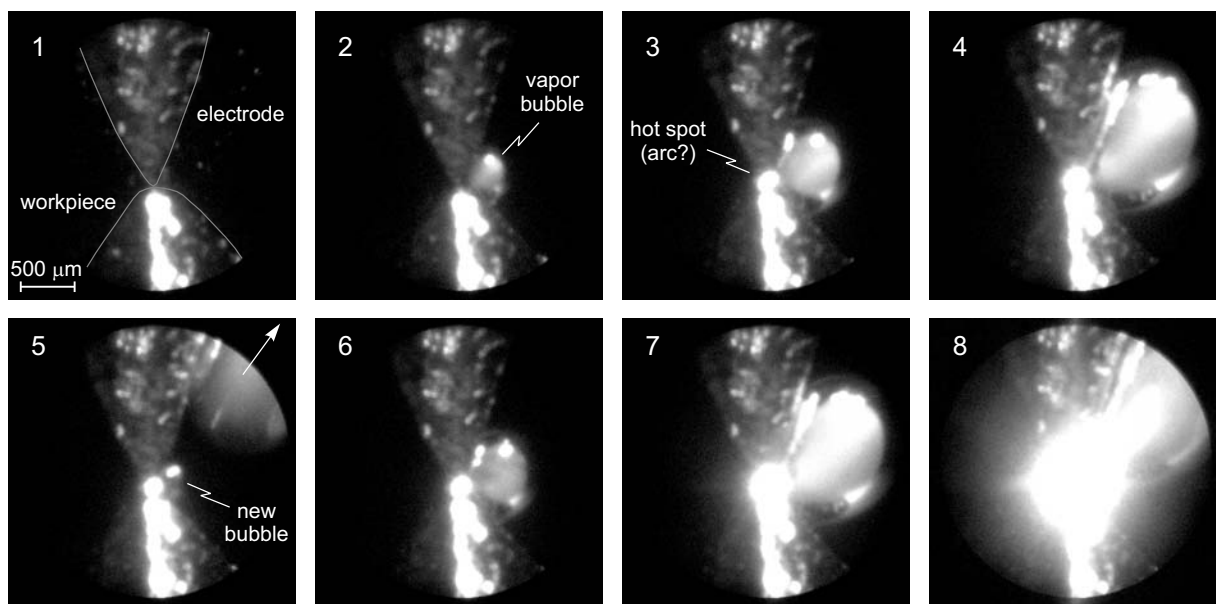


Figure 5.3: Short-circuit, creation of a stable hot spot and continuous generation of large growing vapor bubbles in oil. The duration of the whole sequence is approximately 15 s (images: 9 ms exposure).

A short-circuit occurs when the two electrodes come into contact, or if a conducting debris bridges the gap. If the electrodes are not separated but kept in contact, the current flow heats them by Joule effect. With a point-to-point geometry as in figure 5.3, a hot spot is easily formed between the electrodes, because the current density becomes very high in this region due to their small contact area. The heat released by this hot spot generates a vapor bubble (image 2), just as the sparks do during machining. On image 3, the inter-electrode distance has been slightly increased. The hot spot becomes bright and is probably a small arc. The heat release is then more intense, leading to a growth of the vapor bubble, which remains “attached” to the hot spot (images 3 and 4). Once the bubble reaches a critical size, the buoyancy force is large enough to detach the bubble from the hot spot (image 5). A new bubble is immediately formed, and grows just like

the preceding one (images 6, 7 and 8). This cycle of bubble generation is very stable and will continue repeatedly, unless the electrodes are clearly separated. On images 7 and 8, the inter-electrode distance is further increased. The arc then grows and becomes very bright (image 8). The arc suddenly disappears as soon as the generator can not sustain it anymore, due to a too large gap distance.

5.1.4 Reproducibility

To illustrate the problem of the reproducibility of the discharges (discussed in section 3.6), figure 5.4 shows several images of discharges with the same parameters.

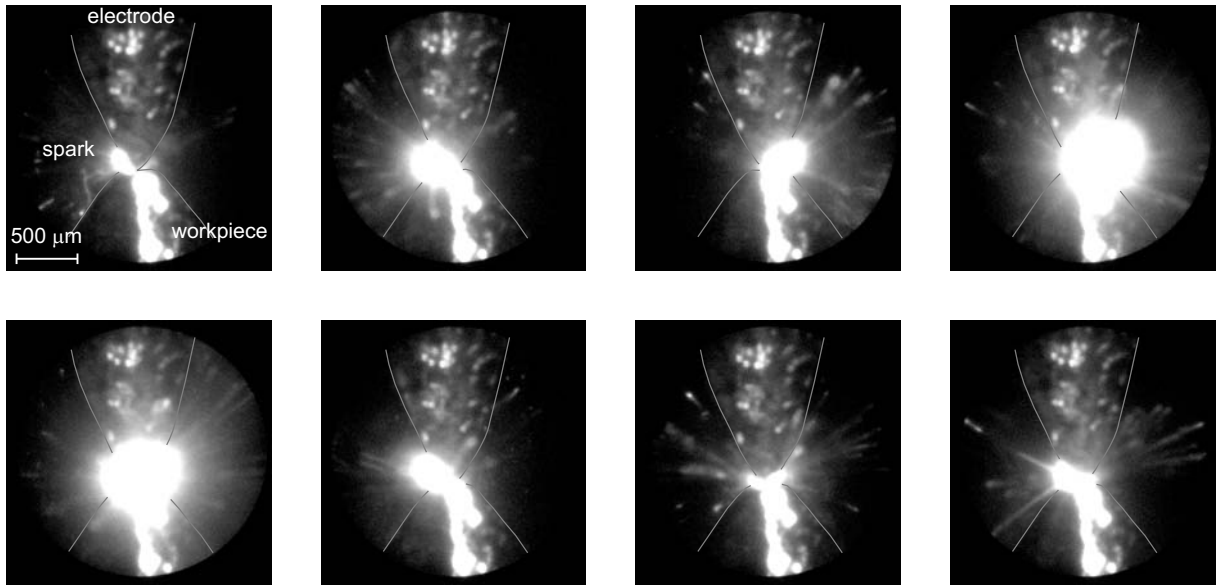


Figure 5.4: Images of similar discharges, illustrating the problem of reproducibility (9 ms exposure; 12 A, 50 μ s, oil). The electrode outlines are drawn.

Even with a point-to-point geometry, the plasma localization strongly changes from one discharge to another. Furthermore, the size of the sparks, and consequently their physical properties, also vary. Therefore, all our measurements were repeated several times. Numerous plasma images were acquired, and the most representative ones are presented in the following sections.

5.2 Plasma imaging

5.2.1 Evolution of the plasma light intensity

Before analyzing images of EDM plasmas, it is important to study the evolution of the plasma light intensity during the discharge. Two examples of such measurements are given in figure 5.5, along with voltage and current measurements.

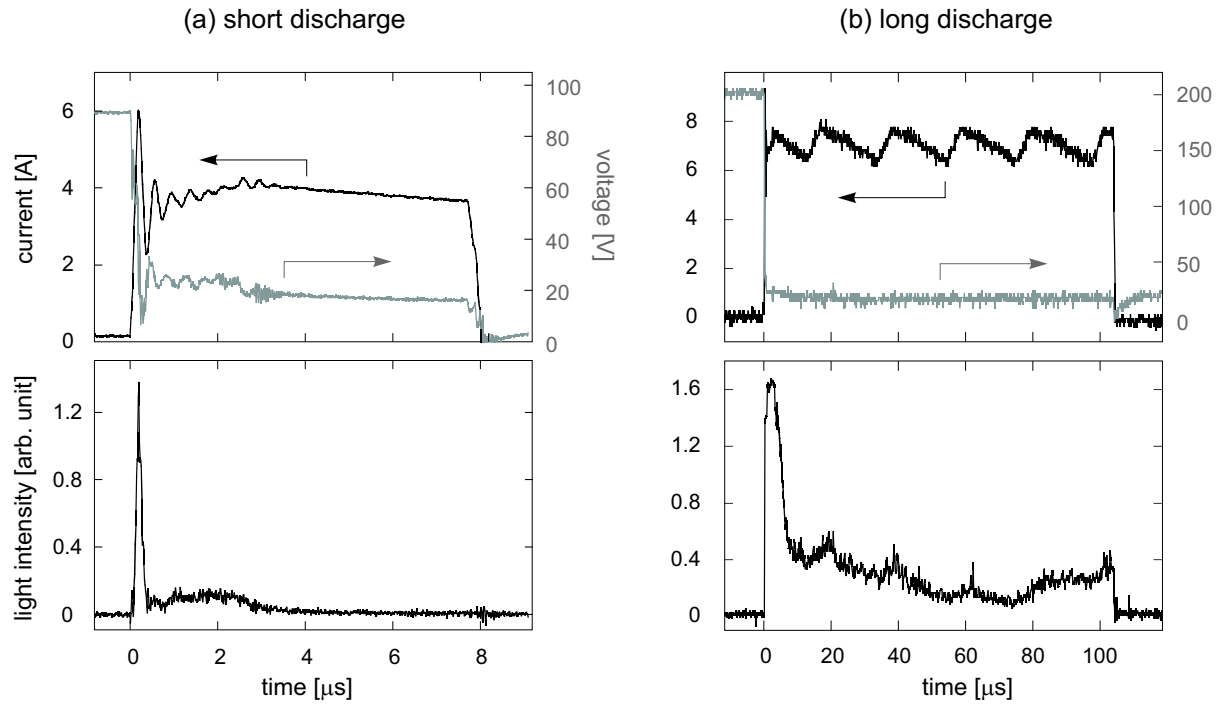


Figure 5.5: Evolution of the plasma light intensity, of the current and of the voltage during a single discharge: (a) short discharge (4 A, 8 μ s, water); (b) long discharge (8 A, 100 μ s, water).

Two phases can be distinguished: the breakdown phase and the discharge phase. The major part of the light is emitted during the breakdown phase, i.e. approximately during the first 500 ns after the breakdown (see figure 5.5 (a)). During the discharge itself, the light emission is 10 to 150 times less intense. In figure 5.5 (b), the first light peak seems to last much longer than 500 ns. This is an artefact due to the saturation of the photomultiplier. For this measurement, the gain of the detector has in fact been set higher in order to better visualize the light emission during the discharge phase. The intensity of the first peak is thus in reality much higher and lasts less than 1 μ s.

The light emission during the discharge phase becomes much more intense when increasing the discharge current. Furthermore, the oscillations observed on light intensity measurements in figure 5.5 (b) are correlated to those on current (the current waveform is caused by the regulation system of the generator). This shows that these two physical values are unsurprisingly interdependent.

From the erosion point of view, the first microsecond seems to be very different from the rest of the discharge. The high intensity of the first light peak suggests that a massive flow of energy is brought to the workpiece during the breakdown phase. Due to the short duration of this event ($< 1 \mu$ s), it is probable that only the workpiece surface is affected by this primary energy flow, while the workpiece bulk remains unaffected. A burst of energy will in fact directly evaporate only the very superficial layers of the workpiece. The bulk is not affected, because it can not absorb this high amount of energy by conduction on such

a short time scale. The bulk will be heated by the plasma during the discharge phase.

Like the workpiece, the electrode is probably also affected by this primary energy flow. A small superficial erosion of the electrode during the breakdown phase could be consistent with the well-known fact that wear mostly occurs at the beginning of the discharge.

The fast and superficial erosion process occurring at the breakdown could be similar to the “thermal runaway” of protrusions on arc cathode surfaces (see § 2.1.3). Protrusions can be evaporated or even explode if the input power is higher than what the electrode can evacuate by conduction. The typical time scale of fast evaporation processes is 1–100 ns, and below 1 ns for explosive processes [56]. Interest in using very short discharges could thus arise in EDM, considering that such fast eroding mechanisms will produce surfaces with very low roughness. A new type of machining could perhaps be developed, with generators capable of producing powerful ultra-short discharges.

5.2.2 Typical plasma image

Contrary to the images of the section 5.1, plasma images are acquired without any external lighting. The measured light comes only from the plasma itself. Figure 5.6 shows a typical image of an EDM plasma. The electrodes have been outlined because they are not visible without the external lighting.

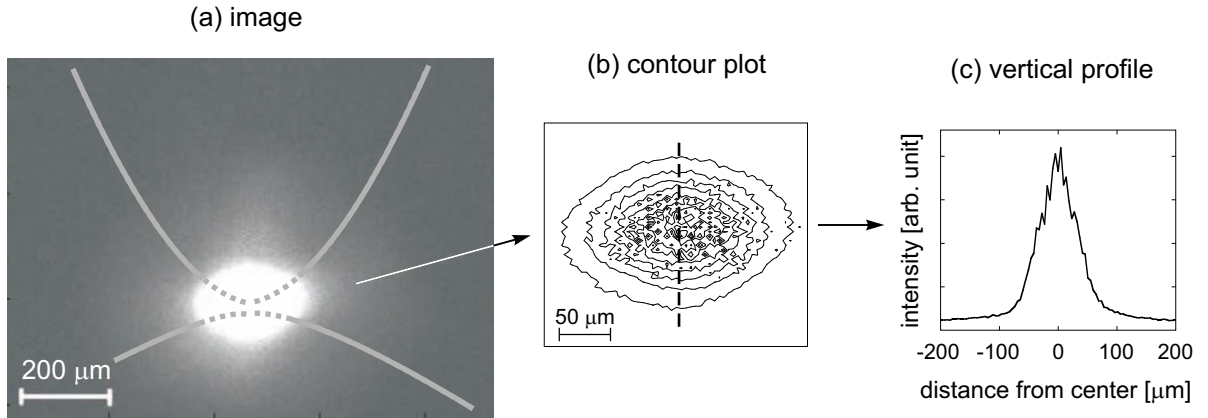


Figure 5.6: (a) Typical plasma image (5 μs exposure, 5 μs delay after breakdown; 24 A, 100 μs , oil), the position of the electrodes is drawn; (b) contour plot of (a); (c) intensity profile of (a) along the vertical axis.

The light emitting region is generally round or oval. As we will see later, its diameter increases with the discharge current. The light mostly originates from a broader region than the gap itself, i.e. the discharge excites a broad volume around the electrode gap.

In order to better analyze the images, it is useful to view them as contour and profile plot, as shown in figure 5.6 (b) and (c). The dots in the center of figure 5.6 (b), and the irregularities in the center of figure 5.6 (c), are not real but due to the individual sampling by the endoscope fibres. There are indeed small spaces between the fibres in the endoscope which do not bring the light to the camera. The brightest zone is the central

region (electrode gap) and the light emission decreases rapidly with distance: at $40\ \mu\text{m}$ from the center, the intensity is halved.

5.2.3 Plasma evolution

The evolution of the plasma size is another delicate point. Care has to be taken for the image treatment and interpretation. First, the light emitting region (excited region) could be broader than the plasma itself (ionized region), and the light could partly be scattered from the liquid in the surrounding of the electrodes. Secondly, the images have to be normalized in intensity. If not, the plasma seems to be bigger during the first microsecond, simply because the light intensity at this stage is much higher. Finally, we cannot acquire more than one image during a single discharge, because the readout time of the CCD camera is much longer than the discharge on-time. Thus, each image will be acquired during a different discharge. Since the discharges are poorly reproducible, the comparison between the images becomes difficult. However, figure 5.7 shows plasma images at different stages of the discharge.

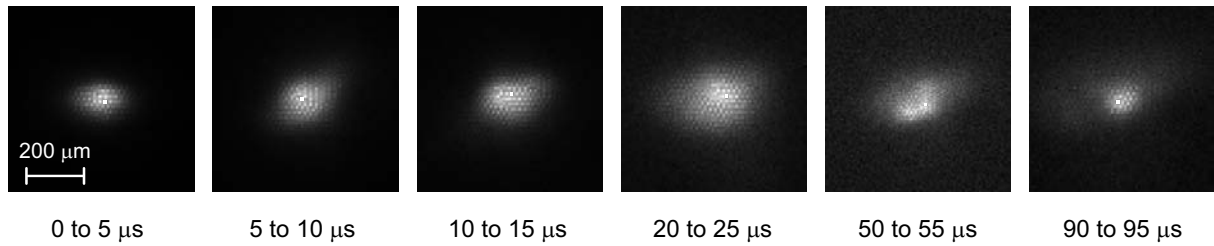


Figure 5.7: Plasma images at different times during the discharge ($5\ \mu\text{s}$ exposure, variable delay after breakdown; $24\ \text{A}$, $100\ \mu\text{s}$, water). The images are normalized in intensity. Each image is obtained during a different discharge.

There is a slight growth of the emitting region, but its size remains fairly constant during the whole discharge. Similar measurements have been reported elsewhere [27, 121]. The emitting region was also found to grow with time. Even if the light emitting region could be larger than the plasma itself, it is likely that these images reflect an increase in the plasma size during the discharge, as expected from simulations [40, 122].

Other results confirm this conclusion. Measurements of crater radius on the cathode surface have been made for different discharge on-time [123]. The crater radius $r_c(t)$, supposed to be close to the plasma radius $r_p(t)$, is found to increase with $t^{0.2}$. In previous models, $r_p(t)$ was assumed to grow with $t^{3/4}$ [40], or with $\tanh(t)$ [124]. We will not propose any relation here. In our opinion, the reproducibility of our images is not good enough to propose any numerical relation, which would be an over-interpretation of the measurements.

5.2.4 Effect of the discharge current

As shown in figure 5.8, the diameter of the light emitting region increases with the discharge current, being roughly from 150 to $400\ \mu\text{m}$ for a current increase from 3 to $48\ \text{A}$.

Thus, the plasma size most likely also increases with the discharge current. Again, this can be correlated with the fact that discharges with high current produce larger craters than discharges with low current.

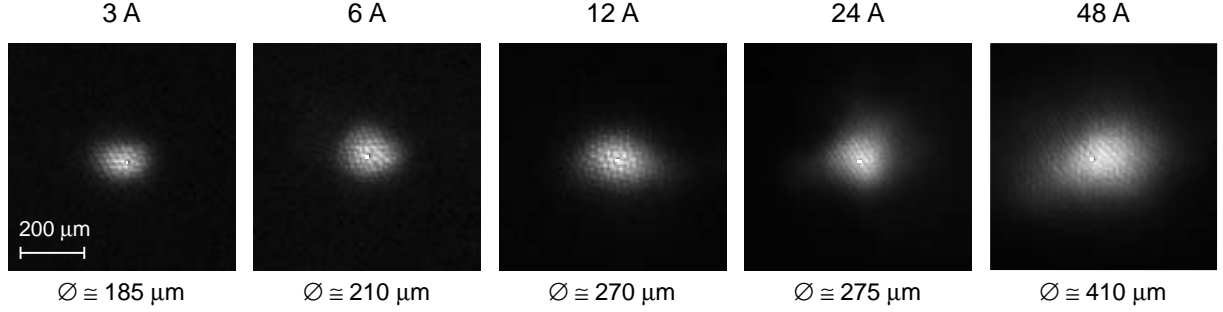


Figure 5.8: Plasma images for different discharge currents and estimation of the emitting region diameter ($5 \mu\text{s}$ exposure, $10 \mu\text{s}$ delay after breakdown; $100 \mu\text{s}$, water). The images are normalized in intensity.

5.2.5 H_α emission

As we will see in chapter 6, the hydrogen H_α line is the dominant contribution in EDM plasma line emission. Intensity evolution and imaging of the H_α emission has been measured by using a band-pass filter centered around 656 nm . The filter is placed between the optical fibre and the photomultiplier for intensity measurements, and between the endoscope and the camera for imaging. Results are given in figure 5.9.

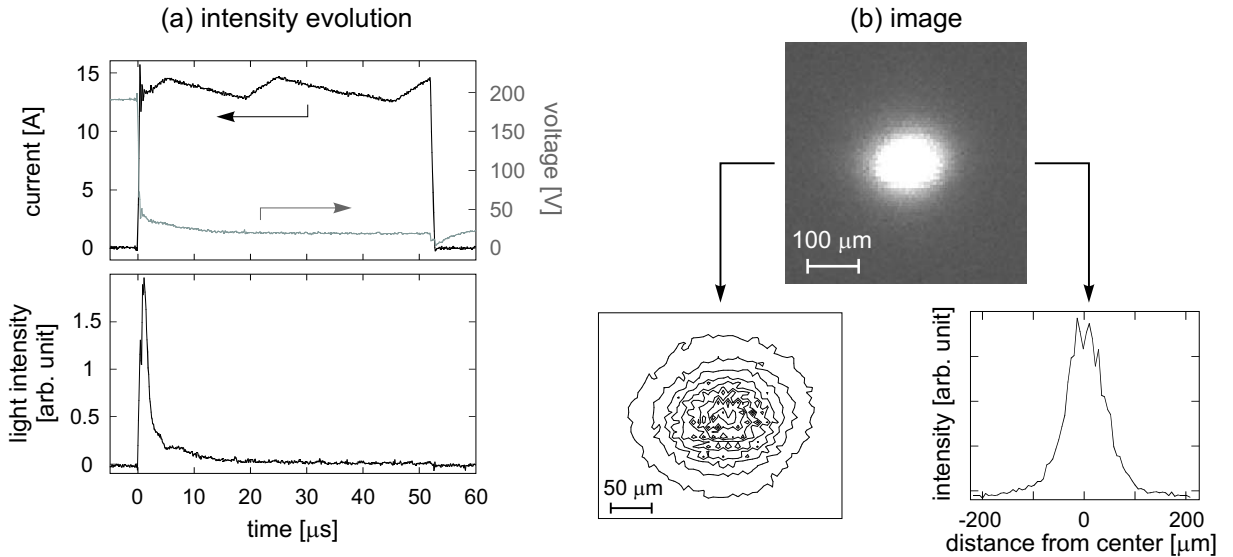


Figure 5.9: Emission of the H_α line: (a) intensity evolution; (b) typical image ($5 \mu\text{s}$ exposure, $0 \mu\text{s}$ delay), contour plot and vertical intensity profile. Discharge parameters: 12 A , $50 \mu\text{s}$, water.

The intensity evolution of this line is similar to the evolution of the total emission, given previously in figure 5.5. The major part of the light is emitted during the breakdown phase. Similarly, the images obtained with the H_α filter are very similar to those obtained without it (see figure 5.6). The emitting region has the same shape, size and intensity profiles. We can thus conclude that the H_α line is emitted by the whole plasma volume.

5.3 Beginning of the discharge : Fast imaging

Figure 5.10 shows fast imaging of the first 300 ns of the discharge, obtained with the ICCD camera. This time interval corresponds to the emission of the first light peak and to the first fast current rise (see figure 5.5 (a)). This interval is thus important in the plasma evolution: it is during the very beginning of the discharge that the plasma is forming and that a high amount of energy is brought into it.

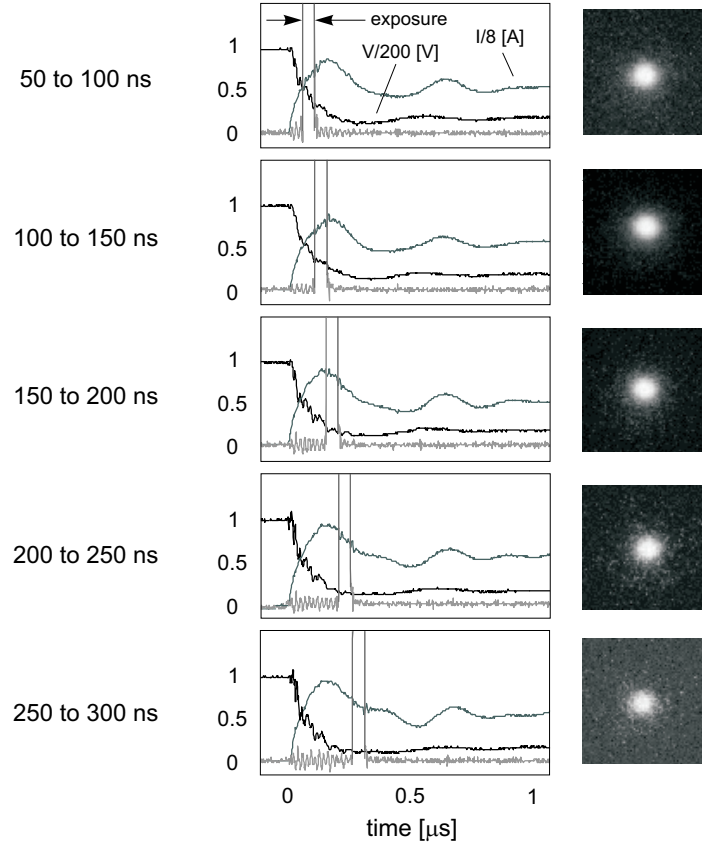


Figure 5.10: Fast imaging of the discharge beginning along with current and voltage evolution (50 ns exposure, variable delay; 6 A, water). The images are normalized in intensity. Each image is obtained during a different discharge.

The exposure time is 50 ns for each image, with variable delays. There is always a 50 ns intrinsic delay between the trigger signal (current rise at the breakdown) and the camera opening, due to gating electronics and cables. Since we cannot anticipate the breakdown

for the camera triggering as previously mentioned in section 4.3, the first image can only be acquired 50 ns after the breakdown.

Between 100 and 200 ns after the breakdown, the current reaches its maximum. The light intensity is also at its maximum. However, on the plasma images, no clear evolution is visible from 50 to 300 ns: size and geometry remain constant. Images obtained with delays longer than 300 ns are not shown here, but they are similar to those of the figure 5.10. This shows that the plasma develops very rapidly (within 50 ns) after the breakdown, and then remains quite stable.

5.4 End of the discharge and post-discharge

Since the major part of the workpiece material is removed at the end of the discharge when the plasma collapses, the transition from the discharge to the post-discharge is particularly interesting to study. This stage in the EDM process is certainly crucial for the optimization of the material removal rate.

The evolution of the light intensity at the transition and during the post-discharge is presented in figure 5.11.

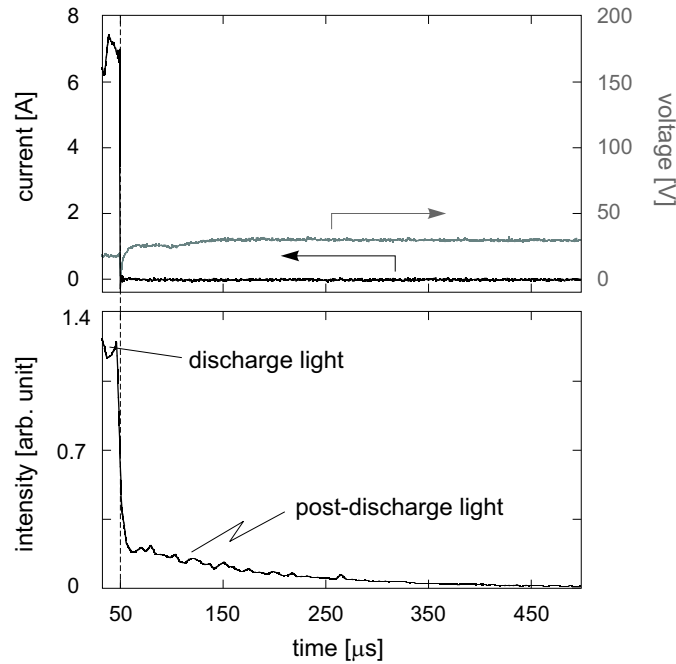


Figure 5.11: Evolution of the light intensity during a post-discharge (discharge: 6 A, 50 μ s, water).

As soon as the current is shut down, it drops rapidly to zero, and the light intensity is simultaneously also dropping fast. But there is still a weak slowly-decaying light emission, typically until 300 μ s after the end of the discharge. The corresponding images of the transition are given in figure 5.12.

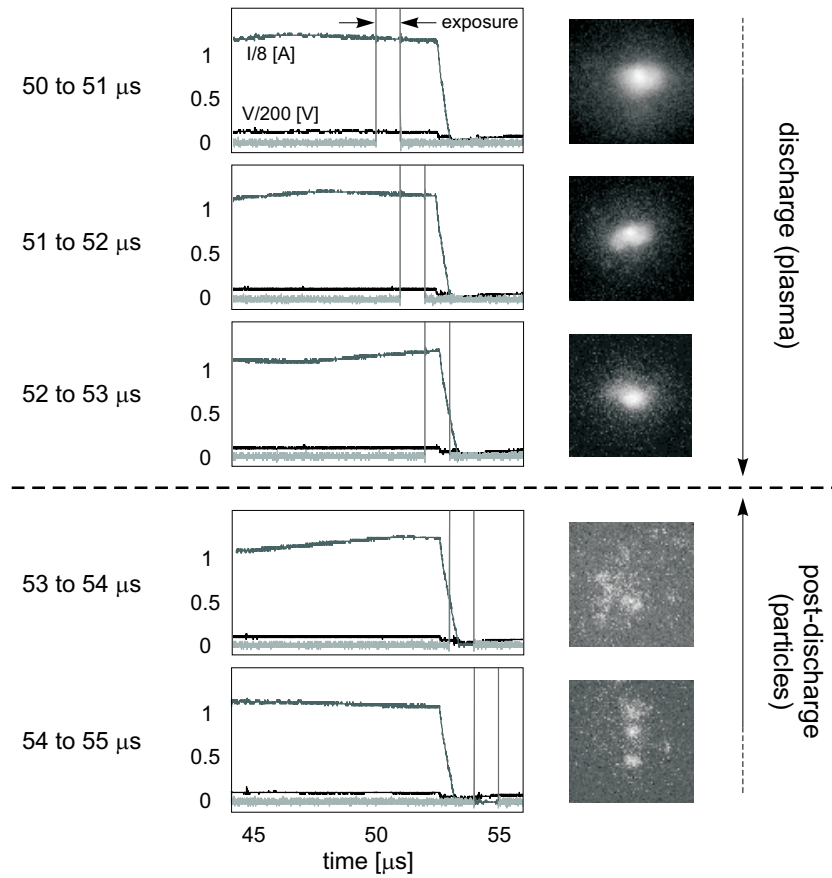


Figure 5.12: Images of the transition between the discharge and the post-discharge, along with current and voltage evolution (1 μs exposure, variable delay; 12 A, 50 μs , water). The images are normalized in intensity. Each image is obtained during a different discharge.

As long as the discharge current is established, the plasma is visible as a bright spot. When the current drops down, the disappearance of the plasma is almost immediate. The plasma collapse is thus a very fast phenomenon.

Images of the post-discharge in figure 5.12 are less clear, due to the weak intensity of the light emitted during this period. The objects which are emitting light are difficult to identify. The quality of the images are much improved by setting the sensitivity of the ICCD camera at its maximum and by increasing the exposure time. It is also easier to do the measurements in oil, because the numerous bubbles present in water strongly perturb the acquisition of the light. Some examples of better post-discharge images are shown in figure 5.13.

It becomes clearer that the light emitted after the discharge is due to particles of heated metal. These particles come from the molten metal pool created in the workpiece during the discharge, and are then removed from the workpiece and ejected in the dielectric when the discharge is shut down. We see their path and not only luminous dots, because they are moving during the camera exposure. These explosions of particles were also clearly

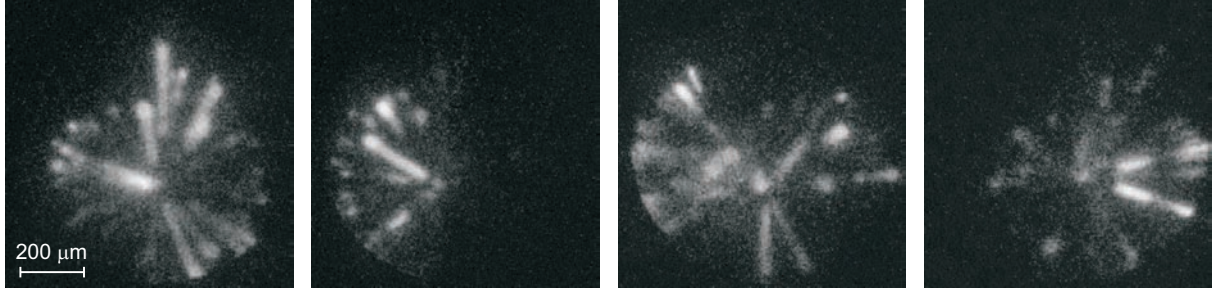


Figure 5.13: Incandescence of the removed particles after a discharge. Each image is taken during a single post-discharge ($100\ \mu\text{s}$ exposure; 12 A, $50\ \mu\text{s}$, oil).

visible on figure 5.4. However, on these previous images, the exposure time was long enough to record both the spark and the post-discharge. Therefore, the interpretation of these luminous paths was not obvious. They could have been attributed to bubbles for example, which would scatter the light of the spark. On the other hand, images of figure 5.13 are time-resolved and the light is acquired only during post-discharges. The interpretation is thus less ambiguous.

In order to confirm the hypothesis of the metal particles, optical emission spectroscopy of the post-discharge light has been performed. An example of the spectrum is shown in figure 5.14.

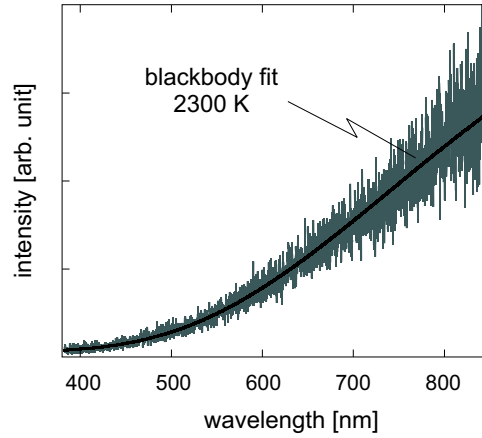


Figure 5.14: Optical emission spectrum of the post-discharge light, with a 2'300 K blackbody fit. The light measurement is time integrated over thousands of post-discharges ($50\ \mu\text{s}$ exposure, 150 g/mm grating; 16 A, $50\ \mu\text{s}$, oil).

Spectroscopy shows that the post-discharge light emission is close to a blackbody radiation, which confirms that the emitters are hot metal particles. The spectrum in figure 5.14 is quite noisy, due to the low intensity of the light emission. Fitting several post-discharge spectra with Planck's law, the temperature of the emitters is found to be around 2'200 K (± 100 K). Since the melting point of steel is $\sim 1'700$ K, the particles are still in a liquid state in the very beginning of the post-discharge. The temperature found

is consistent with metallurgical analyses of the modified layers of the workpiece [25, 125]. In these studies, the maximum temperature of the workpiece surface reached during the EDM process has been estimated to be around 3'000 K.

The particle size can be measured on the images. We found that the largest particles have a diameter of $\sim 30 \mu\text{m}$, which is in good agreement with previous work on spark-eroded particles [126, 127]. The particle speed can also be estimated from images. The maximum speed is around 3 m/s. Since the particles move in the liquid, their trajectories and speed can be affected if a liquid flow velocity is imposed.

Chapter 6

Optical emission spectroscopy of EDM plasmas

The influence of the discharge parameters on the emission spectra are analyzed in the first section, which presents measurements integrated over thousands of whole discharges. The evolution of the spectra during the discharge duration is shown in the second section, with time-resolved measurements. Spatially-resolved spectra are presented in the third section. Finally, time- *and* spatially-resolved measurements are given in the fourth section.

6.1 Time-integrated emission spectra

6.1.1 Typical spectrum

An example of an optical spectrum emitted by the EDM plasma is shown in figure 6.1.

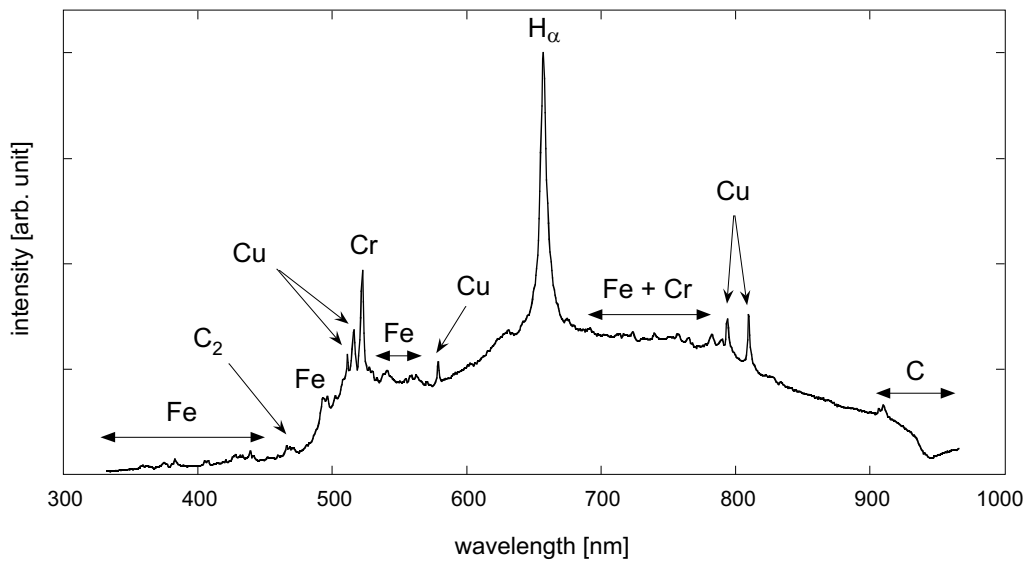


Figure 6.1: Typical emission spectrum (Cu/steel, 12 A, 2 μ s, oil, 150 g/mm grating).

The dominant line is the Balmer H_α line emitted by atomic hydrogen, which comes from the cracking of the dielectric molecules. Some lines of atomic carbon and C_2 molecules (Swan system) are also visible. This indicates that the organic molecules of oil are almost completely cracked by the discharge. As previously mentioned in § 5.2.5, imaging showed that the H_α line is emitted by the whole plasma volume. This can be understood considering the fact that the plasma is formed by cracking and ionizing the dielectric molecules and atoms. Since the hydrogen source is the dielectric, hydrogen atoms are present everywhere in the plasma. Although the H_α line is dominant, the remaining Balmer series lines such as H_β (486.13 nm) or H_γ (434.05 nm) are not observed. This remarkable point will be discussed later, in section 7.2.

The plasma is contaminated by impurities: several lines of atomic copper from the electrode are present, along with many lines originating from atomic iron, chromium and carbon of the removed material of the steel workpiece. These lines can be seen in more detail in figure 6.2.

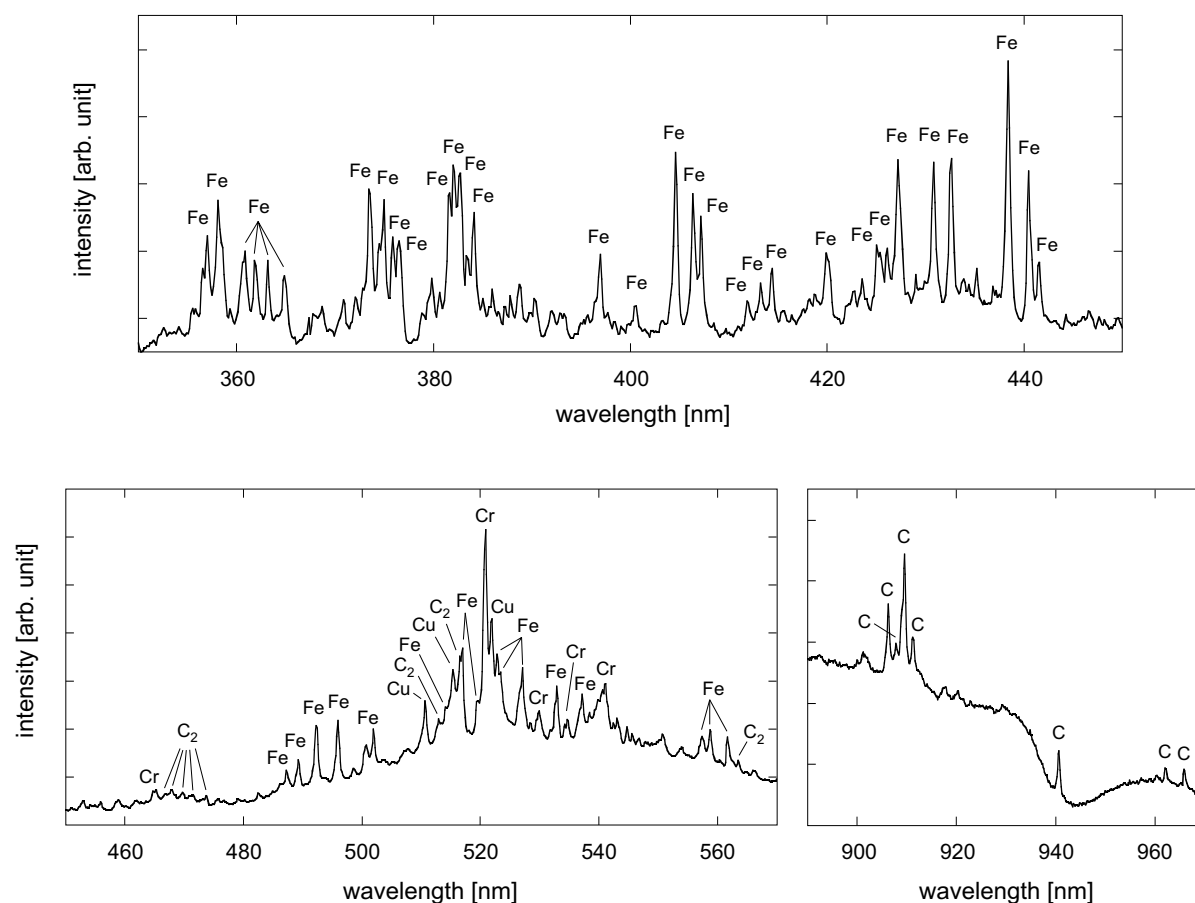


Figure 6.2: Typical emission spectrum, details (Cu/steel, 12 A, 100 μ s, oil, 600 g/mm grating).

The fact that all observed lines are atomic lines (along with a few neutral molecular lines) and that no ionic lines are visible, is a first indication that the plasma is cold. The excitation of ions requires indeed higher energy than the excitation of atoms. Furthermore,

atoms and ions of metallic elements are easily excited, more easily than those of non-metallic elements. For example, the excited state energies of visible transitions of Fe atoms and of Fe^+ ions are respectively around 3 and 11 eV (from the ground state of atoms and ions respectively), but for C atoms and for C^+ ions they are respectively around 8 and 22 eV [128,129]. Thus, the absence of ionic lines of iron, copper or chromium indicates clearly that the plasma temperature is low. Since sparks in gases are known to be highly ionized plasmas [49], EDM sparks should nevertheless also be fairly ionized.

The low excitation energy of metallic atoms explains the abundance and the relatively high intensity of their lines in the EDM plasma emission (see for example the numerous Fe lines in figure 6.2). It should be noted that this abundance does not mean that a large amount of metal is present in the plasma. In electric arcs for example, the light emission is dominated by metallic lines already with a contamination of a few percents of metal. It is also well known that metallic impurities strongly cool down fusion plasmas in tokamaks, because of their strong radiation. Thus, a quantitative estimation of the metallic contamination in the EDM plasma from our spectra would be hazardous.

An intense broadband continuum radiation is also observed. The origin of this radiation remains unclear. Blackbody fits do not match well with our measurements. Thus, a continuous emission by heated electrodes or metal particles is unlikely. It is more probable that this continuum is due to free-bound transitions, i.e. radiation emitted during recombination processes. Free-free radiation is also another plausible source. Since molecules generally emit a broadband spectrum, molecules or fragments of molecules from the dielectric certainly also participate to the continuum [34,63].

6.1.2 Effect of the dielectric

Figure 6.3 shows emission spectra obtained in different dielectrics.

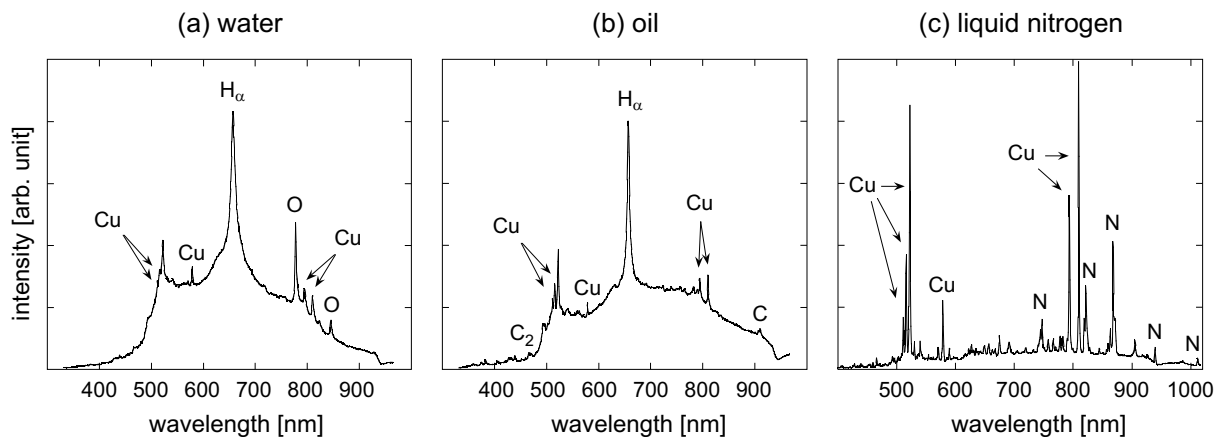


Figure 6.3: Effect of the dielectric on the emission spectrum (Cu/steel, 150 g/mm grating): (a) water, 12 A, 2 μs ; (b) oil, 12 A, 2 μs ; (c) liquid nitrogen, 48 A, 2 μs .

As mentioned previously, the discharge cracks the dielectric molecules, even the strong triple bond of nitrogen N_2 molecules. We observe atomic hydrogen and oxygen lines from water; atomic hydrogen, atomic carbon and C_2 lines from oil; atomic nitrogen lines from liquid nitrogen. The dominant lines in figure 6.3 (c) are copper lines, because we have more electrode wear than workpiece erosion under these experimental conditions in liquid nitrogen.

The dielectric cleanliness has an effect on the emission spectrum, as shown in figure 6.4. The continuum radiation is found to be more intense in clean dielectric than in dielectric contaminated with eroded particles. Unsurprisingly, lines emitted by Fe, Cr and Cu follow the opposite tendency. The high intensity of the continuum in clean dielectric is not clearly understood. It is probably because the contribution of dielectric molecules (continuous radiation) dominates the radiation of metallic elements in a clean dielectric.

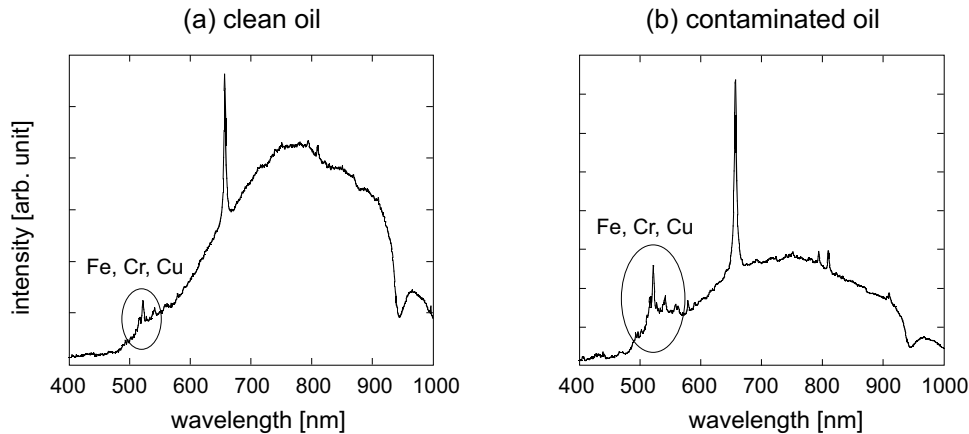


Figure 6.4: Effect of the dielectric cleanliness on the emission spectrum (Cu/steel, 12 A, 50 μ s, 150 g/mm grating): (a) clean oil; (b) oil contaminated with eroded particles.

The addition of metallic powders to the dielectric has also been briefly investigated with spectroscopy. The aim of adding powders is to deposit new layers on the workpiece surface and to improve its quality *during* the machining process. For example, the addition of graphite nano-particles is found to improve the hardness of the white layer and to reduce the number of cracks in it [125]. The addition of aluminium and tungsten powders does not significantly modify the emission spectrum. New Al and W atomic lines are simply added. Thus, the plasma properties are certainly not drastically changed by the introduction of powders. It is rather the breakdown process and the surface quality which can be influenced by the powders, depending on their size and composition.

6.1.3 Effect of the electrode material

Emission spectra obtained with an electrode in copper, in graphite and in tungsten are shown in figure 6.5. The electrode material contaminates the plasma, and lines of respectively atomic copper, of atomic carbon and C_2 , and of atomic tungsten are emitted. With a graphite electrode, the Swan bands of C_2 and the C lines are much stronger than

in figure 6.1 for example, because the carbon contamination of the plasma due to the graphite electrode is much greater than the carbon produced by the cracking of the oil. The tungsten lines are very difficult to observe because they are located in the same spectral region as many iron lines, which are more intense.

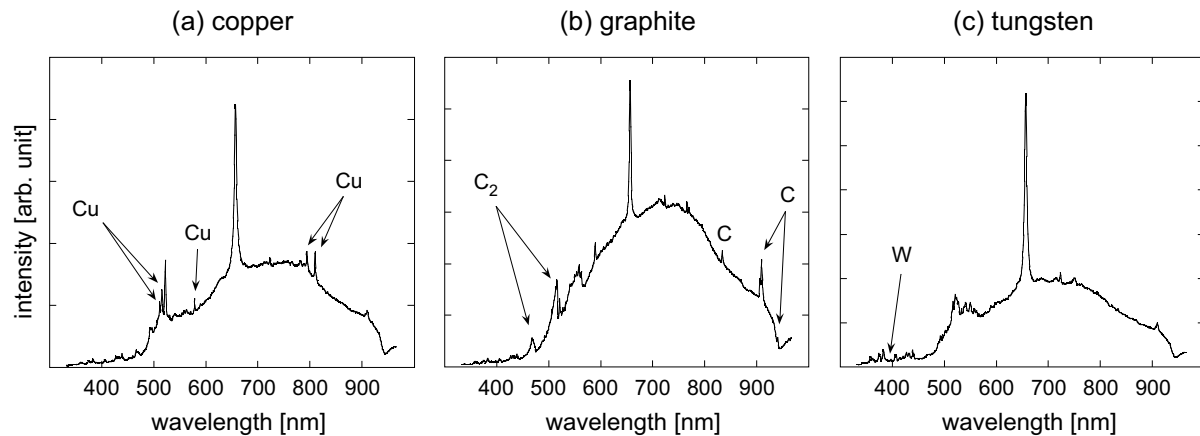


Figure 6.5: Effect of the electrode material on the emission spectrum (12 A, 5 μ s, oil, 150 g/mm grating): (a) Cu/steel; (b) graphite/steel; (c) W/steel.

The use of a zinc electrode produces a spectrum quite different from the others, as shown in figure 6.6. It should be noted that zinc is never used as electrode material in die-sinking machines, but only as a coating layer of the wire in wire-cutting machines.

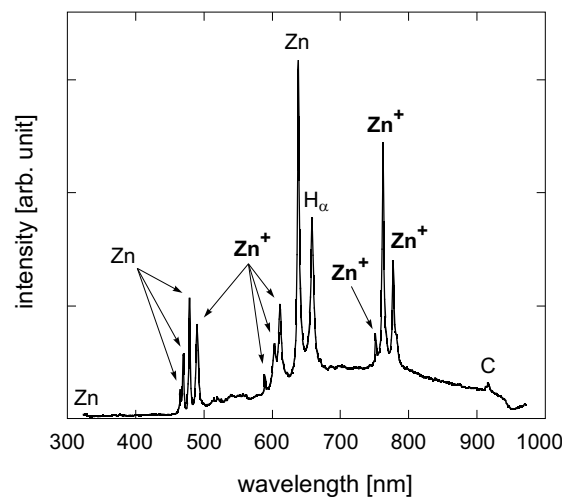


Figure 6.6: Emission spectrum with a zinc electrode (Zn/steel, 12 A, 12 μ s, -200 V, oil, 150 g/mm grating).

In addition to the H_α line and C lines, both atomic Zn lines *and* ionic Zn^+ lines are emitted, with high intensities. Zinc is the only material tested in this work that produces ionic lines. The wavelengths of these lines, along with those of all other main

lines observed in EDM spectra, are given in table 6.1. The different behavior of zinc comes from its physical properties. Excited states energies of Zn^+ transitions already exist from 8 eV [128]. Thus, Zn^+ ions are more easily excited than Fe^+ , Cu^+ or Cr^+ ions.

Moreover, this material has a low melting and boiling temperature (692 K and 1184 K respectively), much lower than those of copper for example (1356 K and 2839 K respectively). Zinc has also a vapor pressure ~ 400 times higher than copper. Consequently, the wear of a zinc electrode is high during the EDM process, and that explains why this material is never chosen for real die-sinking EDM operations. A theoretical study based on experimental data showed that the energy balance at the cathode is strongly related to the electrode material properties [28]. It is demonstrated in this work that a zinc cathode creates a higher density current and a lower ionic current fraction than other cathode materials, due to the particular physical properties of zinc.

species	wavelengths [nm]
H	656.3 (H_α)
C	833.5, 906.2, 909.5, 911.2, 940.6, 962.1, 965.8
C_2	467.9, 468.5, 469.8, 471.5, 473.7, 512.9, 516.5, 563.6 (Swan system)
O	777.2, 777.4, 777.5, 844.6
N	746.8, 821.6, 868.0, 939.3, 1011.5
Cu	510.6, 515.3, 521.8, 578.2, 793.3, 809.3
W	400.9, 407.4, 426.9, 429.5
Fe	358.1, 382.0, 404.6, 438.4, 495.8, 516.7, 527.0, 561.6, 718.7, 751.1, 822.0
Cr	520.5, 520.6, 520.8, 529.8, 541.0, 723.6, 740.0
Zn	468.0, 472.2, 481.1, 636.2
Zn^+	491.2, 589.4, 602.1, 610.2, 747.9, 758.9, 773.3

Table 6.1: Wavelengths of the main lines emitted by EDM plasmas [128–132].

6.1.4 Effect of the electrode polarity

The emission spectra also give qualitative information about the electrode wear and the workpiece erosion. Figure 6.7 shows two spectra measured under the same experimental conditions, except for the electrode polarity.

In figure 6.7 (a), the tungsten electrode is positively polarized with respect to the workpiece. In this configuration, the wear of the electrode is very strong. In the other configuration where the workpiece is positively polarized with respect to the electrode (figure 6.7 (b)), the erosion is more effective and the electrode wears much less. The polarity has a clear influence on spectra. With negative electrode polarity, the iron lines of the group around 520 nm are much more intense than with positive polarity. If we consider the H_α line as a reference of intensity (its intensity does not depend on erosion or wear but originates only from the dielectric), the iron lines show clearly that the erosion is more efficient with negative polarity. If we look at the region between 350 and 450 nm, it

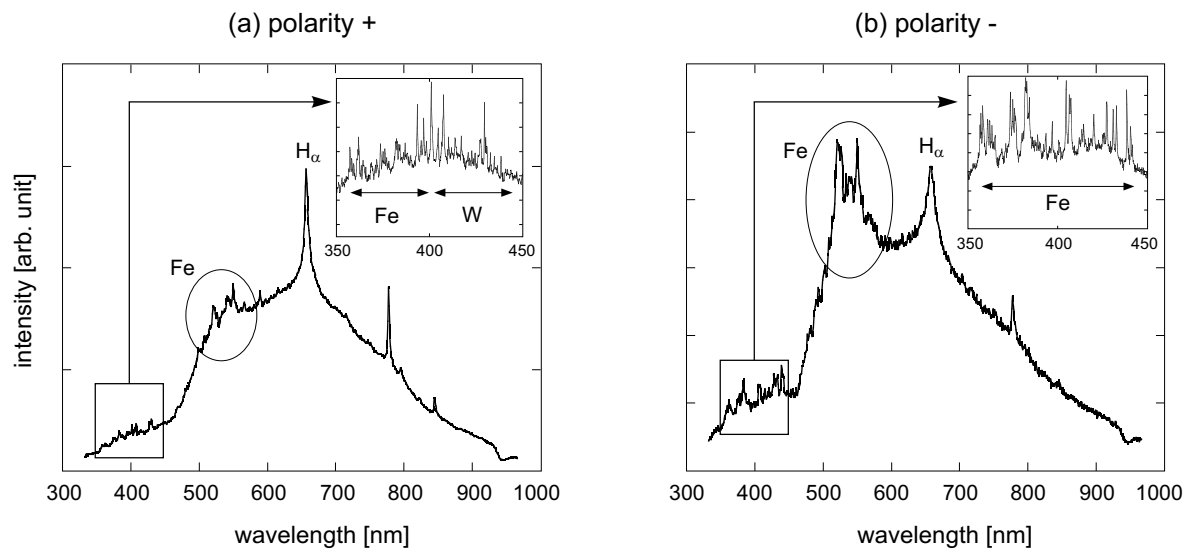


Figure 6.7: Effect of the electrode polarity on the emission spectrum (W/steel, 1 A, 100 μ s, water, 150 and 600 g/mm gratings): (a) positive polarity; (b) negative polarity.

is obvious that the wear is stronger with positive polarity: in (a) several tungsten and iron lines are visible with comparable intensities, in (b) the tungsten lines are no longer visible and the iron lines are more intense. Note that these conclusions are only qualitative, since it is difficult to deduce the quantities of materials removed from these spectra.

6.1.5 Effect of the discharge current

Three emission spectra obtained with different discharge currents are presented in figure 6.8.

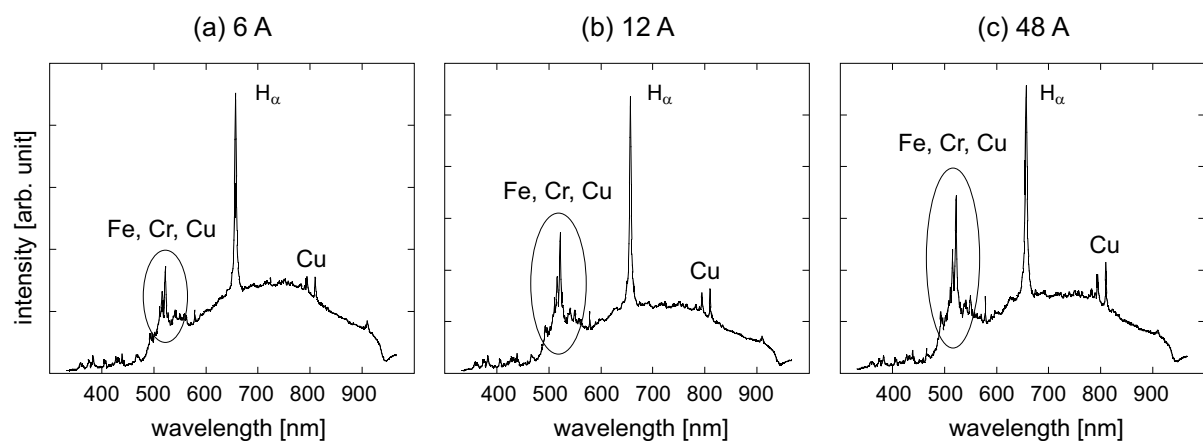


Figure 6.8: Effect of the discharge current on the emission spectrum (Cu/steel, 12 μ s, oil, 150 g/mm grating): (a) 6 A; (b) 12 A; (c) 48 A.

Increasing the discharge current strongly enhances the intensity of the emitted light. But from the spectroscopic point of view, the increase in the current has little effect. It only increases the intensities of the metallic lines. This can be understood by considering that discharges with high current produce large craters and remove more material than low current discharges.

6.1.6 Effect of the discharge on-time

The discharge on-time has a significant influence on the emission spectrum. Figure 6.9 (a) and (b) are spectra for two different on-times of Isopulse discharges, where the current is controlled and maintained constant during the discharge. To produce shorter discharges, we use the generator in the capacitive mode (see section 3.1). Figure 6.9 (c) is the spectrum of discharges produced in the capacitive mode with a 10 nF capacitor.

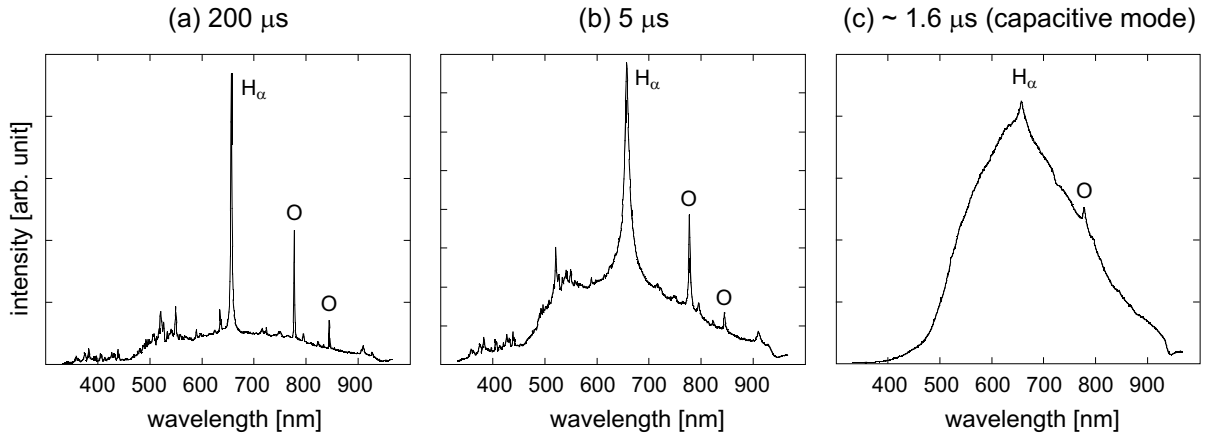


Figure 6.9: Effect of the discharge on-time on the emission spectrum (Cu/steel, water, 150 g/mm grating): (a) 200 μs , 12 A; (b) 5 μs , 12 A; (c) discharges produced in the capacitive mode, $\sim 1.6 \mu\text{s}$, ~ 6 A.

The broadening of the H_α line increases drastically with decreasing on-time as shown in figures 6.9 (a) and (b). The FWHM of the H_α line reaches almost 10 nm in figure 6.9 (b). Such an important broadening can only be due to dynamic Stark broadening, which dominates other broadening mechanisms under these conditions. The H_α line is also shifted to higher wavelengths with decreasing on-time. The measured values of FWHM and line shift are a sign of an extremely high electron density, in particular for brief discharges and thus for the beginning of any discharge. Because the presented spectra are time-integrated, the evolution of electron density can not be directly determined from these FWHM measurements.

For discharges shorter than 2 μs , the plasma is so dense that almost all the atomic lines are completely merged into one broad continuum. We hardly distinguish on figure 6.9 (c) the H_α line, two oxygen lines and two copper lines. This continuum is of another nature than the continuum observed on the previous spectra. It is created by a degeneracy of atomic lines, due to the high plasma density. Extreme densities “destroy” the upper

energy levels of the atoms, and the free-bound radiation becomes more important than line radiation [133, 134]. This effect will be discussed in more detail later, in section 7.2.

6.1.7 First estimation of electron density and temperature

With a H_α FWHM of almost 10 nm for short discharges (figure 6.9 (b)), the order of magnitude of the electron density is 10^{18} cm^{-3} (equation (3.6)). This is a particularly high value, ~ 100 times higher than the density of vacuum arcs and 10 times higher than the density of sparks in gases. This first estimation is in good agreement with other studies on discharges in liquids (see section 2.2), and is also confirmed by the spectrum of figure 6.9 (c): this kind of line-merging phenomenon can only occur in extremely dense plasmas. The pressure imposed by the liquid surrounding the plasma is the cause of its high density.

With the two-line method applied to copper lines from time-integrated spectra, the electron temperature is estimated around $0.7 \text{ eV} \pm 0.15 \text{ eV}$ ($\sim 8100 \text{ K} \pm 1750 \text{ K}$). The errors in intensity measurements are principally due to other overlapping lines located near the copper lines. The value found is a low electron temperature, but consistent with previous studies on EDM plasmas [40, 41] and other similar plasmas [31, 34, 135]. It should be noted that this electron temperature estimation does not give information on the temperature at the electrode surfaces, which would be a useful value to know for simulations and practical applications. This temperature has to be measured differently. Results can be found in [123, 136].

The two-line method is based on the assumption of LTE. It is not an obvious assumption, especially for non-ideal plasmas such as EDM plasmas (see chapter 7), where coulombian interactions are comparable to thermal interactions. The evolution to the equilibrium state by thermal interactions is thus perturbed by coulombian effects. However, due to the high plasma density, one can assume that the numerous collisions between particles thermalize them rapidly.

A density criterion giving the validity of LTE can be derived theoretically [107, 137]. A plasma of temperature T is in complete LTE if its electron density n_e is higher than

$$n_e \geq 9.2 \cdot 10^{17} \cdot \sqrt{\frac{k_B T}{E_H}} \cdot \left(\frac{E_2 - E_1}{E_H} \right)^3 [\text{cm}^{-3}], \quad (6.1)$$

where E_H is the ionization energy of the hydrogen atom, E_1 the ground state energy of the atoms present in the plasma and E_2 the energy of their first excited state. According to this criterion, a hydrogen plasma at 0.7 eV is in LTE if

$$n_e \geq 8.6 \cdot 10^{16} \text{ cm}^{-3}. \quad (6.2)$$

If we assume that the EDM plasma is mainly composed by hydrogen, its electron density is sufficiently high for the assumption of LTE to be reasonably accepted. Therefore, even if we have not measured it separately, the ion temperature can be estimated to be of the same order as the electron temperature.

6.2 Time-resolved emission spectra

6.2.1 Merging of atomic lines

An example of time-resolved emission spectra taken during the first 5 microseconds of the discharge is given in figure 6.10.

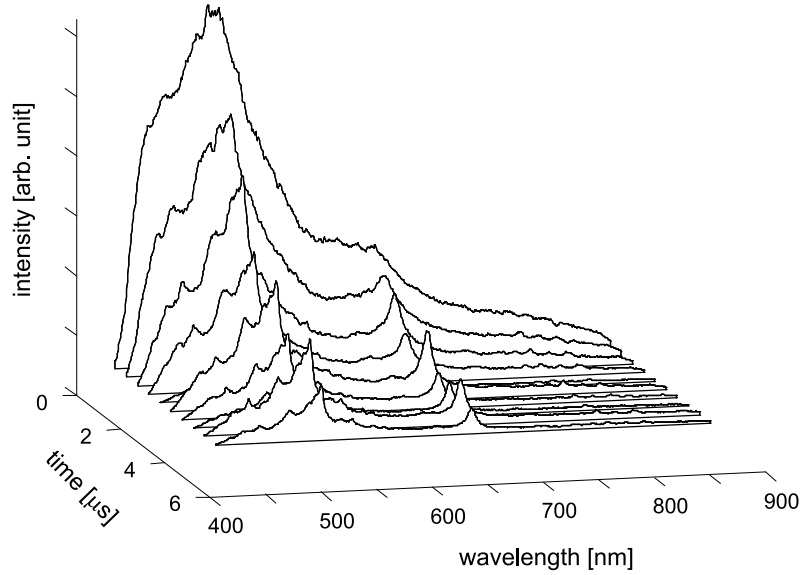


Figure 6.10: Example of time-resolved spectra (Cu/steel, 16 A, water; time resolution 500 ns, 150 g/mm grating).

The intensities of the spectra decrease with time, because the light emission is particularly intense during the first microsecond of the discharge, as stated previously in § 5.2.1. No lines are clearly identifiable in the very first spectrum. The emission is almost continuous. This effect of line merging has already been observed with very short discharges in the preceding section (figure 6.9). The previous conclusions about the high plasma density at the beginning of the discharge is thus confirmed by time-resolved measurements.

The merging can be more clearly seen in figure 6.11, which presents spectra of the first 3 microseconds of the discharge measured with a better time resolution than in figure 6.10. The spectral region investigated is centered around 520 nm, where the main Cu, Cr and Fe lines are located. All the lines are completely merged during approximately the first 400 ns. Their shapes then appear, strongly broadened between ~ 400 ns and $1 \mu\text{s}$, much less afterwards. This is evidence that the electron density is decreasing with time, as we will see later in § 6.2.3.

6.2.2 Evolution of the electron temperature

The evolution of T_e during the discharge is measured by applying the two-line method on each time-resolved spectrum. Note that it is impossible to measure T_e during the first microsecond of the discharge with this method, because of the line merging. The electron

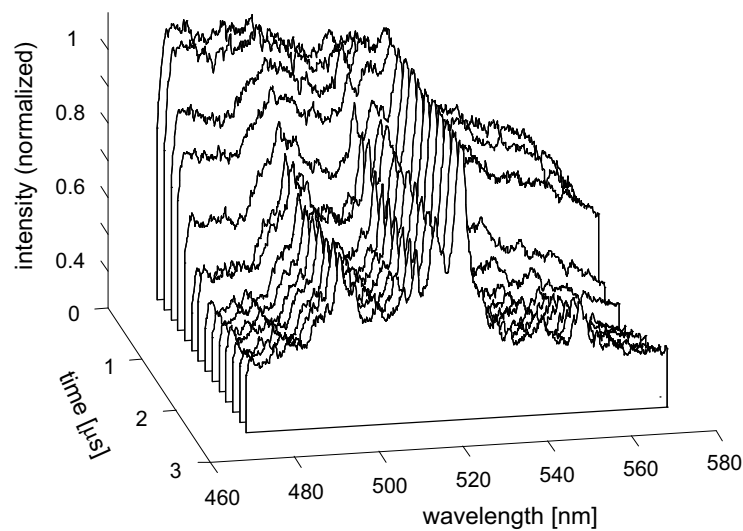


Figure 6.11: Merging of the Fe, Cu and Cr atomic lines (Cu/steel, 12 A, water; time resolution 200 ns, 600 g/mm grating). The spectra are normalized to the intensity of the Cu line at 521.8 nm.

temperature is slightly higher during the first 10 μs than for the rest of the discharge, being from ~ 0.8 to 0.7 eV ($\sim 9'000$ to $8'000$ K). Then it remains rather constant around 0.7 eV within the margin of error, even after 1 ms.

6.2.3 Evolution of the electron density

Figure 6.12 shows time-resolved emission spectra of the H_α line during the first 10 μs of the discharge.

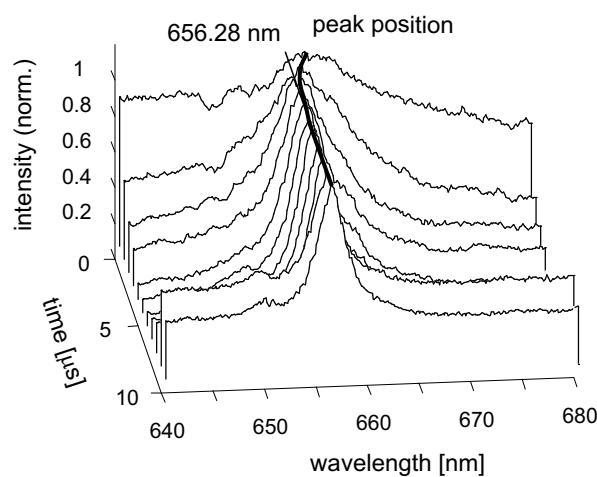


Figure 6.12: Broadening and shift of the H_α line (Cu/steel, 16 A, water; time resolution 1 μs , 600 g/mm grating). The spectra are normalized to the intensity of the H_α line.

The very first spectra show extremely broadened and shifted H_α lines. Thus, it is quite difficult to find a good fit for the first spectra, leading to non negligible errors in the FWHM measurements. The black lines on figure 6.12 represent the theoretical position of the H_α line (656.28 nm) and the measured peak positions. These lines are drawn to easily visualize the line shift. At the beginning of the discharge, we can measure FWHM up to 10 nm and shift up to 10 Å.

The evolution of n_e is calculated from these time-resolved H_α spectra with equations (3.6) and (3.7). Results are given in figure 6.13.

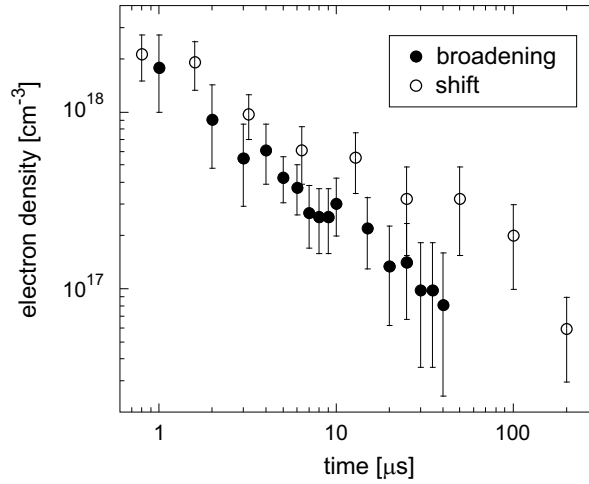


Figure 6.13: Evolution of the electron density, deduced from time-resolved broadening and shift measurements of the H_α line (Cu/steel, 16 A, water).

In spite of some differences, the FWHM and the shift measurements give comparable density values and evolution. As expected, the electron density is extremely high during the first microsecond (above 10^{18} cm^{-3}) and then decreases rapidly with time. The EDM plasma is created from a liquid, which is a dense medium ($\sim 3 \cdot 10^{22}$ water molecules/ cm^3 , for example). This is the main reason for the high plasma density. In the very beginning of the discharge, the plasma has to overcome the extreme pressure imposed by the dielectric. Then the plasma expands, which results in a decrease in its density. But during the whole discharge, the density remains high (always above 10^{16} cm^{-3}) due to the constant pressure of the surrounding liquid. The density reduction with time is confirmed by other studies on discharges in liquids [34].

The high electron density measured reinforces the assumption of free-bound and free-free radiation for the explanation of the continuum given in § 6.1.1. Since these two types of radiation processes involve free electrons, the intensity of free-bound and free-free radiation is in fact directly related to n_e . Therefore, the continuum is expected to be intense with such high values of n_e . Moreover, the measured continuum decreases with the discharge on-time (see figure 6.9), which is consistent with the decrease of n_e with time.

6.3 Spatially-resolved emission spectra

Figure 6.14 shows an example of spatially-resolved spectra along the vertical axis. The intensities of the spectra located in the center are higher, because the plasma is brighter in this region (see also figure 5.6).

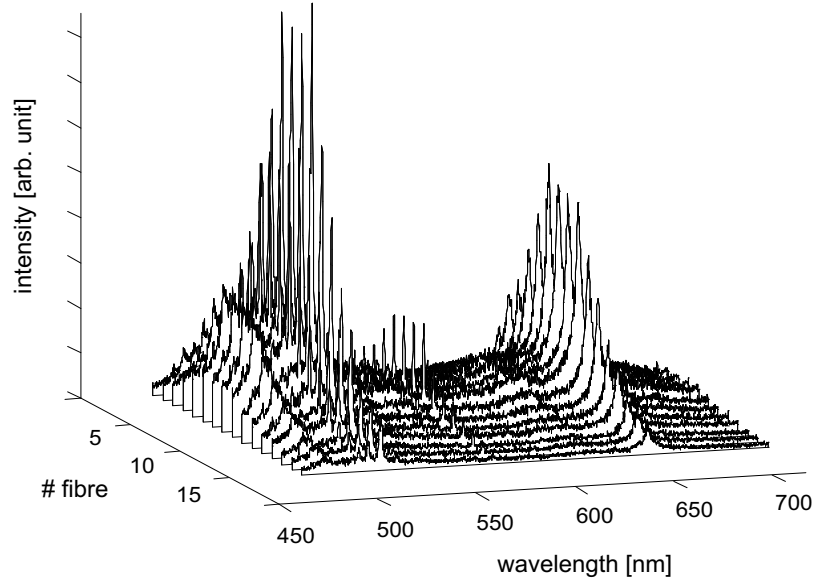


Figure 6.14: Example of spatially-resolved spectra, along the vertical axis (Cu/steel, 12 A, 4 μ s, water, 150 g/mm grating).

Note that the spatially-resolved axis is not calibrated in real distance, but simply graduated with the numbers of the fibres making the sampling. In order to make the conversion into real distance, we have to know the spatial resolution obtained with the fibre bundle, i.e. the real distance between two points seen by two consecutive fibres. This spatial resolution depends on the optical arrangement, mostly on the plasma–endoscope distance, which is not constant from one set of measurements to another. After each set of measurements (the simultaneous acquisition of the 16 spectra), the electrodes have to be changed due to their erosion, and the optical arrangement has to be re-aligned. Thus, an exact calibration for each set of measurements is time-consuming and has not been systematically done. The spatial resolution can nevertheless be estimated around 20–30 μ m/fibre (gap distance \sim 100 μ m), for all the measurements presented here.

6.3.1 Asymmetry of the contamination

As previously said, the spectral region around 520 nm is interesting for a qualitative characterization of the plasma contamination, because of the presence of three chromium lines at 520.45, 520.6 and 520.84 nm, and of the copper line at 521.82 nm. With a copper electrode and a stainless steel workpiece, the Cu line is emitted by particles coming from the electrode and the Cr lines are emitted by particles coming from the workpiece. Figure 6.15 shows spatially-resolved spectra along the vertical axis of this spectral region.

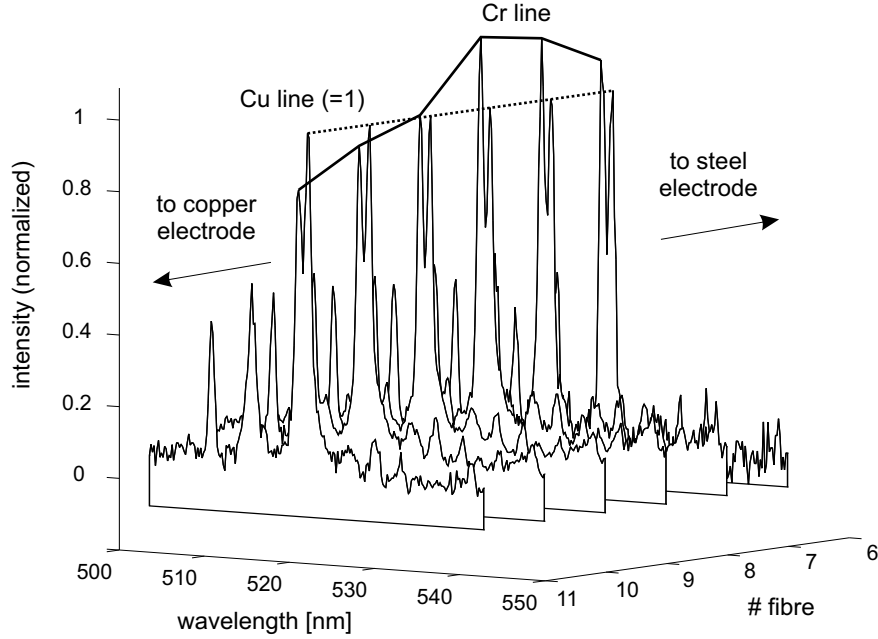


Figure 6.15: Vertical asymmetry of the plasma contamination (Cu/steel, 6 A, 100 μ s, water, 150 g/mm grating). The spectra are normalized to the intensity of the Cu line at 521.8 nm.

An asymmetry of the plasma contamination is clearly visible. Near the Cu electrode, the Cu line is more intense than the Cr lines. On the other hand, the Cr lines are more intense than the Cu line near the steel workpiece. Thus, even if Cu and Cr lines are present everywhere in the plasma, we see that each electrode is contaminating the plasma mostly in a region close to itself. Unsurprisingly, no asymmetry is visible along the horizontal axis (measurement not shown here).

Depending on the discharge parameters, material transfer from one electrode to the other can sometimes be observed. In this case, the intensity of lines emitted by both electrode materials are quite constant across the vertical profile. With the discharge conditions of figure 6.15, no material transfer is macroscopically visible on the electrodes after several minutes of machining. This is qualitatively confirmed by the contamination asymmetry measured by spatially-resolved spectroscopy.

6.3.2 Electron temperature profile

Spatially-resolved spectra of the three Cu lines used for T_e calculations are shown in figure 6.16, along with the electron temperature vertical profile calculated from them. The central spectra have a better signal to noise ratio than the outer ones, because the light intensity is higher in the center. The electron temperature is quite constant over the whole profile. Measurements along the horizontal axis are not shown here but do not show any difference. The plasma has thus a homogeneous electron temperature around 0.7 eV, as previously measured.

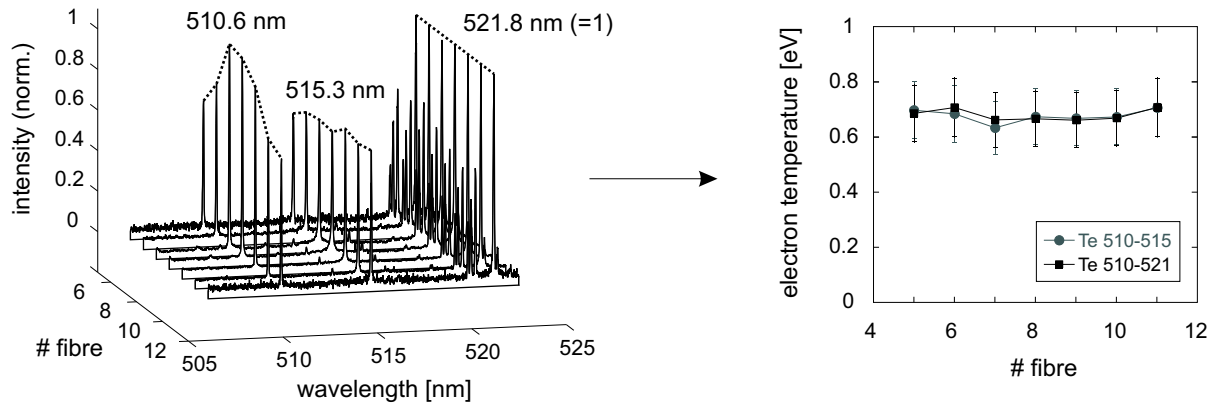


Figure 6.16: Vertical profile of the electron temperature calculated from spatially-resolved Cu lines intensities ratios (Cu/steel, 6 A, 100 μ s, water, 1800 g/mm grating). The spectra are normalized to the intensity of the Cu line at 521.8 nm.

6.3.3 Electron density profile

Spatially-resolved H_α spectra, along with the electron density vertical profile calculated from them with equation (3.6), are shown in figure 6.17. The values found are in good agreement with our previous results (figure 6.13), around $5 \cdot 10^{16} \text{ cm}^{-3}$ for a 100 μ s discharge. Despite large error bars, the electron density seems to be slightly higher in the plasma center. The horizontal profile, not shown here, is very similar to the vertical one.

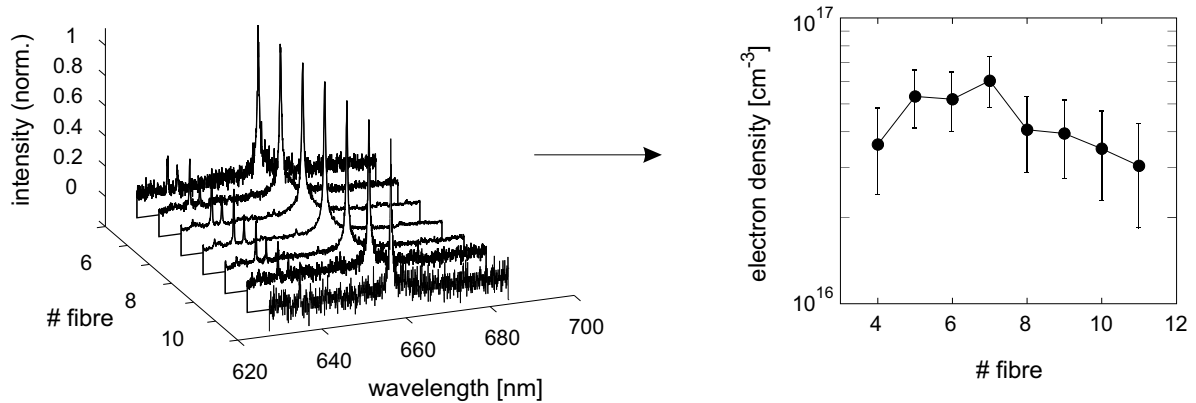


Figure 6.17: Vertical profile of the electron density calculated from spatially-resolved H_α broadening measurements (Cu/steel, 6 A, 100 μ s, water, 600 g/mm grating). The spectra are normalized to the intensity of the H_α line.

6.4 Time- and spatially-resolved emission spectra

6.4.1 Evolution of the contamination

A temporal and spatial characterization of the contamination can be obtained by gating the camera when acquiring spatially-resolved spectra of the Cr and Cu lines. In order to present the contamination results in a convenient way, we have calculated, for each spectrum, the lines intensities ratio R defined by

$$R \doteq \frac{I(\text{Cr})}{I(\text{Cu})} = \frac{I(520.5 \text{ nm}) + I(520.6 \text{ nm}) + I(520.8 \text{ nm})}{I(510.6 \text{ nm}) + I(515.3 \text{ nm}) + I(521.8 \text{ nm})}.$$

This value represents the relative importance of the contamination coming from the workpiece (Cr lines) with respect to the contamination coming from the electrode (Cu lines). The *absolute* value of R has no physical significance and is not important, but its evolution in space and time is of interest for a description of the contamination. Figure 6.18 shows an example of a spectrum where these lines are located, along with the evolution of R profiles. The delay between the beginning of the discharge and the camera exposure is indicated near each profile.

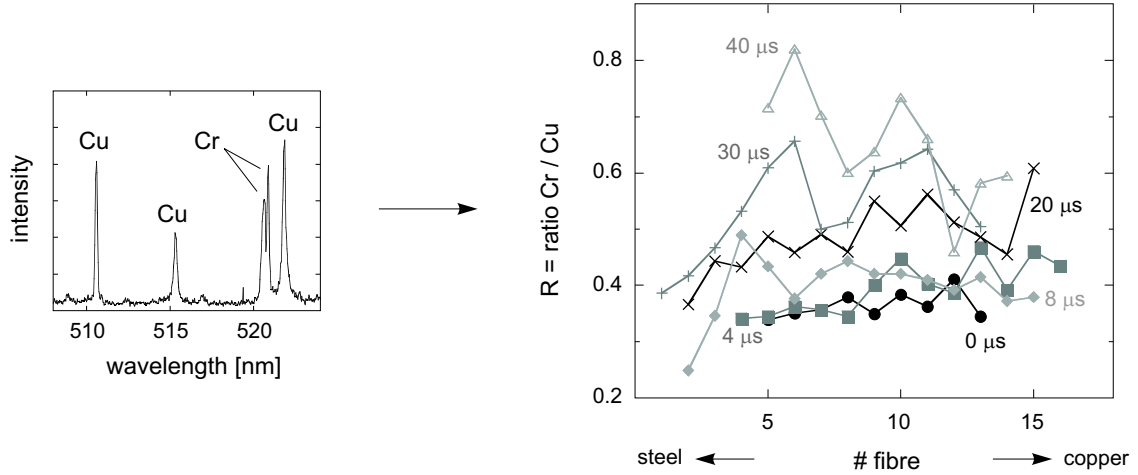


Figure 6.18: Evolution of the contamination distribution, deduced from time- and spatially-resolved spectra of Cu and Cr lines (Cu/steel, 12 A, 50 μs , water; time resolution 2 μs).

The ratio R clearly increases during the discharge, from ~ 0.35 to 0.7 in 40 μs . It indicates that the plasma contamination from the workpiece material increases with time, probably by direct vaporization of the metal into the plasma. This vaporization is mostly efficient after $\sim 10 \mu\text{s}$ (R is roughly constant before). Again, it is impossible to quantify the efficiency of the vaporization, in terms of material removal rate. But even if some amount of material is vaporized during the discharge, the largest part of the erosion occurs certainly at the end of the discharge, with the implosion of the plasma.

The increase in R with time could also be partially due to a small decrease of the contamination from the electrode during the discharge. It is known indeed that wear mostly occurs at the beginning of the discharge.

Due to the asymmetry of the contamination observed in the preceding section, the profiles of R should be decreasing from the left to the right. The steel workpiece is indeed located towards the left (towards fibre #1) and the copper electrode towards the right (towards fibre #16). This tendency cannot be observed in figure 6.18. It is mainly due to the large experimental errors (error bars are not shown for clarity). As stated in section 3.6, time- and spatially-resolved measurements are particularly difficult. Contrary to the increase in R with time, the asymmetry is probably an effect too subtle to be detected during these measurements.

The effect of the electrode polarity on the contamination distribution and evolution is shown in figure 6.19.

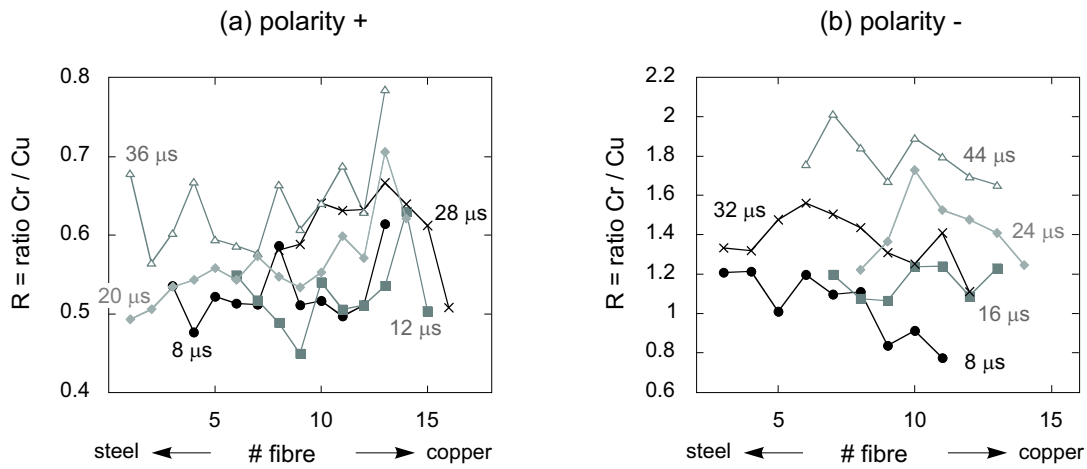


Figure 6.19: Effect of the electrode polarity on the evolution of the contamination repartition, deduced from time- and spatially-resolved spectra of Cu and Cr lines (Cu/steel, 6 A, 50 μs , water; time resolution 4 μs): (a) positive polarity; (b) negative polarity.

As in figure 6.7, the situation where the wear is important (figure 6.19 (a)) can be distinguished from the situation where the erosion is important (figure 6.19 (b)). The ratio R is in fact lower with the positive polarity (0.5–0.7) than with the negative polarity (0.8–2). R increases with time, for both polarities: it slightly increases from 0.5 to 0.65 in (a), but doubles from 0.9 to 1.8 in (b). The vaporization is thus more efficient in the latter case. Again, it is difficult to observe the contamination asymmetry. Some of the profiles in figure 6.19 (b) nevertheless slightly decrease from left to right.

6.4.2 Evolution of the electron temperature profiles

Spatially-resolved spectra of the Cu lines taken at three different times of the discharge are given in figure 6.20. The decrease in the continuum intensity and in the line broadening with time can be observed. It is remarkable that even the Cu lines show a significant broadening during several microseconds, due to the high plasma density. These lines are in fact much less sensitive to Stark broadening than hydrogen lines. Broadening of Cu lines is also observed in laser-produced plasmas with copper targets [94, 138].

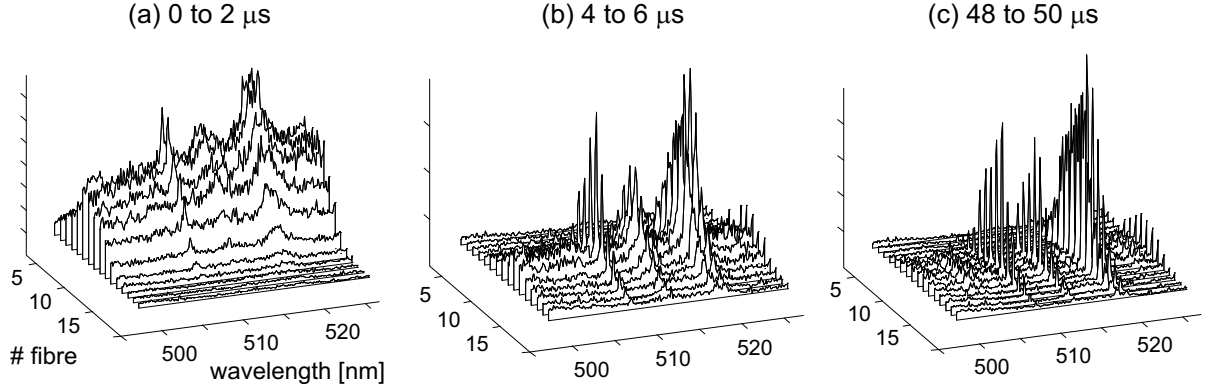


Figure 6.20: Time- and spatially-resolved spectra of the Cu lines used for electron temperature calculation (Cu/steel, 12 A, 50 μ s, water; time resolution 2 μ s, 600 g/mm grating): (a) 0 to 2 μ s; (b) 4 to 6 μ s; (c) 48 to 50 μ s.

Figure 6.21 shows the evolution of T_e profiles calculated from the previous spectra. As previously mentioned, the electron temperature is slightly higher at the beginning, but remains around 0.7 eV. The profiles are roughly flat within the margin of errors.

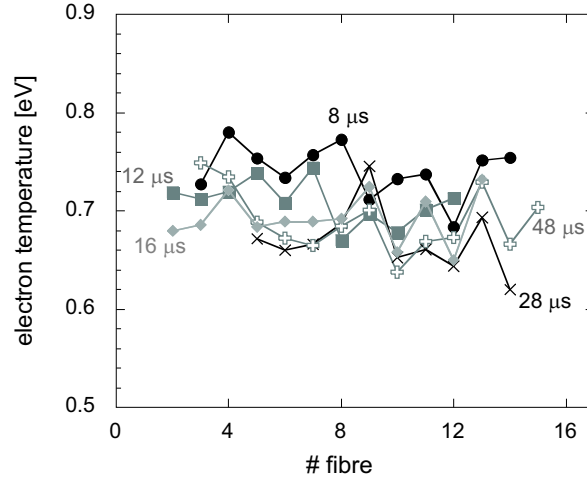


Figure 6.21: Evolution of the electron temperature profiles (Cu/steel, 12 A, 50 μ s, water, time resolution 2 μ s).

6.4.3 Evolution of the electron density profiles

Time- and spatially-resolved H_α spectra are shown in figure 6.22. The spectra are quite noisy, due to the weak intensity emitted. Nevertheless, the H_α broadening is easily observable.

The evolution of the electron density profiles is presented in figure 6.23. These density measurements are consistent with time-resolved and spatially-resolved measurements

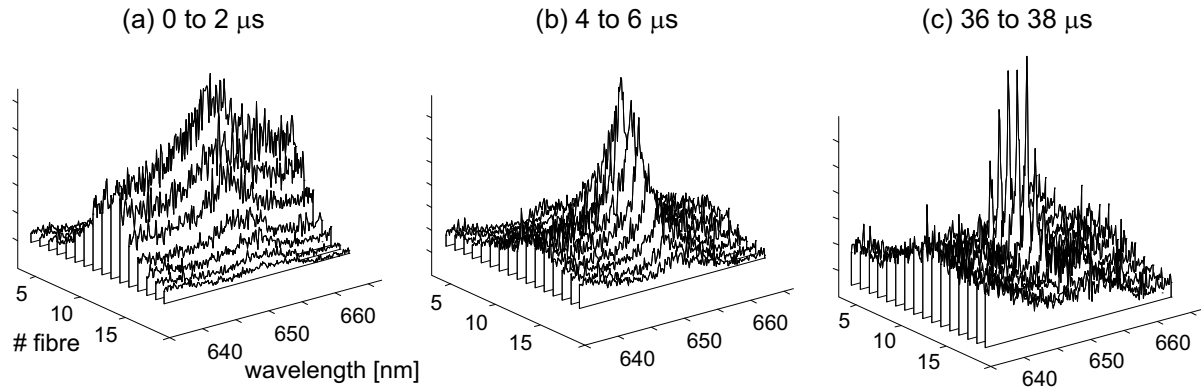


Figure 6.22: Time- and spatially-resolved spectra of the H_α line (Cu/steel, 12 A, 50 μ s, water; time resolution 2 μ s, 600 g/mm grating): (a) 0 to 2 μ s; (b) 4 to 6 μ s; (c) 36 to 38 μ s.

previously presented (figures 6.13 and 6.17). The density diminishes during the discharge, by almost two orders of magnitude in 50 μ s. The density is slightly higher in the plasma center, and this tendency is verified during the whole discharge. This temporal and spatial characterization of n_e can be useful for the validation of EDM plasma simulations.

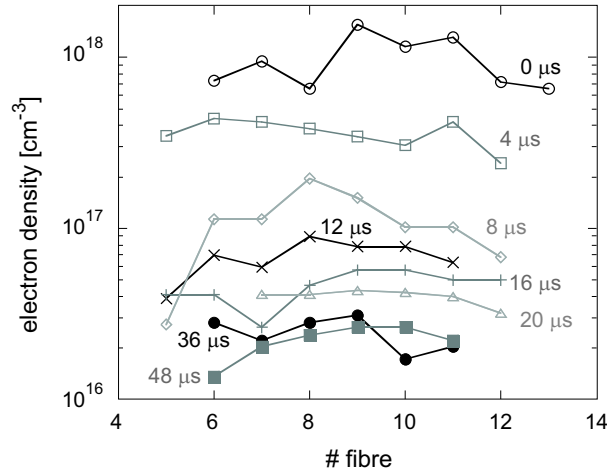


Figure 6.23: Evolution of the electron density profiles (Cu/steel, 12 A, 50 μ s, water, time resolution 2 μ s).

Chapter 7

Non-ideality of EDM plasmas

In this chapter, we will show that EDM plasmas are weakly non-ideal. The definition of a non-ideal plasma is given in the first section. Spectroscopic evidence of the non-ideality of EDM plasmas is discussed in the second section. Finally, the third section presents a general summary of the EDM plasma physical properties, measured in this work.

7.1 Plasma coupling parameter Γ

Natural plasmas and artificially-produced plasmas are both very diverse. Generally, they are classified according to their temperature and density, because the properties of a plasma depend mostly on these two parameters.

In particular, the density n and temperature T define whether a plasma is *ideal* or not. In an ideal plasma, the particles are almost free, i.e. their movement is only weakly influenced by other particles. In this case, the mean kinetic energy of particles is much higher than the mean Coulomb potential energy between them.

Knowing n and T for a given plasma, we can calculate its coupling parameter Γ , which quantifies its “degree of ideality”. This parameter represents the ratio of the potential energy of Coulomb interaction at the mean inter-particle distance divided by the mean thermal energy of the charged particles in the plasma. It is defined by

$$\Gamma \doteq \frac{Z^2 e^2}{4\pi\epsilon_0 a k_B T} , \quad (7.1)$$

where Z is the charge of the particles ($Z=1$ for hydrogen ions, for example), e the elementary charge, ϵ_0 the vacuum permittivity, and a the mean inter-particle distance given by

$$a = \left(\frac{3}{4\pi n} \right)^{1/3} . \quad (7.2)$$

Therefore, we see that

$$\Gamma \propto \frac{n^{1/3}}{T} . \quad (7.3)$$

The plasma is called:

- *ideal* if $\Gamma \ll 1$;
- *weakly non-ideal* if $\Gamma \leq 1$;
- *strongly coupled* if $\Gamma > 1$.

According to equation (7.3), we see that ideal plasmas are characterized by a low density and a high temperature. Note that Γ is linked with the Debye length λ_D , defined by

$$\lambda_D \doteq \sqrt{\frac{\varepsilon_0 k_B T}{e^2 n}}, \quad (7.4)$$

by the relation

$$\Gamma^{3/2} \propto \frac{1}{n \lambda_D^3}.$$

Therefore, we see also that, in an ideal plasma, a very large number of particles is contained in a Debye sphere. Nevertheless, the higher the number of particles in a Debye sphere, the less the particles interact with each other.

On the other hand, non-ideal and strongly coupled plasmas are **dense** and/or **cold**. In such plasmas, the inter-particle distance is short enough, and the particle velocity small enough, to produce significant electrostatic interactions between the charged particles. For a given particle, the microfields created by the others have a significant influence on it.

We have seen in the previous chapter that EDM plasmas have a typical electron temperature of 0.7 eV and a typical electron density of 10^{18} cm^{-3} . Thus, the typical coupling parameter of EDM plasmas is around

$$\Gamma \simeq \mathbf{0.33}.$$

If we consider that n_e reaches $2.5 \cdot 10^{18} \text{ cm}^{-3}$ in the very beginning of the discharge (see figure 6.13), $\Gamma \simeq \mathbf{0.45}$ during the first microsecond. Thus, EDM discharges produce cold and dense plasmas which are **weakly non-ideal**.

According to equation (7.4), the typical Debye length of EDM plasmas is around 6 nm. The mean inter-particle distance a is also around 6 nm (equation (7.2)). Thus, a Debye sphere is containing roughly only one particle. This is another illustration of the plasma non-ideality.

Figure 7.1 shows the classification of the main types of natural and artificial plasmas, including EDM plasmas, in a log density–log temperature diagram. Ideal, weakly non-ideal and strongly coupled plasmas can easily be distinguished in such a log-log diagram, because Γ iso-contours are straight lines.

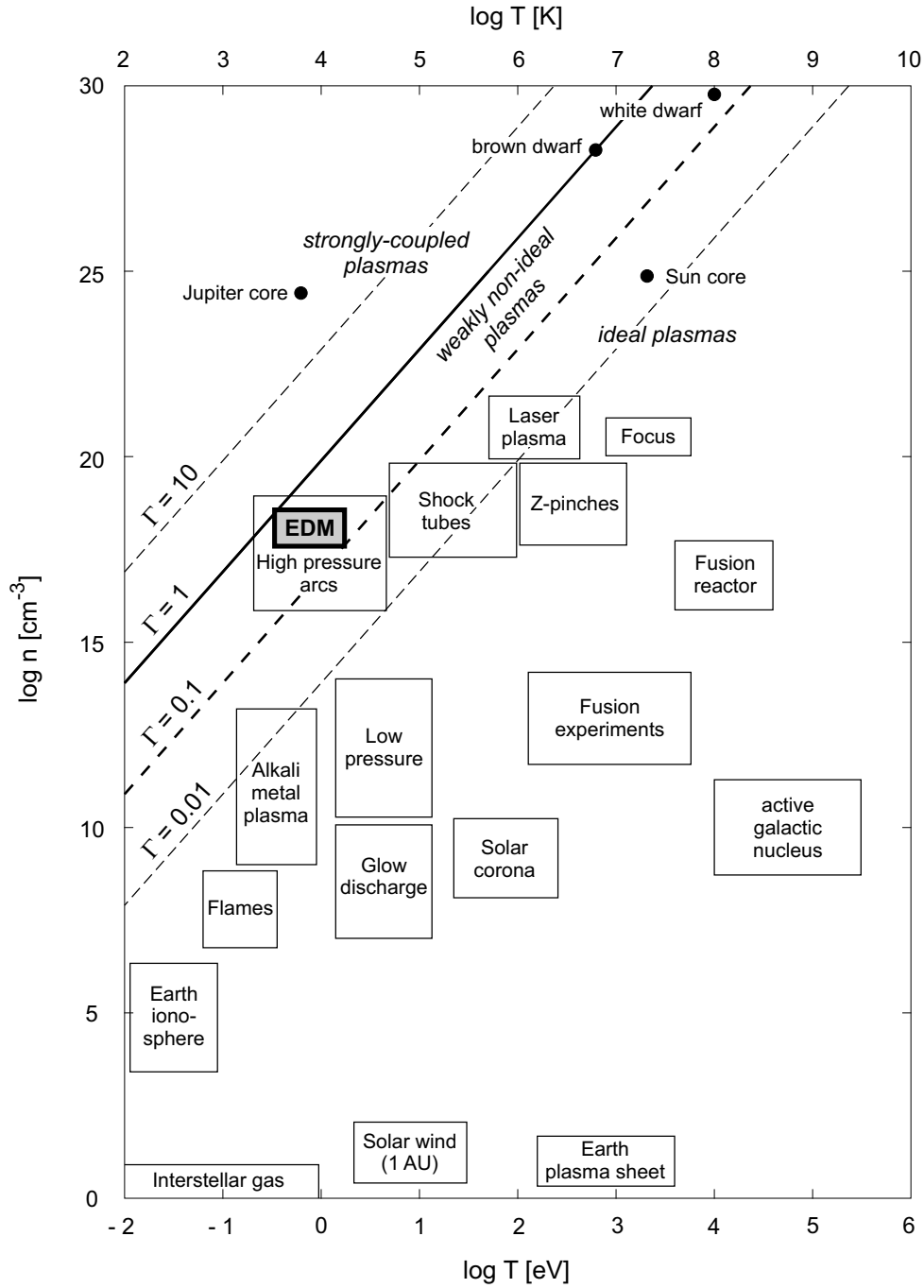


Figure 7.1: Classification of plasmas according to their density and temperature (adapted from [45, 139]).

One can see in figure 7.1 that the majority of natural and artificial plasmas are ideal. Besides extremely dense astrophysical objects, few non-ideal plasmas exist. From the physical point of view, their extreme properties make them particularly interesting to study. The physics of non-ideal plasmas is complex, differing from “classical” plasma

physics theories [43–46]. Corrections have to be made because of deviations from the binary collision model due to collective effects. For example, the screening mechanism described by the Debye model has to be modified in non-ideal plasmas. Theories have been developed quite recently, mainly due to the lack of experimental data before the 1980’s. The creation of dense, and therefore non-ideal plasmas, is in fact difficult and requires considerable experimental resources (see § 2.3). In this context, EDM discharges appear to be a very simple method to produce such plasmas. EDM plasmas are indeed amongst the most dense artificially-created plasmas. But unfortunately, these plasmas are not the easiest to be investigated experimentally, as repeated several times in this work.

7.2 Spectroscopic signs of the non-ideality

In addition, spectroscopic results indicate also that the EDM plasma is non-ideal.

7.2.1 Broadening and shift of H_α

Since non-ideal plasmas are dense, a strong Stark broadening and shift of spectral lines is naturally a characteristic sign of non-ideality. The microfields deform the energy spectrum of radiating atomic particles, i.e. they perturb the initial and final states of radiative transitions. The atomic levels are shifted and split, and this results in line broadening and shift [43, 44].

This effect can be clearly observed on optical spectra emitted by EDM plasmas, especially on the H_α line. This fact has already been discussed in detail in chapter 6. Similar strong broadening and shift of hydrogen lines in dense plasmas have been reported in numerous works [113, 115, 117, 135, 140–144].

It should be noted that the calculation of spectral line shapes emitted by dense plasmas has been recently much improved. Simulations in good agreement with experimental data are obtained with models including several non-ideal effects, such as the effect of the dynamic microfield created by the ions or the influence of electron collisions [45]. Calculations are mostly done for lines of the hydrogen atom or hydrogen-like ions, because of the “simplicity” of quantum calculations for these species.

7.2.2 Asymmetry and structure of H_α

Besides its broadening and shift, the H_α line gives other useful information. Figure 7.2 shows a typical example of a high resolution spectrum of the H_α line. If a lorentzian fit is applied, it is observed that the shape of the line is slightly asymmetric and deviates from the fit. This asymmetry is also due to interactions between ions and the emitter (hydrogen atom in our case), and is another sign of plasma non-ideality [43, 114, 116].

We also see in figure 7.2 the complex structures around the H_α line. The arrows mark small bumps which are not due to radiation of other lines. These structures are created by several phenomena, which occur in dense plasmas [145–153]. Figure 7.3 gives a simple explanation for the origin of these structures.

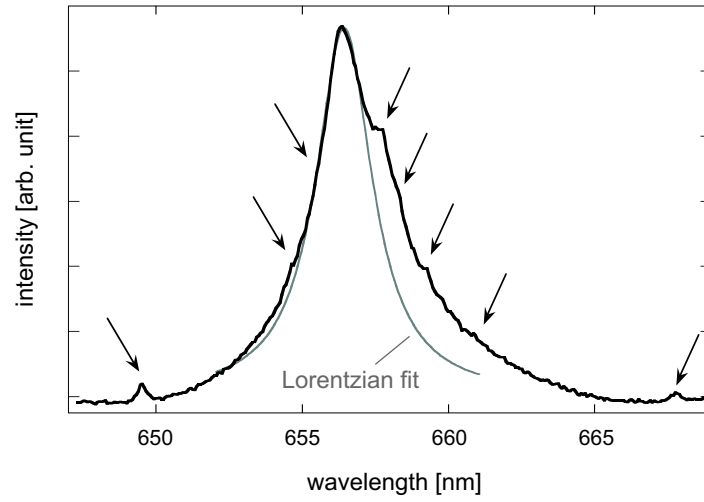


Figure 7.2: Complex structure of the H_α line (C/steel, 24 Å, 12 μ s, oil, 1200 g/mm grating).

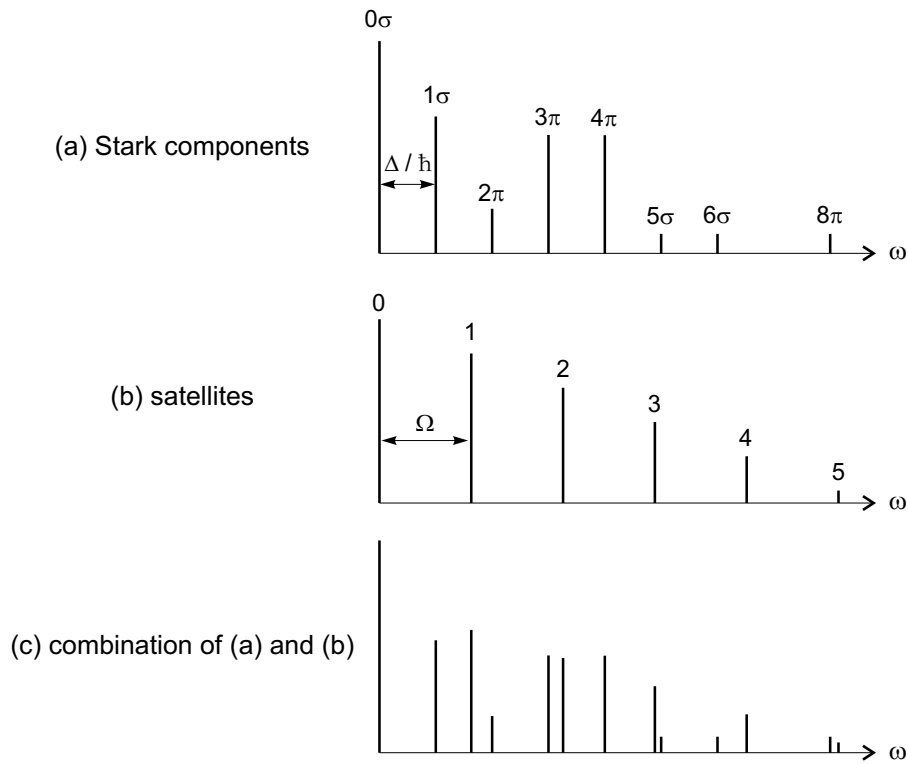


Figure 7.3: Theoretical structure of the H_α line in a non-ideal plasma [147]: (a) Stark components of H_α (see appendix A.2); (b) satellite lines due to plasma waves or turbulence; (c) resulting H_α structure. The frequency $\omega = 0$ corresponds to the H_α unperturbed position ($\lambda_0 = 656.28$ nm). The components on the other side of the line are symmetrically positioned.

First, the quasistatic ion microfields cause splitting of energy levels in hydrogen atoms by the Stark effect. The H_α emission is formed by several lines, due to transitions be-

tween these new levels (see appendix A for more details). These lines are represented in figure 7.3 (a), where σ and π denote the polarization of each component. Moreover, low frequency electrostatic waves can also produce a substantial quasistatic field, with the same effect as the ion microfield.

Furthermore, if plasma waves or turbulence are present in the plasma, a high frequency electric field is superimposed on the quasistatic microfield. This dynamic field, oscillating with a frequency Ω , produces satellite lines as shown in figure 7.3 (b). In the case of Langmuir waves for example, the frequency of the dynamic field is

$$\Omega \simeq \omega_{pe} ,$$

where ω_{pe} is the electron plasma frequency defined by

$$\omega_{pe} \doteq \sqrt{\frac{e^2 n_e}{\varepsilon_0 m_e}} . \quad (7.5)$$

For EDM plasmas, $\omega_{pe} \simeq 5 \cdot 10^{13} \text{ s}^{-1}$. The field associated with Langmuir waves will create satellite lines located at

$$\lambda_k = \lambda_0 \pm k \cdot \lambda_{pe} , \quad k = 1, 2, 3, \dots$$

where λ_0 is the unperturbed H_α position, and where

$$\lambda_{pe} = \frac{\omega_{pe}}{2\pi c} \cdot \lambda_0^2$$

is the wavelength associated with the electron plasma frequency [148, 153].

The combination of the quasistatic and the oscillating field produces a spectrum where the Stark components and the satellites are superimposed, as shown in figure 7.3 (c). Furthermore, if the frequency between the Stark components matches the frequency of the dynamic field (i.e. if $\Delta/\hbar = \Omega$), resonant interactions occur. As a consequence, depressions or “dips” will appear on the spectrum.

The addition of all these effects, typical in non-ideal plasmas, results in multiple modifications to the H_α profile, as seen in figure 7.2. The complexity of the emission spectrum reflects the complexity of the plasma itself: it is a cold and dense plasma, highly collisional, with strong electric fields, turbulence and resonance phenomena.

In principle, the position of the structures in figure 7.2 should allow us to estimate the value of the electric fields present in the plasma. But this estimation can be done only if the structures are completely identified, which is extremely complex. The Stark components have to be distinguished from the satellites, which can be produced by different simultaneous waves or turbulence.

In our case, this identification is not possible. First, the structures of figure 7.2 are barely observable, and it is also almost impossible to estimate which waves are present in the EDM plasma. Turbulent phenomena are certainly more likely than “classical” plasma waves. Nevertheless, the ion microfield can be estimated from the mean inter-particle distance [111, 149]. With a density of 10^{18} cm^{-3} , the microfield is around 10^6 V/cm .

7.2.3 Absence of H_β and line merging

Another important effect of the plasma non-ideality is the transformation of the upper members of a spectral series into a continuous spectrum [43, 44, 134]. This effect is due to:

1. the lowering of the ionization threshold;
2. the merging of spectral lines near the series limit.

First, the ionization potential of atoms is lowered in non-ideal plasmas. Inter-particle interactions in high density plasmas “destroy” in fact the upper atomic levels. More precisely, the microfields which are superimposed on the Coulomb electric field of an atomic nucleus, transform the upper energy states of this atom into unbound states, as shown in figure 7.4.

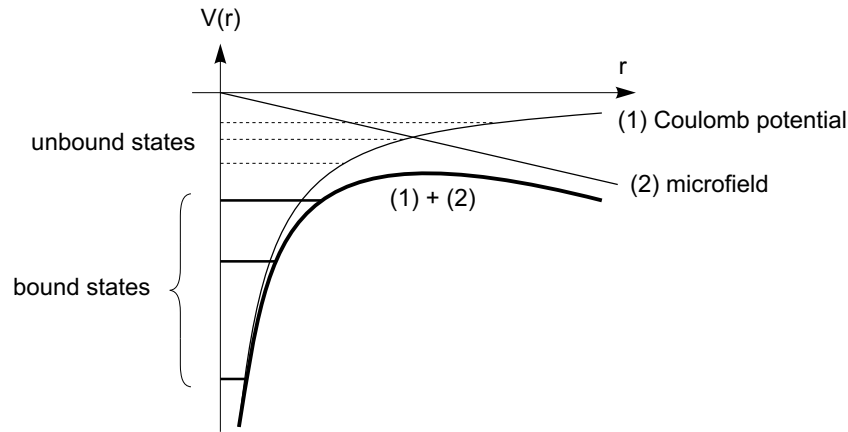


Figure 7.4: Lowering of the ionization threshold in non-ideal plasmas, due to the effect of microfields (assumed to be uniform on the atomic scale) [44].

The shift in the ionization energy ΔU_i is given by

$$\Delta U_i = \frac{Z^2 e^2}{4\pi\epsilon_0 \lambda_D}, \quad (7.6)$$

where λ_D is the Debye length [44, 46]. In our case, we found $\Delta U_i \simeq 0.23$ eV. This lowering of the ionization threshold modifies the optical spectrum of the plasma. Figure 7.5 explains schematically the consequences in the case of an hydrogen plasma.

In an unperturbed atom, all the levels can be populated by electrons (figure 7.5 (a)). Therefore, the different lines of all series can be emitted, in particular those of the Balmer series: H_α , H_β , H_γ , etc. Continuous radiation by free-bound transitions is emitted by electrons coming from the energy continuum, whose threshold is 13.6 eV above the ground state $n = 1$ (see figure 3.8).

On the other hand, in a dense plasma, the ionization potential is lowered due to the microfields. If the “new” threshold is located between levels $n = 3$ and $n = 4$ for example

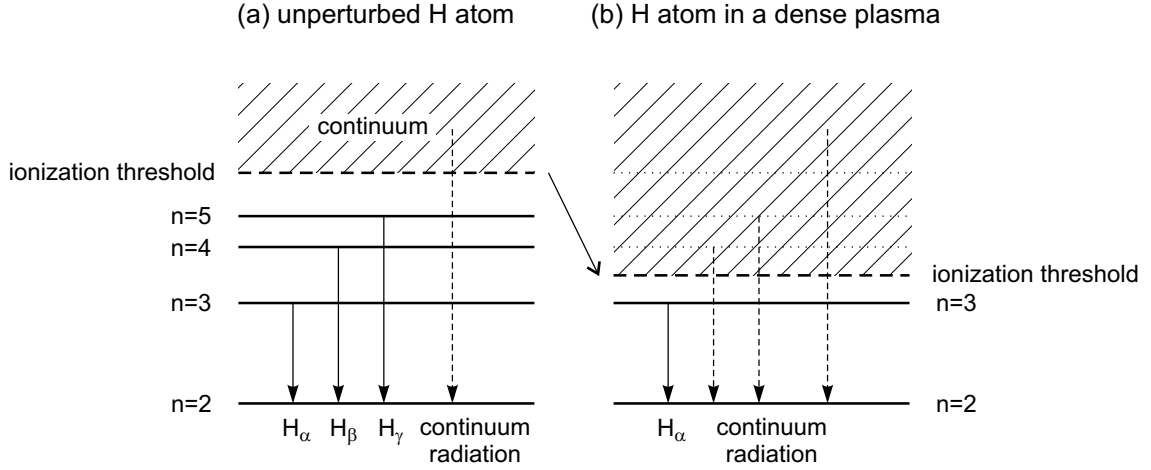


Figure 7.5: Absence of H_β and increase in the continuum radiation due to the lowering of the ionization threshold in a dense hydrogen plasma.

(figure 7.5 (b)), the only Balmer line which can still be emitted is the H_α line, because the upper levels of all other Balmer lines are now in the energy continuum. In addition to the disappearance of these lines, another consequence of the lowering of the ionization threshold is an increase in the continuum radiation. Free-bound and free-free transitions become much more likely with a lowered threshold.

Secondly, some of the remaining spectral lines, whose upper states are yet *below* the “new” ionization threshold, can still be “erased”. Although these lines are discrete transitions, they appear as a continuum radiation not because their upper state is in the energy continuum, but because of the Stark broadening. The upper lines of a series are close to each other in the spectrum. If they are significantly broadened so that their widths exceed the distance between them, they will overlap with adjacent lines and merge into a continuum. The continuum formed by this degeneracy of lines is the type of continuum observed during the first microsecond of the EDM discharge (see § 6.1.6 and § 6.2.1). The Stark broadening of lines near the series limit has thus the same effect as the lowering of the ionization threshold: it transforms the upper members of a spectral series into a continuous spectrum. Therefore, this second effect can be considered as an *apparent* or *optical* lowering of the ionization threshold [43, 44].

As showed in chapter 6, the spectra of EDM plasmas are characterized by the absence of the H_β line and other upper Balmer lines, by a strong continuum radiation and by merging of almost all lines at the beginning of the discharge. All these characteristics can thus be viewed as signs of the non-ideality of the EDM plasma.

7.2.4 Inglis-Teller relation

As previously said, upper spectral lines of a series can be merged if the plasma is dense, due to their overlapping caused by Stark broadening. Since the number of these “erased”

lines depends on the plasma density, the last discernible line gives a rough estimation of the density. For hydrogen Balmer lines, this estimation is given by the *Inglis-Teller relation*:

$$\log n = 23.26 - 7.5 \cdot \log n_{\max} , \quad (7.7)$$

where n is the density expressed in cm^{-3} and n_{\max} the quantum number of the upper energy level of the last visible transition [43, 108, 154–156]. This relation is mainly used in astrophysics, to evaluate the electron density in the atmosphere of stars, for example. The coefficients of this relation are sometimes slightly different in literature. The uncertainty factor of this relation is about 50% [108].

If we observe on EDM spectra the H_α line (transition from level 3 to 2) but no H_β line (transition from level 4 to 2), then

$$3 \leq n_{\max} < 4 ,$$

and the plasma density is at least $6 \cdot 10^{18} \text{ cm}^{-3}$ according to relation (7.7). This rough estimation is of the same order of magnitude as our previous density measurements and confirms their validity.

Contrary to upper hydrogen Balmer lines which disappear because of their strong broadening, metallic lines do not merge and can be observed in the EDM plasma spectrum, as shown in chapter 6. The metallic lines are much less sensitive to Stark broadening, and this explains why they are still observable. The Stark broadening of non-hydrogenic lines is rather poorly documented, and few data are available [157]. Nevertheless, the FWHM of a few atomic copper lines can be found. For example, in a plasma with an electron density of 10^{17} cm^{-3} and at 10'000 K, the FWHM of the H_α line is 10.8 Å, whereas the FWHM of the Cu lines at 510.6, 515.3 and 521.8 nm are 0.43, 1.9 and 2.2 Å respectively [158]. This shows that non-hydrogenic lines are not sufficiently broadened to merge and disappear into a continuum, as upper hydrogen lines do.

7.3 Summary of the physical properties of EDM plasmas

According to the measurements presented in this work, EDM plasmas have the following characteristics:

- The plasma is composed of species coming from the cracking of the dielectric molecules, mainly **hydrogen**, with **contamination** from the electrode materials. The contamination is slightly higher in the vicinity of the electrodes, and increases during the discharge.
- The **electron temperature** T_e is low, around 0.7 eV (8'100 K), slightly higher at the beginning of the discharge. The temperature is homogeneous in the plasma. The

assumption of LTE can be accepted due to the high plasma density, and therefore the ion temperature T_i should be similar to the electron temperature.

- The **electron density** n_e is extremely high, reaching $2 \cdot 10^{18} \text{ cm}^{-3}$ during the first microsecond of the discharge, decreasing rapidly afterwards. The density is slightly higher in the plasma center. The ion density n_i should be roughly equal to the electron density, since multiple ions are unlikely with such a low electron temperature and since quasineutrality should hold.
- The plasma is very dense and cold, and therefore presents several **non-ideal effects**, especially in the beginning of the discharge. The coupling parameter Γ is around 0.33, and reaches 0.45 during the first microsecond.
- The **Debye length** λ_D is around 6 nm, and the mean **inter-particle distance** a is also around 6 nm. Therefore, a Debye sphere contains roughly only one particle. Again, this is a sign of the plasma non-ideality.
- The **light** emitted by the plasma is much more intense during the first microsecond than during the rest of the discharge.
- Due to its high density, the EDM plasma could be not completely optically thin. The **opacity** of a plasma increases in fact with the density. For example, ultra-dense plasmas produced by exploding wires in water ($n_e = 2 \cdot 10^{21} \text{ cm}^{-3}$) are known to be highly opaque and to radiate like a blackbody [33]. Consequently, the light emitted by the very center of the EDM plasma at the beginning of the discharge could be absorbed within the plasma and not be measured. The opacity can be a problem for spectroscopic diagnostics, since the core of an opaque plasma cannot be characterized with such diagnostics. Nevertheless, in our case, the plasma opacity could be critical only during roughly the first 500 ns of the discharge, when the density reaches its maximum. But during this period, T_e and n_e can anyway not be measured with the spectroscopic methods used in this work, because of the line merging.
- **Energy** is dissipated in the plasma by Joule heating, heat conduction, radiation and mechanical work (plasma expansion). Energy is also used for evaporation, dissociation, ionization and excitation of the dielectric molecules and atoms. The energy received by the workpiece is mainly brought by ion bombardment. Thermal run-away of the very superficial layers is also probable in the beginning of the discharge, due to the massive flow of energy at the breakdown.
- For a plasma in LTE, the repartition of the densities of the different species is described by the *Saha equation*. For a plasma containing electrons, one type of singly charged ions and one type of atoms, the Saha equation is

$$\frac{n_e n_i}{n_a} = \frac{Z_e Z_i}{Z_a} \cdot \left(\frac{2\pi m_e k_B T}{h^2} \right)^{3/2} \cdot \exp \left(-\frac{U_i - \Delta U_i}{k_B T} \right), \quad (7.8)$$

where n_k is the density of the species k , Z_k its partition function, U_i the ionization energy of the atom, and ΔU_i its correction due to non-ideality (equation (7.6)) [44,159]. In principle, this equation can be used for the calculation of the EDM plasma **ionization degree** n_e/n_a . For a hydrogen plasma, $Z_e = 2$, $Z_i = 1$ and

$$Z_a = \sum_{n=1}^{n_{\max}} g_n \exp\left(-\frac{E_n}{k_B T}\right) = \sum_{n=1}^{n_{\max}} 2n^2 \exp\left(-\frac{U_i(1-1/n^2)}{k_B T}\right),$$

where $U_i = 13.6$ eV and $n_{\max}^2 = U_i/\Delta U_i$. In our case, we found $Z_a \simeq 2$. Assuming in addition $n_e = n_i = 10^{18} \text{ cm}^{-3}$, we found $n_e/n_a = 10^{-5}$.

The ionization degree of the EDM plasma is certainly much higher, probably about 0.1 as for similar discharges [34]. High-pressure arcs have also similar densities as EDM plasmas, and are known to be strongly ionized. The calculation gives $n_e/n_a = 10^{-5}$, then we found $n_a = 10^{23} \text{ cm}^{-3}$ if we assume that $n_e = 10^{18} \text{ cm}^{-3}$. Such a high density of atoms is unlikely, since the density of molecules in the liquid is around 10^{22} cm^{-3} . This shows that the ionization degree calculated here is not correct. The assumptions made are probably too strong. In particular, the Saha equation as written in (7.8) does not take into account the complex composition of the EDM plasma. But for a multi-component plasma, the Saha equation has no analytical solution and becomes difficult to solve [159].

- Assuming a temperature of 0.7 eV, a density of $2 \cdot 10^{18} \text{ cm}^{-3}$ and that the plasma is a fully ionized hydrogen plasma, the **plasma pressure** p at the beginning of the discharge is

$$p = p_{\text{ideal}} - \Delta p = (n_e + n_i) k_B T - \Delta p,$$

where Δp is a correction due to the plasma non-ideality [44,46] given by

$$\Delta p = \frac{e^2}{24\pi\epsilon_0 \lambda_D} \cdot (n_e + n_i).$$

We found that $p \simeq 4.2$ bar. Since the density decreases during the discharge, the pressure is also decreasing. The value found is lower than the pressure calculated with the simulation [40] ($\sim 10^3$ bar). But the assumption of a fully ionized hydrogen plasma is obviously a simplification. In reality, the plasma composition is more complex and the plasma is partially ionized (the H_α line is emitted by neutral hydrogen atoms). The pressure is thus higher than 4.2 bar, depending on the ionization degree of the plasma. Nevertheless, the pressure is still much lower than the value found with the simulation.

- The estimated **dimensions** of the plasma are summarized in figure 7.6. The electrode gap is around $100 \mu\text{m}$, and the plasma radius in the middle of the gap is also around $100 - 200 \mu\text{m}$, growing with time. The contact surface between the plasma

and the electrodes can be estimated from measurements of crater diameter, and is $\sim 10 \mu\text{m}$. Therefore, the **current density** j flowing through the plasma, and especially through the electrode–plasma interface, is extremely high, in the order of $10^6 - 10^7 \text{ A/cm}^2$.

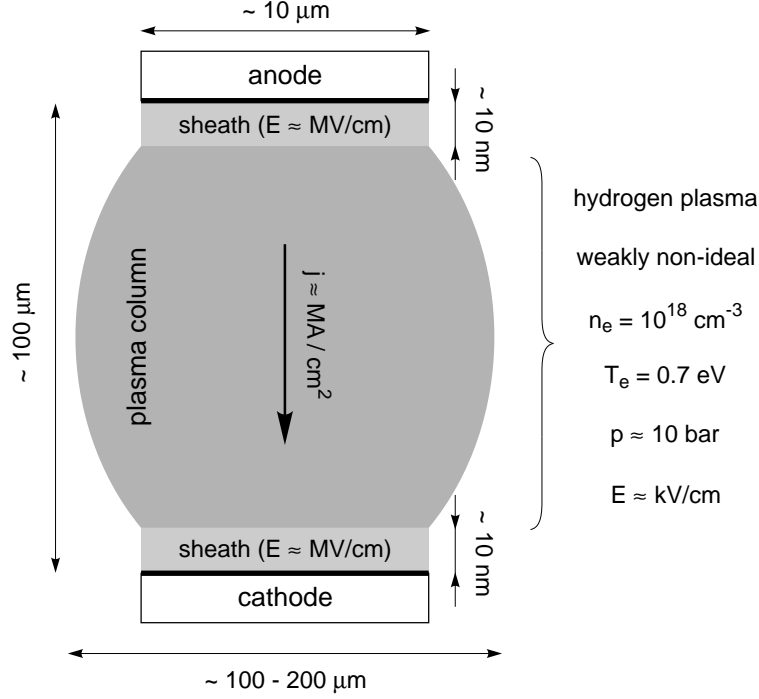


Figure 7.6: Schematic image of the general physical properties of the EDM plasma.

- Assuming a potential profile similar to those of electric arcs (see figure 2.3), most of the voltage jump is located in thin sheaths near the electrodes. The sheath thickness is in the order of the Debye length [53], $\sim 10 \text{ nm}$ in our case. The **electric field** is thus very intense in these regions, about 10^6 V/cm . Consequently, electrons are emitted from the cathode mainly by thermo-field emission. The global field in the plasma column is lower, about $10^2 - 10^3 \text{ V/cm}$. On the other hand, the microfield seen by the particles is also around 10^6 V/cm , due to the high plasma density.
- In a non-ideal plasma, the movement of an electron is mainly influenced by interactions with ions. The **mean free path** of an electron λ_e is thus given by

$$\lambda_e = \frac{1}{n_i Q_{ei}} ,$$

where Q_{ei} is the cross section of thermal electron–ion scattering. This cross section can be theoretically calculated for a strongly ionized non-ideal plasma [44]. The result is

$$Q_{ei} = 4\pi \left(\frac{Ze^2}{12\pi\epsilon_0 k_B T} \right)^2 \cdot \ln \Lambda ,$$

where $\ln \Lambda$ is the Coulomb logarithm. In the case of non-ideal plasma, the usual Coulomb logarithm has to be replaced by

$$\ln \Lambda = \frac{1}{2} \cdot \ln \left[1 + \left(\frac{3}{\Gamma_D} \right)^2 \right] , \quad (7.9)$$

where Γ_D is a parameter similar to the coupling parameter Γ defined by

$$\Gamma_D \doteq \frac{Z^2 e^2}{4\pi\epsilon_0 \lambda_D k_B T} .$$

Note that $\Gamma_D \propto \Gamma^{3/2}$. For EDM plasmas, $\Gamma_D \simeq 0.33$ and therefore $\ln \Lambda \simeq 2.2$. The cross section is thus $Q_{ei} \simeq 1.3 \cdot 10^{-13} \text{ cm}^2$ and the electron mean free path $\lambda_e \simeq 80 \text{ nm}$.

- Related to the electron–ion scattering cross section, the plasma **electrical conductivity** σ can be estimated from the *Spitzer conductivity*, which is valid for fully ionized plasmas where electron–ion collisions are dominant. The Spitzer conductivity is given by

$$\sigma = \gamma_E \cdot \frac{2(4\pi\epsilon_0)^2 (2k_B T)^{3/2}}{\pi^{3/2} Z e^2 m_e^{1/2} \ln \Lambda} , \quad (7.10)$$

where γ_E is a constant depending on Z , which takes account of electron–electron collisions [44, 46, 160]. For singly charged ions ($Z = 1$), we have $\gamma_E = 0.582$ and thus

$$\sigma = 1.53 \cdot 10^{-2} \cdot \frac{T^{3/2}}{\ln \Lambda} \quad [\Omega^{-1} \text{m}^{-1}] ,$$

with T in K. The Spitzer conductivity holds for ideal plasmas ($\ln \Lambda \geq 10$), but can be applied to weakly non-ideal plasmas if the Coulomb logarithm is replaced by the modified Coulomb logarithm given in equation (7.9) [44]. The value found is $\sigma \simeq 5 \cdot 10^3 \Omega^{-1} \text{m}^{-1}$, much lower than the conductivity of ideal plasmas ($\sim 10^6 \Omega^{-1} \text{m}^{-1}$).

- Besides the discharge on-time, the other discharge parameters (current, dielectric, electrode materials, polarity) have roughly **no significant influence** on the general plasma physical properties enumerated here.

Chapter 8

Conclusions

Although Electrical Discharge Machining is known, used and studied since the 1950's, the plasma created during this process remains puzzling. The important lack of knowledge about this plasma is mainly due to the complexity of the phenomena occurring during EDM, but also to the experimental difficulties encountered for its characterization. The EDM plasma is small, weakly luminous, of short duration, in a difficult environment, of stochastic nature and poorly reproducible.

To our knowledge, this work is the first systematic investigation of the EDM plasma with various diagnostics. Considering the significant experimental difficulties related to it, the first success of this work is simply to have shown the applicability of plasma diagnostics to the EDM discharges, particularly optical emission spectroscopy. The efforts made for the application of the diagnostics have been well rewarded. The results obtained are found to be extremely rich, and have permitted us to draw interesting conclusions about the physical properties of this plasma, and also about the different phases of the EDM process in general.

The pre-breakdown in water is characterized by the generation of numerous small hydrogen bubbles at the cathode, created by electrolysis. These bubbles certainly enhance the triggering of the breakdown, since the propagation of streamers is strongly facilitated in a gaseous medium. On the other hand, no bubbles are observed during the pre-breakdown in oil. In this dielectric, the breakdown process can rather be facilitated by the presence of particles in the gap.

Fast current pulses have been measured during the pre-breakdown, which are associated with the propagation of streamers. The occurrence of these pulses increases with the liquid conductivity. As expected, a weak light emission is also observable and is correlated with the pre-breakdown current.

The duration of the pre-breakdown phase is not constant for given discharge parameters, but the values are distributed following a Weibull distribution. This shows that the breakdown process is of stochastic nature, depending strongly on the dielectric and electrode properties.

After the breakdown, the plasma is established very rapidly, in less than 50 ns as observed with fast imaging. The plasma light intensity is particularly high immediately after the breakdown and approximately during the first 500 ns. This first phase is quite different from the rest of the discharge, and the development of generators capable of producing ultra-short discharges could be interesting for a very superficial machining.

During the rest of the discharge, the emitted light is weaker, and its intensity depends mostly on the discharge current (more intense with higher current). Imaging shows that the discharge excites a broad volume around the electrode gap, typically 200 μm in diameter, brighter in its center. This volume also clearly increases with the discharge current. The plasma is found to grow slightly during the discharge, as expected according to crater measurements reported elsewhere. Vapor bubbles are generated in water as in oil, by the heat released from the plasma.

At the end of the discharge when the current is shut down, the plasma implodes and disappears quickly. The ejection of eroded metallic particles out of the gap is observable with imaging during the post-discharge. These particles emit light by incandescence, which is confirmed by spectroscopic measurements. The spectrum of the post-discharge light is indeed close to a blackbody spectrum at roughly 2'200 K, demonstrating also that the eroded particles are still in a liquid state immediately after the end of the discharge.

The spectroscopic analysis of the plasma light gives information about the plasma composition. It is mostly composed by species coming from the cracking of the dielectric molecules, mainly hydrogen in the case of water and oil. Since the plasma is formed from the dielectric, the H_α line, for example, is emitted by the whole plasma volume. The presence of numerous metallic spectral lines indicates that the electrodes are also contaminating the plasma. Time- and spatially-resolved measurements show that the contamination is slightly higher in the vicinity of each electrode, and that the contamination coming from the workpiece increases during the discharge, probably due to vaporization.

Workpiece erosion or electrode wear regime can also qualitatively be differentiated with spectroscopy. Changing the electrode polarity produces in fact very different spectra. An increase in the discharge current has also an effect. Since discharges with high current produce larger craters, the metallic spectral lines are more intense with a high discharge current.

Almost all the spectral lines observed are atomic lines and not ionic lines, which indicates that the plasma is cold. The electron temperature, determined with the two-line method from copper line intensity measurements, is around 0.7 eV in the whole plasma, slightly higher in the beginning of the discharge. This confirms that the EDM plasma has a low temperature.

Discharges with short on-times produce spectra with strongly-broadened lines, especially the H_α line, and with an important continuum radiation. Time-resolved spectroscopy confirms these observations. During the first microsecond, spectral lines are so broadened that they are all merged into a continuum. This effect is due to the high plasma density in the very beginning of the discharge. Time- and spatially-resolved measurements of the electron density, based on Stark broadening and shift measurements of the H_α line, show that the density is above 10^{18} cm^{-3} in the beginning, and then decreases during

the discharge. But even after 50 μs , the electron density remains high, above 10^{16} cm^{-3} . During the whole discharge, the density measured is slightly higher in the plasma center.

The EDM plasma has such a high density because it is formed from a liquid, which is a dense medium, and because it is constantly submitted to the pressure imposed by the surrounding liquid. The strong intensity of the continuum radiation can be related to the high electron density. Free-bound and free-free radiations are indeed more likely in a dense plasma. The high electron density also indicates that the plasma is certainly in LTE.

As previously mentioned, the EDM plasma is cold and dense. With a typical electron temperature of 0.7 eV and a typical electron density of 10^{18} cm^{-3} , its coupling parameter Γ is around 0.3, demonstrating that it is weakly non-ideal. Evaluations of the Debye length, of the mean inter-particle distance and of the Coulomb logarithm, for example, also show the non-ideality of the EDM plasma.

Furthermore, spectroscopic results confirm this conclusion. The broadening, the shift, the asymmetrical shape and the structure of the H_α line are characteristic signs of the non-ideality of the plasma. The absence of upper Balmer lines such as the H_β line, for example, along with the merging of spectral lines in the beginning of the discharge are other demonstrations of this fact.

The physical properties of this plasma are quite fascinating. In addition to an extreme electron density, the electric fields present in the plasma and the current density are particularly high, for example. It is also remarkable that the general plasma physical properties are relatively insensitive to most of the discharge parameters, such as the discharge current, the type of dielectric, the electrode materials and polarity. Whereas these parameters certainly have a significant influence on the machining quality and efficiency, they roughly do not change the plasma densities, fields or temperatures.

Although this work has given many interesting and new results, further investigations are necessary to have a complete understanding of the EDM plasma and process. For example, we have only studied discharges used for standard erosion in die-sinking machines. Plasma created during wire-cutting operations could have different properties, since very high currents and short on-times are used (up to 1 kA during 2 μs typically). Discharges with low current ($< 6 \text{ A}$) have neither been studied, because the plasma intensity with such currents is too weak for our optical diagnostics. These discharges are used for polishing operations, where the workpiece is not significantly eroded but just superficially melted.

Furthermore, besides density and temperature measurements, optical emission spectroscopy gives mainly only qualitative results. Quantitative estimations of the plasma contamination and of the workpiece vaporization would be useful for example, but can unfortunately not be obtained with this diagnostic. The effective temperature at the workpiece surface is also another important parameter which can not be measured with emission spectroscopy.

It should be noted that the other diagnostics which can still be applied to the EDM plasma are few. With miniaturized optical fibres, active spectroscopic methods with lasers could be possibly developed. Measurement of the electron density could thus be

performed with interferometry, and information about bubbles and eroded particles could be obtained with light scattering and absorption measurements. Acoustic diagnostics could also be developed for the study of the formation, expansion and collapse of the plasma and of bubbles [161].

The implementation of spectroscopic diagnostics on industrial machines could be conceivable in the long term. Such diagnostics could be used to control the dielectric cleanliness or to detect transitions into arcs, for example.

This first investigation of the EDM plasma has emphasized its complexity and has also opened new questions. It will be important in the future to correlate the properties of the plasma with the performances and relevant characteristics of the EDM process, in order to define the “perfect plasma” for EDM. To have a complete comprehension of the mechanisms of erosion and wear for example, we should understand precisely how the energy is distributed between the plasma, the electrode and the workpiece, and how it is transferred to them during the discharge. Until now, we can only compare with similar situations, such as cathode spots in high-pressure arcs, for example. But we do not have direct measurements of the heating and transfer mechanisms from the plasma to the electrodes. A deep understanding of this could also explain in detail the origin of the asymmetry between wear and erosion, which is a characteristic and crucial feature of the EDM process. Moreover, with a better comprehension and control of the breakdown phenomenon, more reproducible discharges could be obtained, which is also important from the industrial point of view.

In conclusion, this work has given a first insight into fundamental aspects of the EDM plasma. In our opinion, we are convinced that such a study is necessary for further improvements of the process, and that other investigations should be carried on. Like any other fundamental study, it is clear that this work cannot answer now all the questions related to the EDM process, and that no immediate industrial improvements and direct applications can be obtained from it. Nevertheless, some of the results presented here have already been implemented in a simulation program developed by Charmilles Technologies, which calculates and optimizes the heat exchange during the discharge. This demonstrates that this work is a first promising step towards a better understanding of the EDM process, and possibly towards future developments of this technique.

Appendix A

Stark broadening and shift of hydrogen spectral lines

The *Stark effect* is the modification of the energy levels of an atom, a molecule or an ion, due to the presence of an external electric field. The Zeeman effect is the equivalent of the Stark effect, but for the magnetic field.

The *Stark broadening* is the broadening of spectral lines, caused by the modification of the emitter energy levels by the Stark effect. In this case, the external electric field is a local micro-field created by charged particles (ions or electrons) colliding with the emitter. Though the Stark broadening affects every atom, we will present here some results for the hydrogen atom only. Since we use the Stark broadening of the H_α line for the electron density determination, we will focus especially on the levels $n = 2$ and $n = 3$.

A.1 The Stark effect on hydrogen levels

The Hamiltonian H describing the electron of the hydrogen atom exposed to an electric field is composed of :

- the unperturbed Hamiltonian

$$H_0 = \frac{\mathbf{p}^2}{2m_e} - \frac{e^2}{4\pi\epsilon_0 R} ,$$

where $\mathbf{p} = -i\hbar\vec{\nabla}$ is the impulsion operator, \mathbf{R} the position operator, m_e and e the mass and the charge of the electron. Note that if we take into account the spin-orbit interaction and relativistic effects, the Hamiltonian becomes

$$H_0 = \frac{\mathbf{p}^2}{2m_e} - \frac{e^2}{4\pi\epsilon_0 R} + \frac{1}{2m_e^2 c^2} \frac{e^2}{4\pi\epsilon_0 R^3} \mathbf{L} \cdot \mathbf{S} + \text{relativistic terms} ,$$

where \mathbf{L} is the angular momentum operator and \mathbf{S} the spin operator [162]. This Hamiltonian describes the *fine structure* of the hydrogen atom.

- the Stark perturbing term W_S due to the electric field \mathbf{F}

$$W_S = -e \mathbf{F} \cdot \mathbf{R} .$$

Thus we have :

$$H = H_0 + W_S = \frac{\mathbf{p}^2}{2m_e} - \frac{e^2}{4\pi\epsilon_0 R} - e \mathbf{F} \cdot \mathbf{R} . \quad (\text{A.1})$$

Treating W_S with the perturbation theory, we found that, to first order, the unperturbed energy level E_n is split into $(2n - 1)$ new levels $E_n^{(1)}$ given by

$$E_n^{(1)} = E_n + n(n_2 - n_1) \cdot \Delta , \quad (\text{A.2})$$

with $0 \leq n_1, n_2 < n$ [163]. For example, the level $n = 3$ will be split into 5 levels : E_3 , $E_3 \pm 3\Delta$ and $E_3 \pm 6\Delta$. The difference in energy between the new levels are multiples of Δ , given by

$$\Delta = \frac{6\pi \hbar^2 \epsilon_0}{m_e e} \cdot F . \quad (\text{A.3})$$

We see that Δ is linear with F . The effect of the electric field on the levels given by (A.2) is thus called the *linear Stark effect*.

Taking the fine structure into account, the equation (A.2) has to be modified as follows:

$$E_n^{(1)} = E_n + n(n_2 - n_1)\Delta + k m_l m_s , \quad (\text{A.4})$$

where m_l is the magnetic quantum number, m_s the spin quantum number and k a constant (for example $k = 3 \cdot 10^{-5}$ eV for E_2 ; $8.9 \cdot 10^{-6}$ eV for $E_3 - 3\Delta$; $1.7 \cdot 10^{-6}$ eV for E_3 and $E_3 + 3\Delta$).

The calculation of the energy levels (without the fine structure) at the second order of the perturbation theory modifies equation (A.2) by adding a term quadratic in F . We obtain

$$E_n^{(2)} = E_n + \underbrace{\left[n(n_2 - n_1) \frac{3a_0 e}{2} \right]}_{E_n^{(1)}} \cdot F - \left[n^4 \left(17n^2 - 3(n_2 - n_1)^2 - 9m_l^2 + 19 \right) \frac{a_0^3}{16} \right] \cdot F^2 ,$$

where a_0 is the Bohr radius [163]. The energy shift given by this quadratic term is called the *quadratic Stark effect*.

The linear Stark effect is almost only significant for the hydrogen atom and hydrogen-like ions, and with a strong electric field (the field is called *weak* when the Stark splitting is small compared with the fine structure splitting, and *strong* otherwise). The quadratic

effect is almost negligible for hydrogen. Other elements are sensitive to the quadratic effect, but the effect is small especially for heavy elements. The hydrogen lines are thus the most broadened ones in a multi-element spectrum.

A.2 Consequences of the Stark effect on H_α emission

As previously mentioned, the H_α line is emitted by the transition from the level $n = 3$ to $n = 2$. Figure A.1 shows the splitting of these two levels by the Stark effect, according to equation (A.2).

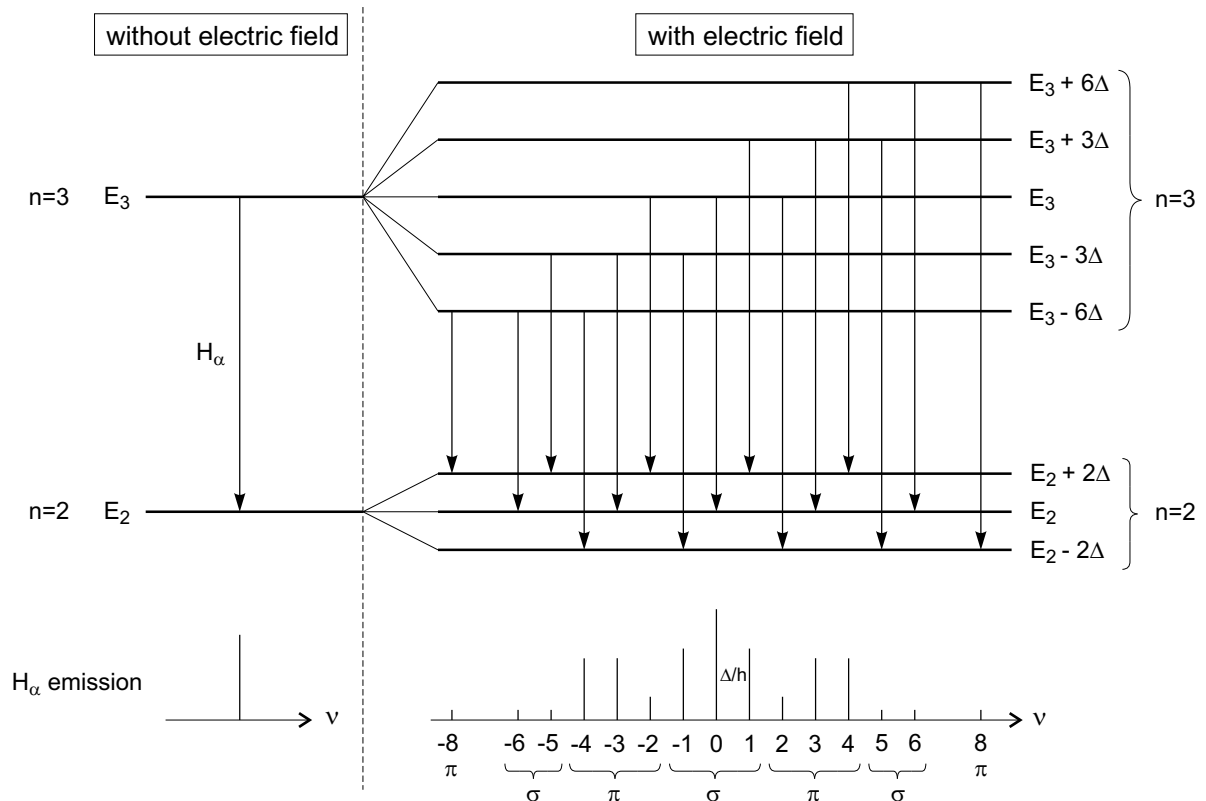


Figure A.1: Splitting of the levels $n = 2$ and $n = 3$ of the hydrogen atom due to the Stark effect, and its consequences on H_α emission.

Due to the levels splitting, the possible transitions are multiplied. The H_α emission is not a single line anymore, but it is composed of several lines. Figure A.1 shows also the frequencies emitted by these new transitions (the zero frequency reference is the transition from E_3 to E_2). The letters π and σ denote the polarization of the emitted light. The polarization π corresponds to a transition with $\Delta m_l = 0$, with the electric vector parallel to the electric field; the polarization σ corresponds to a transition with $\Delta m_l = \pm 1$, with the electric vector perpendicular to the electric field [163].

The frequency range covered by the H_α emission is thus larger with an electric field than without it. This results in the broadening of the H_α emission: this is the origin of the

Stark broadening. If the plasma density increases, the electric field seen by the emitter will also increase, because the charged perturbing particles will be closer. As a result, Δ will be larger according to equation (A.3). So we qualitatively see that the H_α frequency range, i.e. the Stark broadening of H_α , increases with density.

Taking into account the fine structure of the hydrogen atom, the H_α emission is composed of several lines even without electric field, because a splitting of the levels already exist with $F = 0$. But the number of lines is also increased by the Stark effect, as shown in figure A.2 according to equation (A.4).

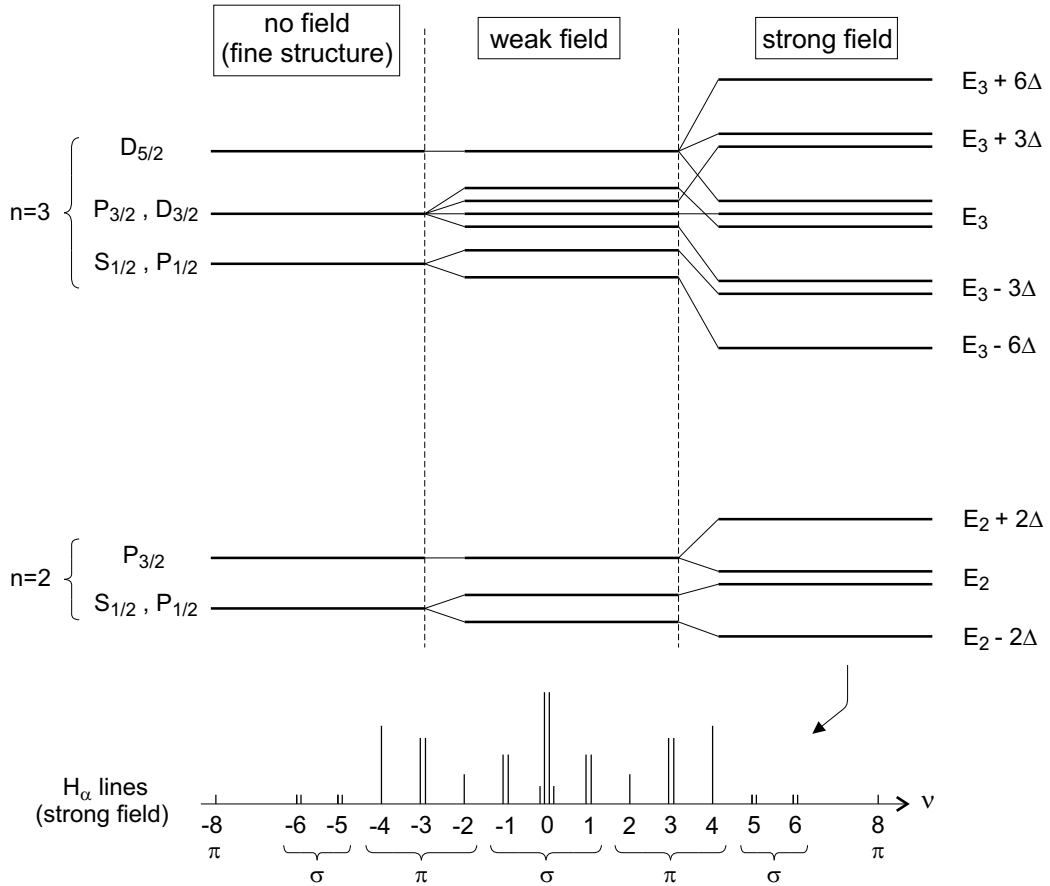


Figure A.2: Fine structure of the levels $n = 2$ and $n = 3$ of the hydrogen atom, splitting due to the Stark effect in weak and strong field, and H_α emission in strong field.

In addition to the broadening, the H_α emission is also shifted to higher wavelengths. Equation (A.4) shows that the center of gravity of the H_α emission ($E_3 - E_2$) is shifted from its position without field, due to the last term. However, this is not sufficient to explain the measured shifts of hydrogen lines. While we can give a simple explanation for the Stark broadening, the origin of the Stark shift of spectral lines is much more complicated. It involves several effects such as the quadratic Stark effect, interaction with field gradient and emitters-electrons collisions, whereas Stark broadening involves mainly emitter-ion collisions [107].

Although the origin of line shape modification by Stark effect can be simply understood as presented here, the precise calculations of line broadening and shift require sophisticated models [112–117].

References

- [1] <http://www.charmilles.ch> .
- [2] <http://www.agie-charmilles.com> .
- [3] B. M. Schumacher, “After 60 years of EDM the discharge process remains still disputed”, *J. Mater. Process. Technol.*, **149**, 376–381 (2004).
- [4] A. Anders, “Tracking down the origin of arc plasma science, I. Early pulsed and oscillating discharges”, *IEEE Trans. Plasma Sci.*, **31**(4), 1052–1059 (2003).
- [5] J. Priestley, “Experiments on the circular spots made on pieces of metal by large electrical explosions”, in *The history and present state of electricity with original experiments*, vol. II, 3rd ed., London (1775).
- [6] B. Dibner, *Galvani - Volta, A controversy that led to the discovery of useful electricity*, CT: Burndy Library, Norwalk (1952).
- [7] A. Anders, “Tracking down the origin of arc plasma science, II. Early continuous discharges”, *IEEE Trans. Plasma Sci.*, **31**(4), 1060–1069 (2003).
- [8] *Handbook of vacuum arc science and technology, fundamentals and applications*, edited by R. L. Boxman, D. M. Sanders and P. J. Martin, Noyes publications, Park Ridge (1995).
- [9] B. R. Lazarenko, *About the inversion of metal erosion and methods to fight ravage of electric contacts*, WEI-Institut, Moscow (in Russian) (1943).
- [10] L. H. Germer and F. E. Haworth, “Erosion of electrical contacts on make”, *J. Appl. Phys.*, **20**(11), 1085–1109 (1949).
- [11] J. D. Cobine and E. E. Burger, “Analysis of electrode phenomena in the high-current arc”, *J. Appl. Phys.*, **26**(7), 895–900 (1955).
- [12] A. S. Zingerman, “The effect of thermal conductivity upon the electrical erosion of metals”, *Sov. Phys. Tech. Phys.*, **1**, 1945–1958 (1956).
- [13] T. Sato, T. Mizutani, and K. Kawata, “Electro-discharge machine for microhole drilling”, *National Technical Report*, **31**, 725–733 (in Japanese) (1985).

- [14] D. F. Dauw and B. Van Coppenolle, “On the evolution of EDM research, part 2: From fundamental research to applied research”, in *Proceedings of the 11th International Symposium for Electro Machining (ISEM-11)*, 133–142 (Lausanne, Switzerland, 1995).
- [15] K. Kobayashi, “The present and future developments of EDM and ECM”, in *Proceedings of the 11th International Symposium for Electro Machining (ISEM-11)*, 29–47 (Lausanne, Switzerland, 1995).
- [16] R. Löttgen, “EDM die-sinking - state of the art”, in *Proceedings of the 12th International Symposium for Electro Machining (ISEM-12)*, 341–350 (Aachen, Germany, 1998).
- [17] K. H. Ho and S. T. Newman, “State of the art electrical discharge machining (EDM)”, *Int. J. Mach. Tools and Manufacture*, **43**(13), 1287–1300 (2003).
- [18] K. H. Ho, S. T. Newman, S. Rahimifard, and R. D. Allen, “State of the art in wire electrical discharge machining (WEDM)”, *Int. J. Mach. Tools and Manufacture*, **44**(12-13), 1247–1259 (2004).
- [19] B. Lauwers, J.-P. Kruth, W. Liu, W. Eeraerts, B. Schacht, and P. Bleys, “Investigation of material removal mechanisms in EDM of composite ceramic materials”, *J. Mater. Process. Technol.*, **149**, 347–352 (2004).
- [20] T. Tani, Y. Fukuzawa, N. Mohri, N. Saito, and M. Okada, “Machining phenomena in WEDM of insulating ceramics”, *J. Mater. Process. Technol.*, **149**, 124–128 (2004).
- [21] H. Takezawa, H. Hamamatsu, N. Mohri, and N. Saito, “Development of micro-EDM-center with rapidly sharpened electrode”, *J. Mater. Process. Technol.*, **149**, 112–116 (2004).
- [22] J. Fleischer, T. Masuzawa, J. Schmidt, and M. Knoll, “New applications for micro-EDM”, *J. Mater. Process. Technol.*, **149**, 246–249 (2004).
- [23] I. Beltrami, C. Joseph, R. Clavel, J.-P. Bacher, and S. Bottinelli, “Micro- and nano-electric discharge machining”, *J. Mater. Process. Technol.*, **149**, 263–265 (2004).
- [24] C. Joseph, *Contribution à l’accroissement des performances du processus de micro-EDM par l’utilisation d’un robot à dynamique élevée et de haute précision*, PhD thesis, Ecole Polytechnique Fédérale de Lausanne, Switzerland (2005).
- [25] G. Cusanelli, A. Hessler-Wyser, F. Bobard, R. Demellayer, R. Perez, and R. Flükiger, “Microstructure at submicron scale of the white layer produced by EDM technique”, *J. Mater. Process. Technol.*, **149**, 289–295 (2004).
- [26] F. Klocke, D. Lung, G. Antonoglou, and D. Thomaidis, “The effects of powder suspended dielectrics on the thermal influenced zone by electrodischarge machining with small discharge energies”, *J. Mater. Process. Technol.*, **149**, 191–197 (2004).

- [27] S. Das, M. Klotz, and F. Klocke, “EDM simulation: finite element-based calculation of deformation, microstructure and residual stresses”, *J. Mater. Process. Technol.*, **142**(2), 434–451 (2003).
- [28] R. Perez, H. Rojas, G. Wälder, and R. Flükiger, “Theoretical modeling of energy balance in electroerosion”, *J. Mater. Process. Technol.*, **149**, 198–203 (2004).
- [29] H.-P. Schulze, R. Herms, H. Juhr, W. Schätzing, and G. Wollenberg, “Comparison of measured and simulated crater morphology for EDM”, *J. Mater. Process. Technol.*, **149**, 316–322 (2004).
- [30] J. C. Devins, S. J. Rzađ, and R. J. Schwabe, “Breakdown and prebreakdown phenomena in liquids”, *J. Appl. Phys.*, **52**(7), 4531–4545 (1981).
- [31] P. E. Frayssines, N. Bonifaci, A. Denat, and O. Lesaint, “Streamers in liquid nitrogen: characterization and spectroscopic determination of gaseous filament temperature and electron density”, *J. Phys. D: Appl. Phys.*, **35**(4), 369–377 (2002).
- [32] E. O. Forster, “Progress in the understanding of electrical breakdown in condensed matter”, *J. Phys. D: Appl. Phys.*, **23**(12), 1506–1514 (1990).
- [33] E. A. Martin, “Experimental investigation of a high-energy density, high-pressure arc plasma”, *J. Appl. Phys.*, **31**(2), 255–267 (1960).
- [34] P. Barmann, S. Kröll, and A. Sunesson, “Spectroscopic measurements of streamer filaments in electric breakdown in a dielectric liquid”, *J. Phys. D: Appl. Phys.*, **29**(5), 1188–1196 (1996).
- [35] S. V. Kukhlevsky, Cs. Ver, J. Kaiser, L. Kozma, L. Palladino, A. Reale, G. Tomasetti, F. Flora, and G. Giordano, “Generation of pure, high-density metal-vapor plasma by capillary discharge”, *Appl. Phys. Lett.*, **74**(19), 2779–2781 (1999).
- [36] G. Wälder, “New technologies and EDM”, in *Proceedings of the 12th International Symposium for Electro Machining (ISEM-12)*, 331–340 (Aachen, Germany, 1998).
- [37] F. Van Dijck, *Physico-mathematical analysis of the electro discharge machining process*, PhD thesis, Catholic University of Leuven, Belgium (1973).
- [38] D. D. DiBitonto, P. T. Eubank, M. R. Patel, and M. A. Barrufet, “Theoretical models of the electrical discharge machining process. I. A simple cathode erosion model”, *J. Appl. Phys.*, **66**(9), 4095–4103 (1989).
- [39] M. R. Patel, M. A. Barrufet, P. T. Eubank, and D. D. DiBitonto, “Theoretical models of the electrical discharge machining process. II. The anode erosion model”, *J. Appl. Phys.*, **66**(9), 4104–4111 (1989).
- [40] P. T. Eubank, M. R. Patel, M. A. Barrufet, and B. Bozkurt, “Theoretical models of the electrical discharge machining process. III. The variable mass, cylindrical plasma model”, *J. Appl. Phys.*, **73**(11), 7900–7909 (1993).

- [41] K. Albinski, K. Musiol, A. Miernikiewicz, S. Labuz, and M. Malota, “The temperature of a plasma used in electrical discharge machining”, *Plasma Sources Sci. Technol.*, **5**(4), 736–742 (1996).
- [42] B. W. Pillans, M. H. Evensen, H. F. Taylor, P. T. Eubank, and L. Ma, “Fiber optic diagnostic techniques applied to electrical discharge machining sparks”, *J. Appl. Phys.*, **91**(4), 1780–1786 (2002).
- [43] V. E. Fortov and I. T. Iakubov, *Physics of nonideal plasma*, Hemisphere, New York (1990).
- [44] *Transport and optical properties of nonideal plasma*, edited by G. A. Kobzev, I. T. Iakubov and M. M. Popovich, Plenum Press, New York (1995).
- [45] R. Redmer, “Physical properties of dense, low-temperature plasmas”, *Phys. Rep.*, **282**(2-3), 35–157 (1997).
- [46] K. Günther and R. Radtke, *Electric properties of weakly nonideal plasmas*, Birkhäuser Verlag, Basel (1984).
- [47] J. M. Meek and J. D. Craggs, *Electrical breakdown of gases*, Clarendon Press, Oxford (1953).
- [48] L. B. Loeb, “Electrical breakdown of gases with steady or direct current impulse potentials”, in *Encyclopedia of Physics, volume XXII: Gas discharges II*, edited by S. Flügge, Springer Verlag, Berlin (1956).
- [49] Y. P. Raizer, *Gas discharge physics*, Springer-Verlag, Berlin (1991).
- [50] A. E. Guile and B. Jüttner, “Basic erosion processes of oxidized and clean metal cathodes by electric arcs”, *IEEE Trans. Plasma Sci.*, **8**(3), 259–269 (1980).
- [51] C. W. Kimblin, “A review of arcing phenomena in vacuum and in the transition to atmospheric pressure arcs”, *IEEE Trans. Plasma Sci.*, **10**(4), 322–330 (1982).
- [52] V. I. Rakhovsky, “State of the art of physical models of vacuum arc cathode spots”, *IEEE Trans. Plasma Sci.*, **15**(5), 481–487 (1987).
- [53] M. S. Benilov and A. Marotta, “A model of the cathode region of atmospheric pressure arcs”, *J. Phys. D: Appl. Phys.*, **28**(9), 1869–1882 (1995).
- [54] R. L. Boxman, S. Goldsmith, and A. Greenwood, “Twenty-five years of progress in vacuum arc research and utilization”, *IEEE Trans. Plasma Sci.*, **25**(6), 1174–1186 (1997).
- [55] I. I. Beilis, “State of the theory of vacuum arcs”, *IEEE Trans. Plasma Sci.*, **29**(5), 657–670 (2001).
- [56] E. Hantzsche, “Mysteries of the arc cathode spot: a retrospective glance”, *IEEE Trans. Plasma Sci.*, **31**(5), 799–808 (2003).

- [57] B. Jüttner, V. F. Puchkarev, E. Hantzsch, and I. Beilis, “Cathode spots”, in *Handbook of vacuum arc science and technology, fundamentals and applications*, edited by R. L. Boxman, D. M. Sanders and P. J. Martin, Noyes publications, Park Ridge (1995).
- [58] A. W. Behrens, J. Ginzel, and F.-L. Bruhns, “Threshold technology and its application for gap status detection”, *J. Mater. Process. Technol.*, **149**, 310–315 (2004).
- [59] P. K. Watson, W. G. Chadband, and M. Sadeghzadeh-Araghi, “The role of electrostatic and hydrodynamic forces in the negative-point breakdown of liquid dielectrics”, *IEEE Trans. Electr. Ins.*, **26**(4), 543–559 (1991).
- [60] W. G. Chadband, “The electrical breakdown of insulating oil”, *Power Engineering Journal*, , 61–67 (March 1992).
- [61] R. Tobazéon, “Prebreakdown phenomena in dielectric liquids”, *IEEE Trans. Diel. Electr. Ins.*, **1**(6), 1132–1147 (1994).
- [62] H. M. Jones and E. E. Kunhardt, “Development of pulsed dielectric breakdown in liquids”, *J. Phys. D: Appl. Phys.*, **28**(1), 178–188 (1995).
- [63] A. Beroual, M. Zahn, A. Badent, K. Kist, A. J. Schwabe, H. Yamashita, K. Yamazawa, M. Danikas, W. D. Chadband, and Y. Torshin, “Propagation and structure of streamers in liquid dielectrics”, *IEEE Electr. Insul. Mag.*, **14**(2), 6–17 (1998).
- [64] I. V. Lisitsyn, H. Nomiya, S. Katsuki, and H. Akiyama, “Thermal processes in a streamer discharge in water”, *IEEE Trans. Diel. Electr. Ins.*, **6**(3), 351–356 (1999).
- [65] H. M. Jones and E. E. Kunhardt, “The influence of pressure and conductivity on the pulsed breakdown of water”, *IEEE Trans. Diel. Electr. Ins.*, **1**(6), 1016–1025 (1994).
- [66] O. Lesaint and G. Massala, “Positive streamer propagation in large oil gaps, Experimental characterization of propagation modes”, *IEEE Trans. Diel. Electr. Ins.*, **5**(3), 360–370 (1998).
- [67] G. Massala and O. Lesaint, “Positive streamer propagation in large oil gaps, Electrical properties of streamers”, *IEEE Trans. Diel. Electr. Ins.*, **5**(3), 371–381 (1998).
- [68] A. Denat, F. Jomni, F. Aitken, and N. Bonifaci, “Thermally and electrically induced bubbles in liquid argon and nitrogen”, *IEEE Trans. Diel. Electr. Ins.*, **9**(1), 17–22 (2002).
- [69] H. Yamada, T. Sato, and T. Fujiwara, “High-speed photography of prebreakdown phenomena in dielectric liquids under highly non-uniform field conditions”, *J. Phys. D: Appl. Phys.*, **23**(12), 1715–1722 (1990).

- [70] A. Beroual, C. Marteau, and R. Tobazéon, “Behavior of streamers in liquids under step voltages in point-plane geometry”, *IEEE Trans. Electr. Ins.*, **23**(6), 955–959 (1988).
- [71] H. Yamashita and H. Amano, “Prebreakdown phenomena in hydrocarbon liquids”, *IEEE Trans. Electr. Ins.*, **23**(4), 739–750 (1988).
- [72] O. Lesaint and P. Gournay, “Initiation and propagation thresholds of positive pre-breakdown phenomena in hydrocarbon liquids”, *IEEE Trans. Diel. Electr. Insul.*, **1**(4), 702–708 (1994).
- [73] Y. Nakao, H. Itoh, S. Hoshino, Y. Sakai, and H. Tagashira, “Effects of additives on prebreakdown phenomena in n-hexane”, *IEEE Trans. Diel. Electr. Ins.*, **1**(3), 383–390 (1994).
- [74] T. Zinoulis, I. Argirakis, D. W. Auckland, and W. G. Chadband, “The role of particles in discharge initiation in liquids”, in *IEEE 11th International Conference on Conduction and Breakdown in Dielectric Liquids (ICDL '93)*, 421–425 (Baden-Dättwil, Switzerland, 1993).
- [75] M. Hara, J. Suheiro, H. Maeda, and H. Nakashima, “DC pre-breakdown phenomena and breakdown characteristics in the presence of conducting particles in liquid nitrogen”, *IEEE Trans. Diel. Electr. Ins.*, **9**(1), 23–30 (2002).
- [76] W. G. Chadband, “From bubbles to breakdown, or vice-versa”, in *IEEE 11th International Conference on Conduction and Breakdown in Dielectric Liquids (ICDL '93)*, 184–193 (Baden-Dättwil, Switzerland, 1993).
- [77] T. Aka-Ngnui and A. Beroual, “Bubble dynamics and transition into streamers in liquid dielectrics under a high divergent electric field”, *J. Phys. D: Appl. Phys.*, **34**(9), 1408–1412 (2001).
- [78] J. Qian, R. P. Joshi, J. Kolb, K. H. Schoenbach, J. Dickens, A. Neuber, M. Butcher, M. Cevallos, H. Krompholz, E. Schamiloglu, and J. Gaudet, “Microbubble-based model analysis of liquid breakdown initiation by a submicrosecond pulse”, *J. Appl. Phys.*, **97**(11), 113304 (2005).
- [79] S. M. Korobeinikov, A. V. Melekhov, and A. S. Besov, “Breakdown initiation in water with the aid of bubbles”, *High Temperature*, **40**(5), 652–659 (2002).
- [80] R. Kattan, A. Denat, and O. Lesaint, “Generation, growth, and collapse of vapor bubbles in hydrocarbon liquids under a high divergent electric field”, *J. Appl. Phys.*, **66**(9), 4062–4066 (1989).
- [81] A. Denat, N. Bonifaci, and M. Nur, “Spectral analysis of the light emitted by streamers in hydrocarbon liquids”, *IEEE Trans. Diel. Electr. Ins.*, **5**(3), 382–387 (1998).
- [82] H. Akiyama, “Streamer discharges in liquids and their applications”, *IEEE Trans. Diel. Electr. Ins.*, **7**(5), 646–653 (2000).

- [83] M. Sato, T. Ohgiyama, and J. S. Clements, “Formation of chemical species and their effects on microorganisms using a pulsed high-voltage discharge in water”, *IEEE Trans. Ind. Appl.*, **32**(1), 106–112 (1996).
- [84] M. P. Brenner, S. Hilgenfeldt, and D. Lohse, “Single-bubble sonoluminescence”, *Rev. Mod. Phys.*, **74**(2), 425–484 (2002).
- [85] D. J. Flannigan and K. S. Suslick, “Plasma formation and temperature measurement during single-bubble cavitation”, *Nature*, **434**(7029), 52–55 (2005).
- [86] J. W. Robinson, M. Ham, and A. N. Balaster, “Ultraviolet radiation from electrical discharges in water”, *J. Appl. Phys.*, **44**(1), 72–75 (1973).
- [87] A. W. DeSilva and J. D. Katsouros, “Electrical conductivity of dense copper and aluminium plasmas”, *Phys. Rev. E*, **57**(5), 5945–5951 (1998).
- [88] A. Grinenko, A. Sayapin, V. Tz. Gurovich, S. Efimov, J. Felsteiner, and Ya. E. Krasik, “Underwater electrical explosion of a Cu wire”, *J. Appl. Phys.*, **97**(2), 023303 (2005).
- [89] J. W. Robinson, “Measurements of plasma energy density and conductivity from 3 to 120 kbar”, *J. Appl. Phys.*, **38**(1), 210–216 (1967).
- [90] S. V. Kukhlevsky, J. Kaiser, O. Samek, M. Liska, and J. Erostyak, “Stark spectroscopy measurements of electron density of ablative discharges in Teflon-(CF₂)_n capillaries”, *J. Phys. D: Appl. Phys.*, **33**(9), 1090–1092 (2000).
- [91] Y. Ping, I. Geltner, A. Morozov, and S. Suckewer, “Interferometric measurements of plasma density in microcapillaries and laser sparks”, *Phys. Plasmas*, **9**(11), 4756–4766 (2002).
- [92] L. S. Caballero, H. Chuaqui, M. Favre, I. Mitchell, and E. Wyndham, “Plasma jet emission in fast-pulsed capillary discharges”, *J. Appl. Phys.*, **98**(2), 023305 (2005).
- [93] C. Colon, G. Hatem, E. Verdugo, P. Ruiz, and J. Campos, “Measurement of the Stark broadening and shift parameters for several ultraviolet lines of singly ionized aluminium”, *J. Appl. Phys.*, **73**(10), 4752–4758 (1993).
- [94] M. A. Hafez, M. A. Khedr, F. F. Elaksher, and Y. E. Gamal, “Characteristics of Cu plasma produced by a laser interaction with a solid target”, *Plasma Sources Sci. Technol.*, **12**(2), 185–198 (2003).
- [95] Y. Zhang, L. Li, and G. Zhang, “Spectroscopic measurements of plasma inside the keyhole in deep penetration laser welding”, *J. Phys. D: Appl. Phys.*, **38**(5), 703–710 (2005).
- [96] V. A. Alekseev and I. T. Iakubov, “Non-ideal plasmas of metal vapours”, *Phys. Rep.*, **96**(1), 1–69 (1983).

- [97] K. Terashima, L. Howald, H. Haefke, and H.-J. Güntherodt, “Development of a mesoscale/nanoscale plasma generator”, *Thin Solid Films*, **281-282**, 634–636 (1996).
- [98] Y. Hirata, M. Fukushima, T. Sano, K. Ozaki, and T. Ohji, “Micro-arc discharge phenomena”, *Vacuum*, **59**(1), 142–151 (2000).
- [99] T. Ito, T. Izaki, and K. Terashima, “Development of plasma chip”, *Surf. Coat. Technol.*, **133-134**, 497–500 (2000).
- [100] C. Penache, M. Miclea, A. Bräuning-Demian, O. Hohn, S. Schlössler, T. Jahnke, K. Niemax, and H. Schmidt-Böcking, “Characterization of a high-pressure microdischarge using diode laser atomic absorption spectroscopy”, *Plasma Sources Sci. Technol.*, **11**(4), 476–483 (2002).
- [101] M. Miclea, K. Kunze, J. Franzke, and K. Niemax, “Plasmas for lab-on-the-chip applications”, *Spectrochim. Acta B*, **57**(10), 1585–1592 (2002).
- [102] R. Longwitz, *Study of gas ionization in a glow discharge and development of a micro gas ionizer for gas detection and analysis*, PhD thesis, Ecole Polytechnique Fédérale de Lausanne, Switzerland (2004).
- [103] T. Ito, T. Izaki, and K. Terashima, “Application of microscale plasma to material processing”, *Thin Solid Films*, **386**(2), 300–304 (2001).
- [104] O. B. Postel and M. A. Cappelli, “Parametric study of the vacuum ultraviolet emission and electrical characteristics of a He-Xe microdischarge”, *J. Appl. Phys.*, **89**(9), 4719–4726 (2001).
- [105] K. H. Becker, K. H. Schoenbach, and J. G. Eden, “Microplasmas and applications”, *J. Phys. D: Appl. Phys.*, **39**(3), R55–R70 (2006).
- [106] G. Sémon, *Guide pratique d’usinage par étincelage*, Ateliers des Charmilles S.A., Genève (1977).
- [107] H. R. Griem, *Principles of Plasma Spectroscopy*, University Press, Cambridge (1997).
- [108] R. Rompe and M. Steenbeck, *Progress in plasmas and gas electronics, volume 1*, Akademie-Verlag, Berlin (1975).
- [109] T. Fujimoto, *Plasma Spectroscopy*, Clarendon Press, Oxford (2004).
- [110] K. Fu, M. Jogwich, M. Knebel, and K. Wiesemann, “Atomic transition probabilities and lifetimes for the Cu I system”, *At. Data Nucl. Data Tables*, **61**(1), 1–30 (1995).
- [111] H. R. Griem, *Spectral line broadening by plasmas*, Academic, New York (1974).

- [112] M. A. Gigosos and V. Cardenoso, “New plasma diagnosis tables of hydrogen Stark broadening including ion dynamics”, *J. Phys. B: At. Mol. Opt. Phys.*, **29**(20), 4795–4838 (1996).
- [113] S. Böldeker, S. Günter, A. Könies, L. Hitzschke, and H.-J. Kunze, “Shift and width of the H alpha line of hydrogen in dense plasmas”, *Phys. Rev. E*, **47**(4), 2785–2791 (1993).
- [114] W. Olchawa, “Computer simulations of hydrogen spectral line shapes in dense plasmas”, *J. Quant. Spectrosc. Radiat. Transfer*, **74**(4), 417–429 (2002).
- [115] S. A. Flih, E. Oks, and Y. Vitel, “Comparison of the Stark widths and shifts of the H-alpha line measured in a flash tube plasma with theoretical results”, *J. Phys. B: At. Mol. Opt. Phys.*, **36**(2), 283–296 (2003).
- [116] S. Günter and A. Könies, “Shifts and asymmetry parameters of hydrogen Balmer lines in dense plasmas”, *Phys. Rev. E*, **55**(1), 907–911 (1997).
- [117] A. Escarguel, E. Oks, J. Richou, and D. Volodko, “Highly nonlinear, sign-varying shift of hydrogen spectral lines in dense plasmas”, *Phys. Rev. E*, **62**(2), 2667–2671 (2000).
- [118] W. Weibull, “A statistical distribution function of wide applicability”, *J. Appl. Mech.*, **18**, 293–297 (1951).
- [119] C. J. Frei, “Weibull statistical analysis of dielectric breakdown in n-hexane”, *IEEE Trans. on Electr. Insul.*, **20**(2), 303–307 (1985).
- [120] C. J. Frei, L. He, and K. Müller, “Implications from the influence of electrohydrodynamic motion on breakdown with respect to the discharge mechanism in dielectric liquids”, *IEEE Trans. on Electr. Insul.*, **24**(2), 169–174 (1989).
- [121] A. Karden, *Der Entladekanal - Was passiert wirklich bei der Funkenerosion?*, Bericht Nr. 272-1/00, Laboratorium für Werkzeugmaschinen und Betriebslehre, Rheinisch-Westfälischen Technischen Hochschule, Aachen (2001).
- [122] E. Gidalevich and R. L. Boxman, “Sub- and supersonic expansion of an arc channel in liquid”, *J. Phys. D: Appl. Phys.*, **39**(4), 652–659 (2006).
- [123] B. Revaz, G. Witz, and R. Flükiger, “Properties of the plasma channel in liquid discharges inferred from cathode local temperature measurements”, *J. Appl. Phys.*, **98**(11), 113305 (2005).
- [124] P. C. Pandey and S. T. Jilani, “Plasma channel growth and the resolidified layer in EDM”, *Precis. Eng.*, **8**(2), 104–110 (1986).
- [125] G. Cusanelli, PhD thesis, Université de Genève, Switzerland (2004).

- [126] A. E. Berkowitz and J. L. Walter, “Spark erosion: a method for producing rapidly quenched fine powders”, *J. Mater. Res.*, **2**(2), 277–288 (1987).
- [127] J. Carrey, H. B. Radousky, and A. E. Berkowitz, “Spark-eroded particles: Influence of processing parameters”, *J. Appl. Phys.*, **95**(3), 823–829 (2004).
- [128] C. E. Moore, *A multiplet table of astrophysical interest*, U.S. Department of Commerce, National Bureau of Standards, Washington (1959).
- [129] PLASUS SpecLine Software, <http://www.plasus.de> .
- [130] J. Reader, C. H. Corliss, W. L. Wiese, and G. A. Martin, *Wavelengths and transition probabilities for atoms and atomic ions*, U.S. Department of Commerce, National Bureau of Standards, Washington (1980).
- [131] R. W. B. Pearse and A. G. Gaydon, *The identification of molecular spectra*, Wiley, New York (1950).
- [132] NIST Atomic Spectra Database, <http://www.physics.nist.gov/PhysRefData/ASD> .
- [133] D. J. Heading, G. R. Bennett, J. S. Wark, and R. W. Lee, “Novel plasma source for dense plasma effects”, *Phys. Rev. Lett.*, **74**(18), 3616–3619 (1995).
- [134] Y. Vitel, M. El Bezzari, T. V. Gavrilova, M. Skowronek, L. G. D’yachkov, and Y. K. Kurilenkov, “On dense hydrogen and noble gases plasma spectra”, *Physica B*, **228**(1-2), 161–165 (1996).
- [135] A. Escarguel, B. Ferhat, A. Lesage, and J. Richou, “A single laser spark in aqueous medium”, *J. Quant. Spectrosc. Radiat. Transfer*, **64**(4), 353–361 (2000).
- [136] B. Revaz, J. Emery, G. Witz, R. Flükiger, R. Perez, J. Carron, and M. Rappaz, “Local temperature response to pulsed discharges in electronic discharge machining (EDM) environment”, *IEEE Trans. Plasma Sci.*, **33**(3), 1066–1071 (2005).
- [137] H. R. Griem, “Validity of local thermal equilibrium in plasma spectroscopy”, *Phys. Rev.*, **131**(3), 1170–1176 (1963).
- [138] K. Song, H. Cha, J. Lee, and Y.-I. Lee, “Investigation of the line-broadening mechanism for laser-induced copper plasma by time-resolved laser-induced breakdown spectroscopy”, *Microchem. J.*, **63**(1), 53–60 (1999).
- [139] J. D. Huba, *NRL Plasma formulary*, Naval Research Laboratory, Washington (2004).
- [140] M. M. Litvak and D. F. Edwards, “Spectroscopic studies of laser-produced hydrogen plasma”, *IEEE J. Quant. Electronics*, **2**(9), 486–492 (1966).
- [141] W. L. Wiese, D. E. Kelleher, and D. R. Paquette, “Detailed study of the Stark broadening of Balmer lines in a high-density plasma”, *Phys. Rev. A*, **6**(3), 1132–1153 (1972).

- [142] Y. Vitel, “Experimental study of H_α broadening and shift in dense argon plasmas”, *J. Phys. B: At. Mol. Phys.*, **20**(10), 2327–2337 (1987).
- [143] C. Parigger, J. W. L. Lewis, and D. Plemmons, “Electron number density and temperature measurement in a laser-induced hydrogen plasma”, *J. Quant. Spectrosc. Radiat. Transfer*, **53**(3), 249–255 (1995).
- [144] Y. Vitel, T. V. Gavrilova, L. G. D’yachkov, and Y. K. Kurilenkov, “Spectra of dense pure hydrogen plasma in Balmer area”, *J. Quant. Spectrosc. Radiat. Transfer*, **83**(3–4), 387–405 (2004).
- [145] A. Cohn, P. Bakshi, and G. Kalman, “Linear Stark effect due to resonant interactions of static and dynamic fields”, *Phys. Rev. Lett.*, **29**(6), 324–327 (1972).
- [146] C. C. Gallagher and M. A. Levine, “Balmer-line anomalies in a turbulent plasma”, *Phys. Rev. Lett.*, **30**(19), 897–900 (1973).
- [147] W. R. Rutgers and H. W. Kalfsbeek, “Calculations and measurements of the dynamic Stark effect in hydrogen”, *Z. Naturforsch.*, **30**(a), 739–749 (1975).
- [148] A. I. Zhuzhunashvili and E. A. Oks, “Technique of optical polarization measurements of plasma Langmuir turbulence spectrum”, *Sov. Phys. JETP*, **46**(6), 1122–1129 (1977).
- [149] K. H. Finken, R. Buchwald, G. Bertschinger, and H.-J. Kunze, “Investigation of the H alpha line in dense plasmas”, *Phys. Rev. A*, **21**(1), 200–206 (1980).
- [150] V. P. Gavrilenko and E. A. Oks, “Intra-Stark spectroscopy of Coulomb radiators in a plasma with quasimonochromatic electric field”, *Sov. J. Plasma Phys.*, **13**(1), 22–28 (1980).
- [151] G. Kalman and P. Bakshi, “Microfield effects: strongly coupled plasmas”, *J. Quant. Spectrosc. Radiat. Transfer*, **44**(1), 1–9 (1990).
- [152] P. Bakshi and G. Kalman, “Hydrogenic spectroscopy for various unusual plasmas”, *J. Quant. Spectrosc. Radiat. Transfer*, **44**(1), 93–100 (1990).
- [153] E. A. Oks, S. Böldeker, and H.-J. Kunze, “Spectroscopy of atomic hydrogen in dense plasmas in the presence of dynamic fields: Intra-Stark spectroscopy”, *Phys. Rev. A*, **44**(12), 8338–8347 (1991).
- [154] D. R. Inglis and E. Teller, “Ionic depression of series limits in one-electron spectra”, *Astrophys. J.*, **90**, 439–448 (1939).
- [155] C.-R. Vidal, “Determination of electron density from line merging”, *J. Quant. Spectrosc. Radiat. Transfer*, **6**(4), 461–477 (1966).
- [156] K. M. Roussel and R. F. O’Connell, “A comparison between Debye-Hückel screening and the stark effect on the determination of the last observable spectral line from a hydrogen-like plasma”, *Phys. Lett. A*, **51**(4), 244–246 (1975).

- [157] N. Konjevic, “Plasma broadening and shifting of non-hydrogenic spectral lines: present status and applications”, *Phys. Rep.*, **316**(6), 339–401 (1999).
- [158] N. Konjevic and W. L. Wiese, “Experimental Stark widths and shifts for spectral lines of neutral and ionized atoms”, *J. Phys. Chem. Ref. Data*, **19**(6), 1307–1385 (1990).
- [159] M. R. Zaghloul, M. A. Bourham, and J. M. Doster, “A simple formulation and solution strategy of the Saha equation for ideal and nonideal plasmas”, *J. Phys. D: Appl. Phys.*, **33**(8), 977–984 (2000).
- [160] L. Spitzer and R. Härm, “Transport phenomena in a completely ionized gas”, *Phys. Rev.*, **89**(5), 977–981 (1953).
- [161] J. W. Mackersie, I. V. Timoshkin, and S. J. MacGregor, “Generation of high-power ultrasound by spark discharges in water”, *IEEE Trans. Plasma Sci.*, **33**(5), 1715–1724 (2005).
- [162] C. Cohen-Tannoudji, B. Diu, and F. Laloë, *Mécanique quantique*, Hermann, Paris (1973).
- [163] H. G. Kuhn, *Atomic Spectra*, Longmans, London (1962).

Acknowledgments

This last chapter is undoubtedly the most pleasant one to write. It would have been impossible to complete this thesis without the help of many people. Since they all understand my mother tongue, I wish to warmly thank them *en français dans le texte*.

Mes remerciements vont naturellement tout d'abord au Dr Christoph Hollenstein, directeur du groupe des plasmas industriels du CRPP et directeur de ma thèse, sans qui rien n'aurait été possible et grâce à qui j'ai beaucoup appris. Travailler sous sa supervision, et ainsi pouvoir profiter de sa grande expérience et de son sens aigu de la physique, a été un réel plaisir pendant ces cinq ans. Ses qualités scientifiques mais aussi humaines ont largement contribué au succès de mon travail de thèse. Merci énormément, Christoph !

Je remercie très sincèrement les personnes de Charmilles Technologies qui ont collaboré à ce projet, spécialement le Dr Georg Wälder qui m'a suivi pendant tout ce travail et qui m'a fait le plaisir d'être membre de mon jury. Un grand merci également à René Demellayer et au Dr Roberto Perez, pour avoir partagé leur grande connaissance de l'électro-érosion et pour leurs précieux conseils. Merci à vous tous pour votre soutien technique et scientifique, ainsi que pour votre enthousiasme face à mon travail.

Je tiens aussi à remercier les Drs Ivano Beltrami et Cédric Joseph ainsi que Marco Boccadoro de Agie, pour les discussions fructueuses que j'ai eues avec eux et leur intérêt pour mon projet.

Je remercie sincèrement MM. les professeurs Michel Rappaz et Jörg Winter qui ont accepté de faire partie de mon jury de thèse, ainsi que M. le professeur Robert Schaller qui l'a présidé.

Si le directeur d'un groupe de recherches est essentiel, ses autres membres ne le sont pas moins. Un très très très grand MERCI au Dr Jean-Luc Dorier, qui a toujours su écouter et trouver des réponses à mes questions tant scientifiques que techniques. Merci Jean-Luc de m'avoir fait profiter de tes impressionnantes connaissances, et merci de ne jamais être à court de gentillesse et de bonne humeur ! Je remercie également les Drs Alan Howling et Laurent Sansonnens pour leur disponibilité et leurs conseils toujours pertinents. Je suis particulièrement reconnaissant envers Alan qui a relu et corrigé ce manuscrit, et qui a ainsi rendu le texte un peu plus oxfordien.

Un grand merci aux doctorants du groupe, Samantha Pavon, Lukas Derendinger, Hannes Schmidt et Benjamin Strahm, mais aussi à il Dottore Raffaello Sobbia, pour avoir contribué à l'excellente ambiance de travail. Evidemment, un merci tout particulier à

Alban Sublet, ambassadeur de Haute-Savoie en Suisse, qui est devenu au fil de ces années bien plus qu'un simple collègue de travail. Merci Alban, collègue physicien, joggeur, fondeur, skieur, vététiste, randonneur, cinéaste, cinéphile, photographe, mélomane, et j'en oublie. T'es un jeune qui n'en veut, moi je dis chapeau.

Je tiens également à remercier les anciens doctorants du groupe, tout spécialement les Drs Thierry Delachaux et Malko Gindrat. Merci les gars pour les très nombreux moments de rire passés ensemble, sans vous ce n'est plus pareil... Merci Thierry pour les kilomètres courus en ta compagnie, en particulier ces 26.2 miles de souffrance entre Hopkinton et Boston un jour trop chaud d'avril. Et merci Malko, mon voisin de bureau pendant plusieurs années, de m'avoir transmis un peu de ta connaissance inépuisable de l'informatique.

Mes remerciements vont bien sûr également aux différents services techniques du CRPP. Merci aux mécaniciens, électriciens, électroniciens, au service du vide et au service informatique, pour les "p'tits boulots" occasionnels sans lesquels on n'avance pas au labo. Un très grand merci au secrétariat pour toutes les tâches administratives, avec mention spéciale pour Edith Grüter. Merci de tout mon coeur Edith, pour tout et surtout pour tout le reste !

Je tiens aussi à saluer Alexandre Blais, de l'université d'Ottawa certes, mais Québécois avant tout. Merci Alex de ton passage en Suisse, et merci mille fois de m'avoir fait découvrir les richesses de ta belle province. J'ai eu bin d's'fonne avec toé, mon go !

Enfin, je remercie infiniment tous les membres de ma famille, les personnes les plus importantes de ma vie, pour leur soutien tout au long de ces années. Merci à la nouvelle génération, Arthur, Gaspard, Anna, Elise et Camille, pour tout le bonheur que vous me transmettez. Merci à mes indispensables soeurs, Véronique, Noémie et Sarah, mais comment diable vivrais-je sans vous ?!? Merci à vous d'avoir choisi Françoise, Antoine et Stephan, je n'aurais pu faire meilleurs choix... Et un merci incommensurable à Maman et à Papa, pour m'avoir soutenu de toutes les manières possibles et m'avoir donné la chance de toujours pouvoir choisir et réaliser ce que j'ai eu envie de faire. Vous m'avez en plus donné l'amour de la Science, merci de m'avoir fait ce si beau cadeau...

Antoine

Curriculum Vitae

Antoine DESCOEUDRES

Né le 2 février 1978 à Lausanne (VD),
de nationalité suisse et originaire de La Sagne (NE).

FORMATION

- | | |
|-------------|--|
| 2002 - 2006 | Thèse de doctorat
effectuée dans le groupe des plasmas industriels,
Centre de Recherches en Physique des Plasmas (CRPP),
Ecole Polytechnique Fédérale de Lausanne (EPFL).
Assistant pour divers cours de Physique générale. |
| 1996 - 2001 | Diplôme d'ingénieur physicien , EPFL
Travail de diplôme effectué au CRPP. |
| 1993 - 1996 | Baccalauréat ès lettres (mention latin-mathématiques) et
Certificat de maturité - type A (latin-grec)
Gymnase cantonal du Bugnon, Lausanne. |

PUBLICATIONS

- A. Descoeudres, L. Sansonnens and C. Hollenstein, "Attachment-induced ionization instability in electronegative capacitive RF discharges", *Plasma Sources Sci. Technol.*, **12**(2), 152-157 (2003).
- A. Descoeudres, C. Hollenstein, R. Demellayer and G. Wälder, "Optical emission spectroscopy of electrical discharge machining plasma", *J. Phys. D: Appl. Phys.*, **37**(6), 875-882 (2004).
- A. Descoeudres, C. Hollenstein, R. Demellayer and G. Wälder, "Optical emission spectroscopy of electrical discharge machining plasma", *14th International Symposium for Electromachining (ISEM XIV)*, April 2004, Edinburgh, Scotland.
J. Mater. Process. Technol., **149**, 184-190 (2004).
- A. Descoeudres, C. Hollenstein, G. Wälder and R. Perez, "Time-resolved imaging and spatially-resolved spectroscopy of electrical discharge machining plasma", *J. Phys. D: Appl. Phys.*, **38**(22), 4066-4073 (2005).